An Experimental Study of Foam Flow in Fractured Systems of Increasing Size

Master Thesis in Petroleum Technology - Reservoir Physics

By

Sigbjørn Aasheim Johansen

Department of Physics and Technology

University of Bergen

June 2016

Abstract

Although use of foam for gas mobility control is substantially covered in literature, large-scale field implementation is still absent in fractured reservoirs. Current understanding of foam behavior in fractured systems is essentially based on experimental studies, and a recent investigation of foam generation in a rough-walled fractured system by coinjecting surfactant solution and gas showed that foam effectively reduce gas mobility in fractures. Reduced gas mobility favors stabilized gas-oil displacement in heterogeneous reservoirs where high-permeable "thief-zones" may result in viscous fingering due to early breakthrough of gas. This experimental thesis investigates foam flow in three different fractured systems, and the overall objective was to evaluate if increased system size (i.e. fracture length) had an impact on foam flow.

A total of 13 coinjections with surfactant solution and gas were carried out in fractured systems referred to as System A, B, and C. Systems A and B constitute two fractured marble cores with diameters of two and four inches, respectively, and were successfully drilled, fractured, and reassembled to replicate rough-walled fractures found in reservoirs. During all coinjections, the total volumetric rate was kept constant whereas gas fractional flow (F_g) was varied in pre-defined fractions. Measurements of differential pressure in all three systems indicated elevated flow resistance at $F_g = 0.7 - 0.9$, corroborated by observed generation of strong, fine-textured foam at high gas fractional flow. Foam rheology was evaluated using different flow rates in each system, and apparent viscosity of foam was found to decrease at increased flow rates, suggesting a shear-thinning foam behavior. Foam flow did not seem dependent on system size. Coinjections in all three systems obtained the highest flow resistance at high gas fractional flow and pressures gradient curves was highly comparable between the systems.

Positron emission tomography (PET) imaging was successfully applied to visualize liquid saturation and distribution during coinjection in System B. PET signals provided access to variation in local surfactant concentrations within the fracture network, and contributed favorable towards understanding observed differences in measured differential pressures. Visual investigation of foam texture during coinjection in System C showed texture changed from uniform, polyhedral bubbles to coarse, dry bubbles at a high gas fractional flow. Findings from this thesis will hopefully contribute to improved understanding of foam behavior in fractured systems.

Acknowledgements

First of all, I would like to express my gratitude to my main-supervisor, Associate Professor Martin Fernø at The Department of Physics and Technology, University of Bergen. Thank you for excellent guidance and creative suggestions for this thesis. I would also like to thank my co-supervisors, Professor Arne Graue and Associate Professor Geir Ersland for the opportunity to conduct this thesis as a part of the Reservoir Physics group and for letting me travel overseas to attend conferences of relevance for my studies.

Thanks to Inez Buzdugan, Dr. Marianne Steinsbø and Dr. Bergit Brattekås for assistance and guidance in the lab. Your practical sense and insight on experimental work has been impressive and all help from you have been very much appreciated. Also a big thanks to Dr. Jarand Gauteplass for the assistance during imaging experiments.

Numerous other individuals provided assistance along the way. I would like to thank the staff at the mechanical workshop for excellent work on modifying experimental equipment used in this thesis. I would also like to thank the competent and friendly staff at the Haukeland University Hospital for helping us run imaging experiments and for granting us access to their PET/CT lab.

I would also like to thank new friends and students I have met during my five years as a student in Bergen. Fellow students in "Svigjengen" has helped me focus and keeping my spirits up during the last couples of weeks and I wish you all good luck after this journey ends. A special thanks goes to my good friend and laboratory partner, fellow master student Snorre Sande Vasshus. Your commitment, knowledge and enthusiasm has been a major source of inspiration throughout this work!

Finally, I would like to give my deepest appreciations to my parents, Pål and Gro, as well as my sister, Solveig for their support and motivation throughout my years of study.

Bergen, May 2016

Sigbjørn Aasheim Johansen

Table of Contents

Introduction

The global energy consumption is increasing and the world's population is expected to pass the eight billion mark within the next decades. Although renewable sources of energy (e.g. wind power, hydropower, and solar energy) are developed and utilized to meet this demand, fossil fuels are believed to remain the primary energy resources in foreseeable future. The current situation with low oil and gas prizes due to an oversupplied marked may, however, constraint new developments within the petroleum industry. Companies emphasize cost-effective operations and strive to make a profit. Use of conventional recovery techniques such as pressure depletion and secondary water- or gasflooding are favored, seldom yielding recovery factors higher than 20-40 percent of original oil in place (Muggeridge et al., 2013). Hence, substantial reserves may be left behind in reservoirs as residual oil. Residual oil is a target for enhanced oil recovery (EOR) techniques, in which chemicals or gases not originally present in the reservoir are injected to increase sweep efficiency (Ahmed and Meehan, 2011).

Approximately 50 percent of the world's petroleum resources are located in carbonates, characterized by heterogeneities in permeability and wide distribution of fractures (Bust et al., 2011). Recovery by gas flooding may prove ineffective in these reservoir as high transmissivity of fractures facilitates viscous fingering and early breakthrough of gas. Implementation of foam as an EOR measure may, however, improve displacement efficiency by reducing gas mobility with factors as great as 5000 (Buchgraber et al., 2012). Reduced gas mobility due to unique viscous properties of foam improve the mobility ratio between oil and gas. Foam could also enhance volumetric sweep efficiency by blocking off high-permeable zones (e.g. fractures) and divert displacing fluids into unswept, oil-rich zones (Guo et al., 2011). Field implementation of foam for mobility control in fractured carbonate reservoirs has yet been limited because foam flow in fractures is still not fully understood (Fernø et al., 2016).

Studies by Kovscek et al. (1995) showed that foam effectively reduced gas mobility during coinjection of surfactant solution and nitrogen into a transparent replica of a rough-walled fracture. Foam films were observed to bridge the fracture aperture and induce the highest flow resistance at high gas fractional flow. Similar findings were reported by Fernø et al. (2016), observing foam generation and flow inside a fractured marble tile with large variations in fracture aperture. Reduction in the apparent viscosity of foam at elevated flow rates suggested reduced mobility control of gas due to shear thinning of foam from a significant drag between flowing foam and rough fracture surfaces.

This experimental thesis was carried out to investigate foam dependency on system size using three different fractured systems. Foam was set to generate by coinjecting surfactant solution and gas in pre-defined fractions directly into fractures. By recording differential pressure as a function of gas fractional flow, foam properties such as apparent viscosity and mobility reduction factor could be cross-examined between systems of various fracture lengths. The thesis is divided into five chapters. Chapter 1 introduce theory and experimental findings on foam flow in fractures. In addition, a short introduction is given on the imaging techniques used in this thesis (PET/CT). Chapter 2 includes detailed descriptions of materials, fluids and experimental setups used. Chapter 3 contains experimental results and discussion for System A, B, and C, and concluding remarks are presented in Chapter 4 along with proposed future efforts. References used are presented in Chapter 5 in addition to three appendixes A, B, C, containing uncertainty calculations, fundamentals and raw data from coinjections, respectively.

Chapter 1: Theory

1 Scaling

Reservoir heterogeneities and complex fracture geometries may lead to poor volumetric sweep efficiency in many of the reservoirs on the Norwegian Continental Shelf (Aarnes et al., 2007). Volumetric sweep efficiency defines the fraction of the total reservoir volume that is contacted by an injected fluid during a displacement process. Laboratory research on gas/oil displacement in heterogeneous systems report foam to have excellent mobility control abilities, increasing sweep efficiency by diverting gas flow from high permeable thief zones to zones with lower permeability (Li et al., 2011). However, to successfully use foam in reservoirs, foam behavior needs to be characterized on a variety of scales (Pancharoen et al., 2012).

The objective of this experimental thesis is to characterize foam flow in fractured systems of increasing size. Generally, up-scaling describe the integration of small-scale flow mechanisms observed in the laboratory into coarse grid models of a reservoir. Here, foam flow is observed in systems of different fracture lengths, and corescale in **Figure 1** is emphasized. PET/CT imaging was used to monitor foam flow inside a fractured core to provide insight on foam distribution within a fracture network. Findings from this thesis will hopefully contribute to improved understanding of foam behavior in fractured systems.

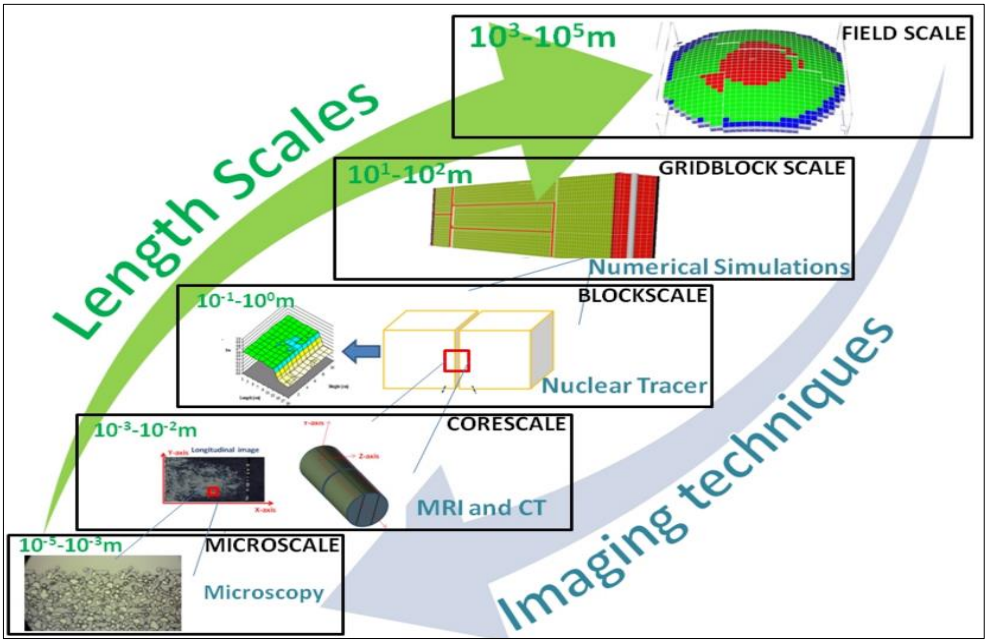

Figure 1: Summary of the various scales under study for petroleum reservoirs (Fernø, 2015). The green arrow represents up-scaling from capillary driven flow observed in micromodels all the way up to field scale where reservoir heterogeneities affect flow performance. The experiments of this study covers corescale.

2 Fractured Reservoirs

A fractured reservoir can be defined as a reservoir where naturally occurring fractures have a significant effect on reservoir fluid flow, predominantly in the form of increased reservoir permeability (Nelson, 2001). Low permeable rocks such as carbonates are heavily dependent on fractures to be economically recoverable (Ahr, 2011).

van Golf-Racht (1982) related fracture patterns to geological events, keeping in mind that an elementary rock volume in a reservoir experience stress from overburden pressure, confining pressure, pore pressure and tectonic forces. Considering a depositional environment where thick layers of deposits are stacked on top of each other, a sufficiently high overburden pressure may result in extension, normal or inverse faults. A fault is a discontinuity in a rock volume resulting from sliding movement (Marshak, 2011). Because associated shear fractures tend to be oriented parallel to faults, it is possible to estimate the fracture direction near a known fault in a reservoir. Characterizing fractures from folding processes are much more complicated. An example could be the rise of a salt dome, where an initially plain layer experience stress from below from propagating salt. Due to several states of stress throughout the lifting process, both conjugate and orthogonal fractures develop over the fold, shown in **Figure 2**.

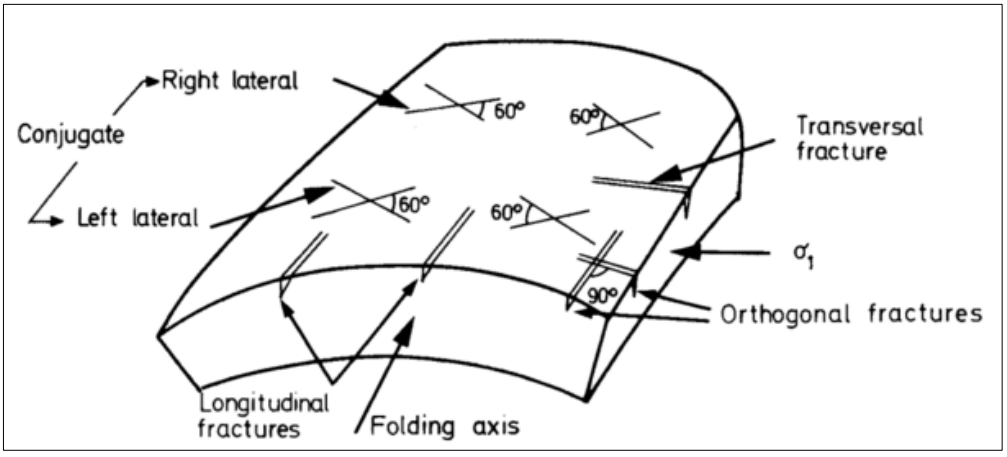

Figure 2: Different types of fractures associated with a folding process (van Golf-Racht, 1982).

As several fracture patterns and geometries can occur in one single reservoir, characterizing fractured reservoirs solely based on observed fractures is difficult. Instead, Firoozabadi (2000) classified fractured reservoirs into three groups depending on their fluid distribution in matrix and fractures.

Type I: Fracture pore volume is very small compared to the matrix pore volume where the majority of hydrocarbons are stored. Ekofisk chalk, consisting of high porosity matrix from calcite shell fragments falls into this category (Skarestad and Skauge, 2012).

Type II: Most of the hydrocarbons reside in the matrix, but the fracture pore volume may be as high as 10%-20%. One example could be Asmari limestone reservoirs (Firoozabadi, 2000).

Type III: More than half of the hydrocarbons are stored in fractures. Although the Keystone field in Texas is a valid example of such a field, few reports on production performance of these reservoirs can be found in the literature (Firoozabadi, 2000).

2.1 Recovery in Fractured Reservoirs

The impact from fractures on storage capacity and flow properties in a reservoir can present itself as abnormal behavior in production compared to what is expected in a conventional reservoir. Following is a list of production characteristics for fractured reservoirs (Allan and Sun, 2003):

- Because fractures increase the transmissivity (i.e. ability to transfer flow) in a fractured reservoir, pressure drops around producing wells are very low. In fact, pressure gradients have limited effects on production because fracture/matrix-block communication is the primary drive mechanism.
- Fluid expansion, gravity drainage and imbibition ensure a continuous supply of oil from matrix blocks into fractures during production from reservoirs containing adequate matrix permeability. This leads to lower pressure decline per barrel of oil produced compared to conventional reservoirs.
- Fractured reservoirs lack transition zones as high permeability in fractures provide a mechanism for rapid re-equilibration of fluid contacts, resulting in sharp oil-water and gas-oil contacts during production.
- PVT properties are commonly constant throughout a fractured reservoir as convective circulation occurs during production.

Proper reservoir characterization is crucial prior to exploitation of a field. Mistaking a fractured reservoir for a conventional reservoir, for instance, could result in poor reservoir performance, and choosing the appropriate recovery method must be carefully considered in advance.

2.1.1 Primary Recovery

Primary recovery constitutes the simplest method of extracting hydrocarbons from a reservoir. The idea is to utilize the existing natural pressure in the reservoir as a drive mechanism by performing pressure depletion. Uren (1939) found that the natural pressure present in a reservoir originates from various forces, for instance expansion of natural gas and water drive from supporting aquifers. These forces could act either simultaneously or sequentially, depending on reservoir properties and composition (Donaldson et al., 1989).

Allan and Sun (2003) stated that fractures in brittle reservoir rocks such as dolomite and tight limestone tend to connect the reservoir to regional aquifers. Some of the highest recovery efficiencies observed in their survey on 100 fractured reservoirs were in fact achieved by unassisted primary recovery from a strong bottom water drive. Weak correlation between ultimate recovery factor and matrix and fluid properties in these reservoirs suggest that the recovery efficiency is heavily dependent on fractures. In more ductile reservoirs such as chalk, fractures tend to be located around faults. Limiting the connection to supporting aquifers, an existing gas cap is necessary if primary recovery is to be considered. Normally, application of secondary or tertiary methods is essential for maximizing recovery in such reservoirs (Allan and Sun, 2003).

2.1.2 Secondary Recovery

Secondary recovery occurs as artificial energy is applied to the reservoir, commonly by injection of water or immiscible gas (Speight, 2013). This provides pressure support extending the lifetime of the field, along with an additional push helping the hydrocarbons to flow towards producing wells (e.g. in a 5-spot configuration).

Being the first field in production on the Norwegian Continental Shelf, the Ekofisk field (chalk) is a good example on use of secondary recovery in fractured reservoirs. Almost immediately after production start in 1971, the pressure went into steep decline. Pressure depletion caused subsidence in the reservoir, resulting in lowering of the production rig towards the ocean surface and fear of rig failure (Yudovich et al., 1989). The decision of injecting water into the reservoir to prevent further subsidence was genius. As it turned out, the reservoir was highly responsive to waterflooding and recovery was increased significantly. Immiscible gas/oil displacement is also a viable option in fractured reservoirs. Vertical communication from fractures favors gas-oil gravity drainage. By injecting gas from above, oil will be drained downward due to the density difference between the two phases. Matrix sections saturated with oil will also experience an additional drainage effect from surrounding gas-saturated fractures, as gravitational forces around the block will exceed the capillary forces inside the block, mobilizing the oil (Okon and Udoh, 2013). In contrast to conventional reservoirs, liberated gas from the oil preferentially flows straight to the top of the reservoir through fractured pathways rather than horizontally towards the nearest wellbore, generally resulting in a lower gas-oil ratio (Denney, 2003).

One limitation using gasflooding for oil recovery is the mobility contrast between gas and oil. The mobility ratio M is defined as the ratio between the mobility of the displacing fluid λ_j behind the flood front and the mobility of the displaced fluid λ_k ahead of the front (Zolotukhin and Ursin, 2000). Strongly influencing the residual oil saturation S_{or} left after a recovery process, M is given as:

$$M = \frac{\lambda_j}{\lambda_k} = \frac{k_{rj} \cdot \mu_k}{k_{r,k} \cdot \mu_j} \tag{1}$$

where k_r is the end-point relative permeability and μ is the viscosity of the fluids. Because $\mu_g \ll \mu_o$, a heterogeneity in permeability (e.g. fracture) reducing the resistance to flow could cause the displacing fluid to channel through the oil as a viscous finger, resulting in a limited sweep as much of the oil remain untouched (Lyons and Plisga, 2005). This is illustrated in **Figure 3** below:

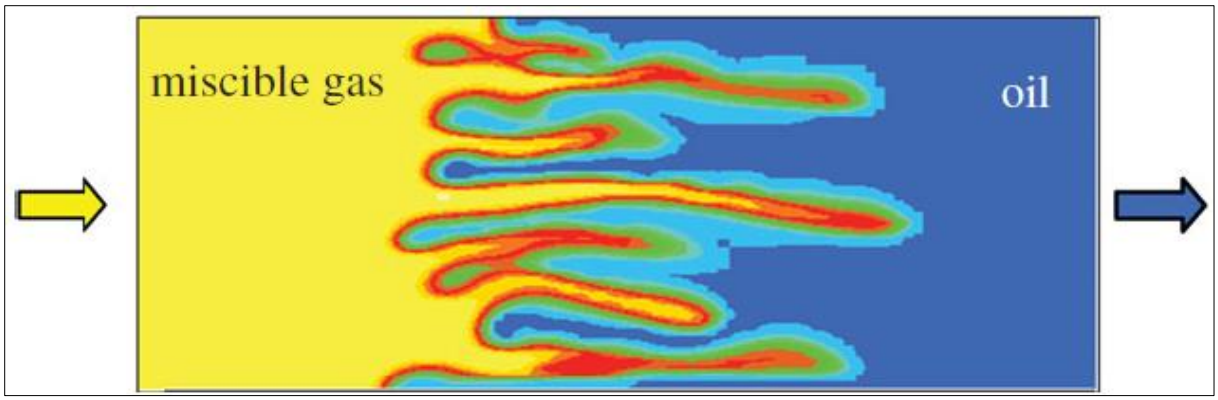

Figure 3: Simulation of viscous fingering when low-viscosity gas displace oil at M=10 (Muggeridge et al., 2013).

2.1.3 Tertiary Recovery

Tertiary or enhanced oil recovery (EOR) is an additional production step designed to recover residual oil by injecting chemicals or gases not originally present in the reservoir (Ahmed and Meehan, 2011). A variety of different EOR methods has been developed over the years, and these may be divided into two major categories: non-thermal and thermal recovery (Al-Anazi, 2007). An overview is given in **Figure 4** below.

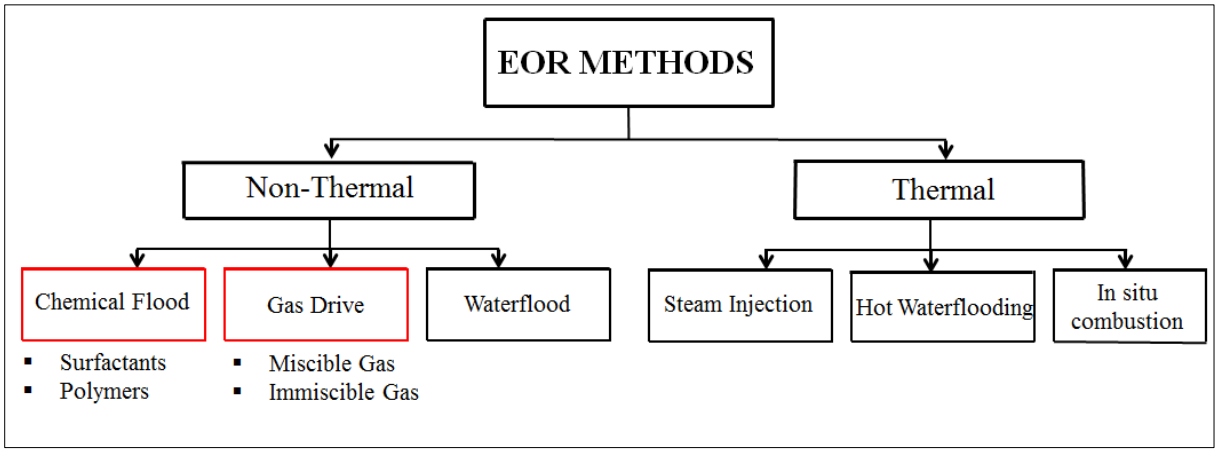

Figure 4: Overview of different EOR methods. Thermal methods are used when temperature affects recovery efficiency (e.g. mobilization of high viscous oils). Non-thermal methods including injection of chemicals and/or gas are particularly of interest in this thesis and are highlighted in red. Redrawn from (Al-Anazi, 2007).

Chemical Flood

Injection of chemicals called surfactants reduces the residual oil saturation by increasing the capillary number (defined in Appendix B). Surfactants molecules, often represented as a tadpole consisting of a nonpolar (lypophile) tail and a polar (hydrophile) head, orient themselves at the interface between two fluids based on where they have the greatest affinity. Adsorption along the interface provides an expanding force causing a drastic reduction in the normal interfacial tension (Schramm, 1994). Anionic surfactants have been used to alter the wettability of fractured carbonates from oil-wet to more water-wet states. This improves recovery as the relative permeability of oil increases when the aqueous phase imbibe into smaller pores, displacing additional oil (Anderson, 1986, Wang and Mohanty, 2014). Other chemicals such as polymers are used to create a more favorable mobility ratio and thus increase the sweep efficiency in a displacement process.

Gas Drive

Tertiary gasflooding in previously waterflooded reservoirs could also enhance oil recovery. By injecting natural gas (e.g. methane) from an existing gas cap or nearby fields, the goal is to recover oil capillary trapped by water and oil untouched by previous waterfloods. Gas flow in new pathways results in contact between oil and gas, and residual oil is mobilized in a miscible or immiscible process (Skjæveland and Kleppe, 1992). High permeability in fractures compared to rock matrix is, however, a challenge for application of this recovery method in fractured reservoirs as gas may channel into the high-permeable fractures, leading to early breakthrough and poor sweep efficiency (Fernø, 2012). Unique flow properties of foam suggest that gas override and limited sweep efficiency may be prevented when foam acts as a mobility control agent during EOR (Kovscek et al., 2010).

3 Foam

Foam got a significantly higher viscosity compared to gas and may improve volumetric sweep efficiency in fractures by reducing the mobility contrast between oil and gas (Yan et al., 2006). In the following section, basic characteristics of foam will be described before foam flow and generation in fractures are emphasized. Fundamental parameters such as interfacial tension, capillary pressure and capillary number are an integer part of foam characteristics and petroleum recovery in general. However, because these parameters are not emphasized and qualitatively investigated in this thesis, a brief overview are included in Appendix B.

3.1 Foam Structure and Characterization

Foam consists of bubbles of gas dispersed within a continuous layer of liquid. Each bubble is separated by a thin liquid film called lamella, and a point of contact between three films is known as a Plateau border. A temporary film equilibrium is achieved when the bubbles assume a position determined by capillary pressure and surface tension (Exerowa and Kruglyakov, 1998), illustrated in **Figure 5**. The foam is metastable and thermal fluctuations leads to rearrangement with time (Stevenson, 2011). To generate and sustain liquid films, a surfactant is introduced to the liquid phase. Generally, the surfactant concentration must exceed a critical micelle concentration to generate stable foam (Mukerjee and Mysels, 1971, Buchgraber et al., 2012).

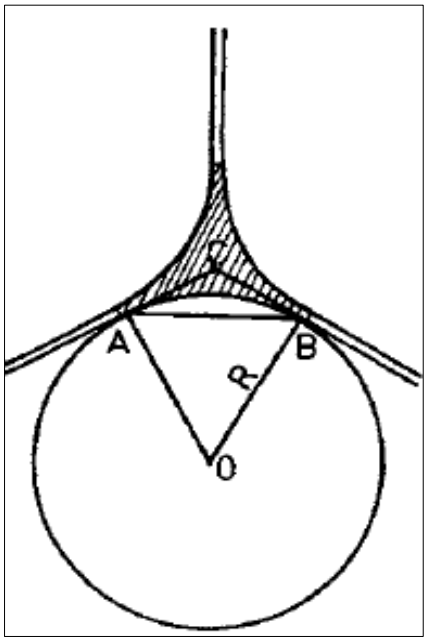

Figure 5: Cross-section of a Plateau border. The first law of Plateau states that since film tensions are equal, forces acting in one plane can balance one another only if the three angles between them are equal i.e. $\angle ACB = 120°$ while all the angles in triangle AOB are equal to 60°, making $AB = R$. The border radius of curvature R could therefore be determined with a microscope by measuring the side AB (Exerowa and Kruglyakov, 1998).

Because foams are thermodynamically unstable and complex, it has been stated that "any attempt to understand their properties in terms of a 'simple' all-embracing theory is doomed to failure" (Schramm, 1994). However, there are different ways for characterizing foam. These are discussed below.

Foam quality is defined as the percentage of gas volume per volume of foam (Martins et al., 2001). Low quality foams ($F_g \leq 0.5$) are referred to as wet foams, consisting of spherical bubbles well-separated by liquid. Due to their sparsely texture, i.e. number of lamellae in unit volume, these are considered weak (Kam, 2007). In the high-quality domain, dry, gas-rich foam with flat liquid-films and polyhedral shape develops as bubbles accumulate. Such fine-textured foam will cause multiple film faces in pores, resulting in a stronger, more resistant foam due to increased viscosity (Grundmann and Lord, 1983). The different types of foam qualities are shown in **Figure 6** below.

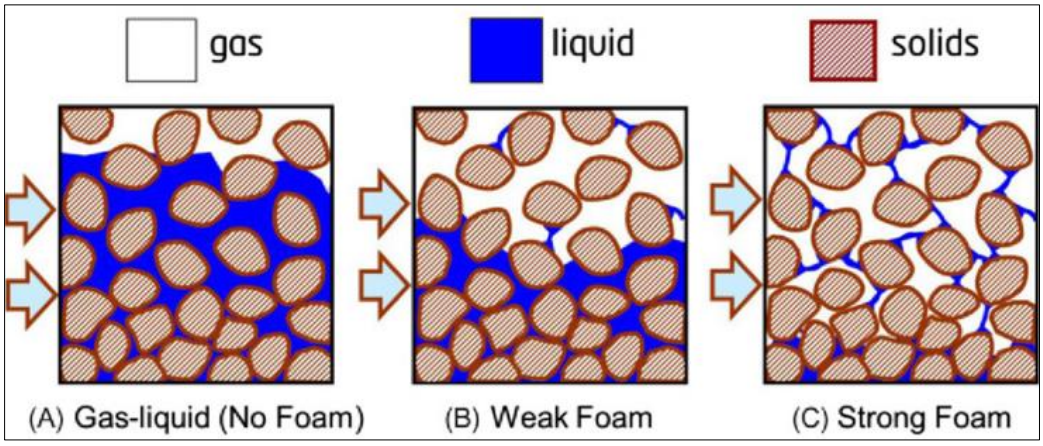

Figure 6: Illustration of foam appearance within a porous media. Foam strength ranging from non-existent to the left to dry on the right (Sheng, 2013).

Bubble size is controlled by foam quality, and this relation depends primarily upon the type and concentration of surfactant used (Holm, 1968). Since each bubble is filled with compressible gas, changes in pressure and temperature may cause the bubbles volume to change. If the pressure decreases, the gas will expand and make the bubbles larger (Grundmann and Lord, 1983). In foam structures of heterogeneous bubble size distribution, the gas in smaller ones tends to diffuse into larger ones because the pressure is higher inside the smaller bubbles compared to the larger ones (Martins et al., 2001).

Rheology is a science of deformation of matter with time and is used to explain non-Newtonian fluid flow where stress is not proportional to rate (Corapcioglu, 1996). Studies through the 70's and 80's reviled that foams got non-Newtonian flow characteristics with a pseudoplastic behavior at different shear rates and is several orders of magnitude more viscous (10-100 cP) compared to its constituting phases: liquid and gas (Patton et al., 1983). To get a qualitative description of the viscous properties of foam, Hirasaki and Lawson (1985) compared viscosity measurements on foam flowing through smooth capillaries with a mathematical model of apparent viscosity. They concluded that the apparent viscosity of foam is a sum of three contributions: (1) viscosity from liquid in lamella, (2) the resistance in the interface of a bubble flowing through a capillary, and (3) a surface tension gradient generated when surfactant sweeps from the front to the back of a bubble. Treating foam as a single phase in Darcy's law, apparent viscosity can be given as (Farajzadeh et al., 2015):

$$\mu_f^{app} = \frac{K \nabla P}{Q} \tag{2}$$

where k [D] is the permeability, ∇P [bar/cm] is differential pressure over the length of the system and Q [ml/s] is total volumetric rate. Decrease in μ_f^{app} with increased flow rates indicate shear thinning of the foam, i.e. thinning of liquid lamella. Film thinning reduce foam strength and if flow rate is

increased (higher stress), bubbles will collapse spontaneously. Shear thinning foams will thus have a higher viscosity at low flow rates with moderate stress and lower viscosities at high flow rates with high levels of stress (Lee and Ramesh, 2004).

3.2 Foam Generation in Fractures

Foam experiments has been conducted in a variety of fractured systems ranging from idealized fracture models characterized by smooth rock surfaces and homogeneous fracture distribution to rough-walled, heterogeneous networks. Generally, lamellae are created by three different mechanisms; snap-off, lamella-division, and leave-behind (Chen et al., 2004). Snap-off is believed to be the dominant foam generation mechanism and occurs in constriction sites of the flow path featuring abrupt change in capillary pressure. In accordance with equation (A4) in appendix B, the capillary pressure between gas (non-wetting) and water (wetting) is higher inside a constriction with small fracture aperture than in surrounding flow space with larger aperture. Increased pressure in the wetting phase result in influx of water toward the neck of the constriction, followed by snap-off and separation of gas bubbles (Ransohoff and Radke, 1988).

Kovscek et al. (1995) studied foam flow inside a transparent replica of a rough-walled fracture. Foam was generated in two ways; in-situ by coinjecting nitrogen and surfactant solution into the fracture and by use of a Berea sandstone pre-generator. Snap-off appeared to be the primary foam-generation mechanism and observation of bubble shape and size indicated that in-situ foam had approximately four times larger bubbles compared to pre-generated foam. Differences in bubble size was assumed to be a result of a limited number of snap-off sites inside the fracture compared to the pre-generator. Large bubbles were observed to become more stationary at high gas fractional flow. As shown in **Figure 7**, lamella bridged fracture aperture and resulted in elevated flow pressure due to increased flow resistance within the fracture.

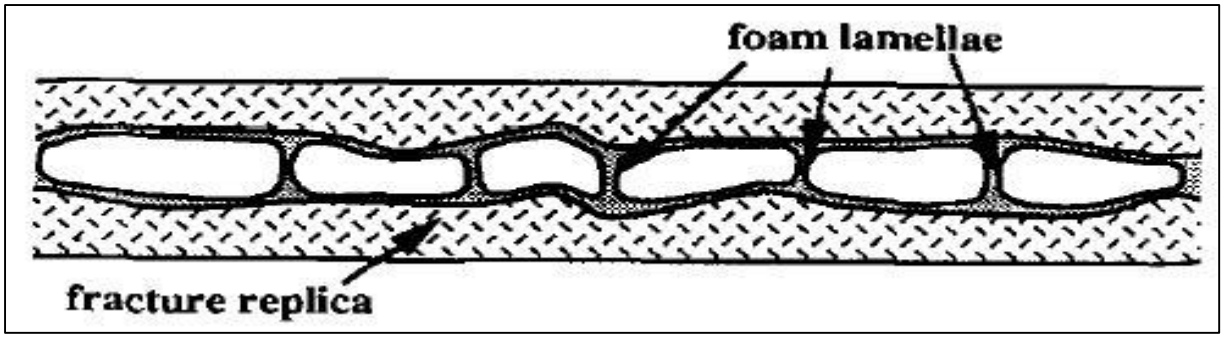

Figure 7: Simple schematic of foam flow through a transparent replica of a rough-walled fracture. Lamella was observed to bridge fracture aperture at high gas fractional flow, resulting in elevated flow pressure (Kovscek et al., 1995).

Fernø et al. (2016) reported similar observations during coinjection of gas and surfactant solution into a fractured marble network with complex variations in fracture aperture (System C in this thesis). Lamella generation by snap-off was observed in large vugs, and the ultimate foam resistance was measured at $F_g = 0.90$. Coinjecting gas and surfactant solution into a 2D silicon micromodel representing a fractured network, Gauteplass et al. (2015) verified snap-off to be the predominant in-situ foam generation on micro-level. Using a high resolution camera, rectilinear snap-off was observed at constriction sites where the wetting phase (water) accumulated into pores initially filled with gas. Areas where low permeability matrix opened into high permeable fractures also featured snap-off sites. Lamella was found to primarily follow only one pathway, usually where the pore throat radius was greatest, preventing foam generation from lamella division to occur.

3.3 Foam Stability

Foam generated in a field must be stable enough to propagate through the formation to ensure a high sweep efficiency. Friedmann and Jensen (1986) found that a high velocity gas injection strategy could enhance foam stability. Increased shear between gas/surfactant/porous media results in smaller, uniform bubbles, characterizing a high quality foam. This logic does not apply when CO_2 is used for mobility control. High quality CO_2 foams could be extremely immobile and result in a drastic pressure drop across the reservoir. Instead, a low quality foam could be appropriate as these can be injected for a long time period as CO_2 gradually approach the mobility of oil (Enick and Olsen, 2012). Following are some essential factors influencing foam stability.

A limiting capillary pressure is found to destabilize foam films generated inside a porous medium. During foam flooding, capillary pressure increases with decreasing saturation of the wetting fluid, similar to a drainage process in a water-wet reservoir (see appendix 2). Reduction in water supply from Plateau borders to lamellae result in film-thinning (Farajzadeh et al., 2015). Approaching a limiting capillary pressure, P_c^*, the work required to destabilize a film is minimal, and minor mechanical disturbances or thermal fluctuations is enough to cause rupture (Vrij and Overbeek, 1968). P_c^* results in a coarse, unstable foam texture and depends upon the type of surfactant, its concentration and electrolyte content (Khatib et al., 1988).

Diffusion could result in foam coalescence, and is defined as a process where physical properties are transferred from one location to another (Janssen et al., 2013). Pressure difference between small and large bubbles in a foam drives gas to diffuse through the lamella from smaller bubbles to larger bubbles (Sheng, 2013).

Gas compressibility effects are reported to make an impact on foam flow in porous media. At low pressure gradients, foam moves as bubble trains when a minimum pressure gradient $(\nabla P)^{\min}$ is obtained (Rossen, 1988):

$$(\nabla P)^{\min} = (\Delta P)^{\text{avg}}\, \mathrm{n_L} \tag{3}$$

where $(\Delta P)^{\text{avg}}$ is the average differential pressure between each lamella in the train and $\mathrm{n_L}$ is the number of lamellae per unit length. Lamella require a positive pressure difference between each bubble of the train to flow. An increased $(\nabla P)^{\min}$ value due to compression of gas filled bubbles may, however, cause unequal $(\Delta P)^{\text{avg}}$ distribution within the bubble train, resulting in random fluctuations in pressure and frequent separation of bubbles. Compressible foams increase the flow resistance by occupying pore throats and depends on bubble size, presence of trapped gas and bubble-train length (Rossen, 1988).

3.4 Foam in Mobility Control

The ability of foam to reduce gas mobility by presence of thin foam films in gas injection processes emphasize significant improvement in both aerial and vertical sweep efficiency (Sheng, 2013). Reduced gas mobility lowers the risk of gravity override and viscous fingering through high-permeability zones, and the idea is to divert gas into unswept and oil-rich areas and thereby increase oil recovery (Guo et al., 2011).

The mobility reduction factor (MRF) quantifies the reduction in mobility of gas when foam is present, and is given as (Buchgraber et al., 2012):

$$MRF = \frac{\Delta P_f}{\Delta P_g} \tag{4}$$

where ΔP_f [Pa] and ΔP_g [Pa] is the differential pressure across a fracture or porous media caused by foam and single-phase gas, respectively. Studies by Holm (1968) indicated that foam only allows gas to move by breaking and re-forming bubbles. Under such circumstances, gas enters foam and start moving as flowing bubbles. In the largest pores of a water-wet medium, the aqueous phase (e.g. surfactant solution) resides along the pore walls while the gas moves as "bubble trains" in the center of the pores (Enick and Olsen, 2012). A significant drag force between the interfacial area of the foam and the rock surfaces result in limited movement for the gas bubbles (Hirasaki and Lawson, 1985). Immobile, trapped gas, shown in **Figure 8**, can be found in intermediate sized pores. Stationary foam impact gas mobility when foam films block for further gas propagation and thereby reduce the relative permeability of gas (Kovscek and Radke, 1993).

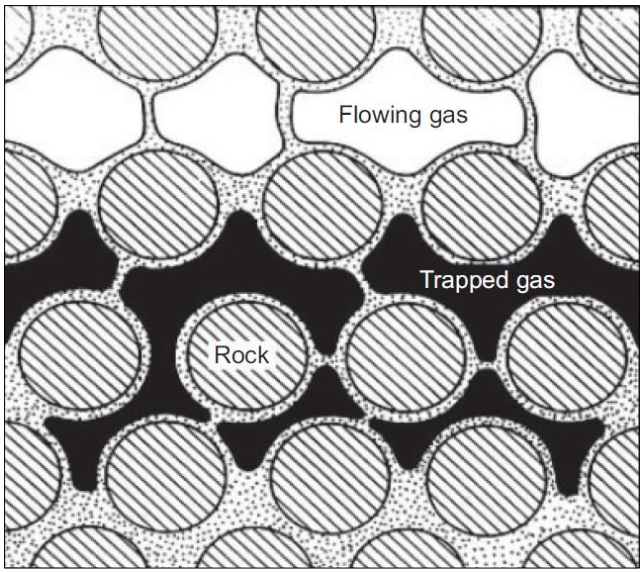

Figure 8: Illustration of gas mobility in foam flow. Mobile foam bubbles are represented as a white "train" of bubbles flowing through the largest pore spaces and stationary, trapped gas is represented by a black color (Kovscek et al., 2010) .

4 Literature Survey: Foam in Mobility Control

Lawson and Reisberg (1980) showed that foam is applicable as a mobility control agent during oil displacement in homogeneous sandstone and limestone core samples. Foam was generated by injection of alternate slugs of nitrogen and surfactant solution, and gravity segregation and viscous fingering by gas was not observed. Low measurements in gas relative permeability at high gas saturations indicated pockets of trapped gas within the porous medium. Presence of stationary gas hindered early gas breakthrough, and replacement of oil by large bodies of gas was thought to be the predominant mobility control mechanism.

Foam has also proven to be effective in fractures and high permeable thief zones during tertiary gasflooding. Li et al. (2011) increased oil recovery significantly by initiating a foam flood in previously waterflooded sandpacks of heterogeneous permeability, shown in **Figure 9**. Reduced mobility and increased viscosity of the gas phase after foam generation resulted in an improved sweep in layers of lower permeability. Mobilization of residual oil by gas was observed through a glass observation window attached to the sandpacks. A variety of different surfactants were used due to foam collapse in presence of crude oil.

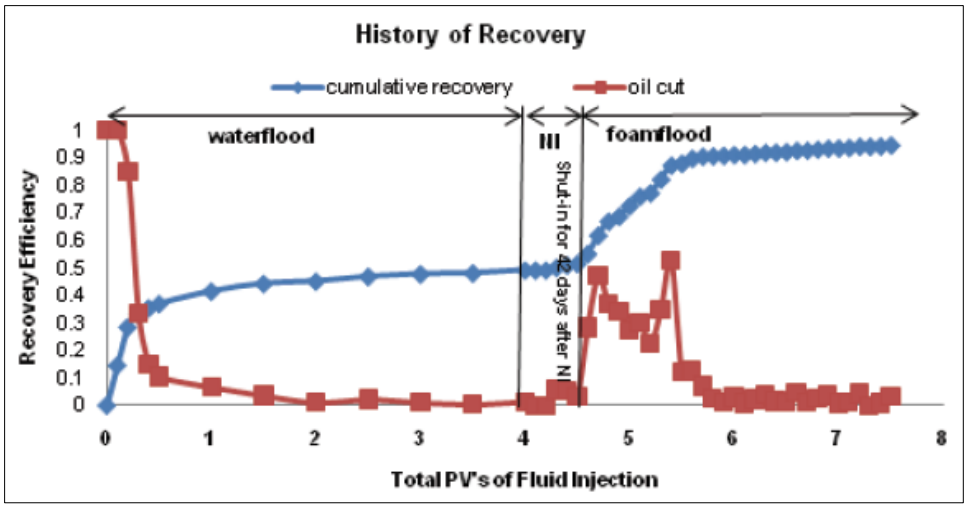

Figure 9: Plot of oil recovery and oil cut as a function of pore volumes injected in a layered system containing heterogeneous permeability zones (Li et al., 2011). After 4 pore volumes of waterflooding the system was shut in for 42 days to let gravity and capillary flow settle. Foam flooding gives an almost linear recovery response and stabilize after approximately 1 PV. This is favorable from an economical point of view.

Foam generation in fractures with various roughness and width has been investigated by Buchgraber et al. (2012) using 2D micromodels. Pore-scale observations from a high resolution camera along with differential pressure measurements proposed significant reduction in gas mobility during foam flow in fractures. Mobility reduction factor (MRF) ranged from 300-500 in rough fractures and were found to increase linearly up to a foam quality of 90%. For foam with quality >95%, lamella reportedly collapsed and smaller bubbles were stored in larger bubbles. MRF for wet foams did not appear to depend on liquid flow rate.

Skauge et al. (2002) presented a full-scale field application of foam for gas mobility control in the Snorre Field, using a Foam Assisted Water Alternating Gas injection (FAWAG) strategy. In the Western Fault Block of the Snorre Field, the motivation was to prevent early gas breakthrough and thus increase sweep efficiency. Simulation and history matching confirmed increased oil production as a result of improved sweep from the foam, and it was concluded that foam is a qualified alternative for

EOR in the North Sea. The financial costs of the FAWAG operation was 1M USD, while the additional oil recovery observed from January 2000 in **Figure 10** was 25-40 M USD considering the oil price at the time.

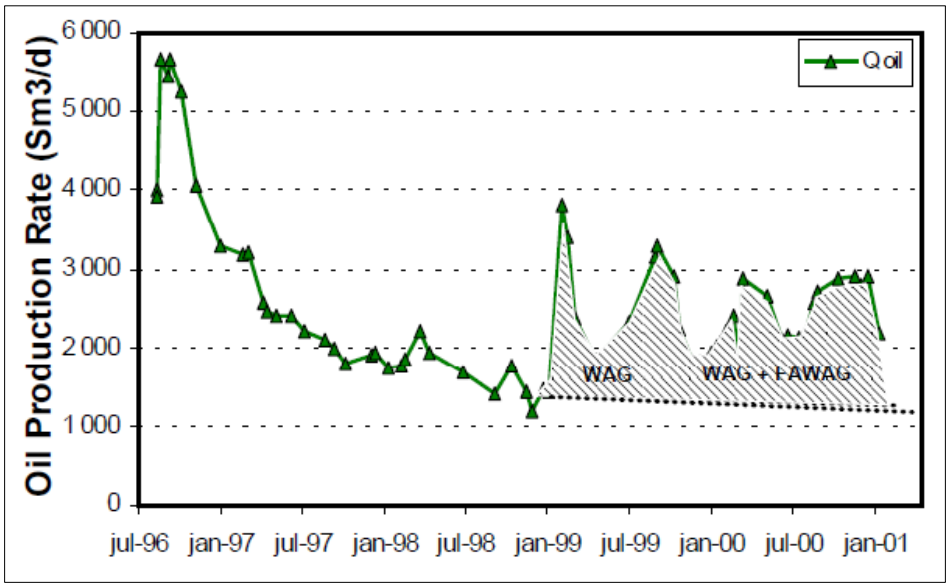

Figure 10: Simulated oil production on the Western Fault Block. The peak in oil production was established a few months after initiation of waterflooding, followed by a decline in oil rate with time. Switching to WAG and later FAWAG schemes increased oil recovery, indicating that foam is an appropriate strategy for EOR (Skauge et al., 2002).

5 Imaging Techniques

Following is a brief description of imaging techniques used in this thesis.

5.1 X-ray Computed Tomography

X-ray Computed Tomography (CT) use an x-ray source and multiple detectors to create cross-sectional images of an object of interest (e.g. core sample). Because CT scans offers an accurate and time-efficient way to investigate lithology, porosity and saturation inside of a rock without causing any damage, it has become an integral part of petroleum research (Hicks, 1996).

Emitted x-rays experience attenuation, or gradual loss in intensity, as they move through a core sample. The number of x-rays successfully penetrating the core depends on rock properties, and is measured as the linear attenuation coefficient, μ_a, defined in Beer's law as:

$$\mu_a = \rho_b \left(a + \frac{bZ^{3.8}}{E^{3.2}} \right) \tag{5}$$

where $\rho_b [\mathrm{kg/m^3}]$ is the bulk density of the sample, a and b are empirical constants, Z is the effective atomic number in the sample and E [kV] is the initial x-ray energy (Hicks, 1996). By collecting multiple μ_a readings from different angles of a core sample, it is possible to generate a two-dimensional (2D) image representing a thin slice of the cross-sectional area (Suzuki, 1990). To alternate the angle of incoming x-rays, the core could be rotated around its own axis during the scan. Alternatively, the x-ray source and the detectors may be rotated around a stationary sample. CT may be used to map areas of high density within a core sample. By moving the sample in lateral direction between each 2D image, it is possible to create a three-dimensional (3D) image of the entire core sample. Using this technique, Eide (2011) managed to identify high-density areas inside a water saturated chalk core, shown in **Figure 11.**

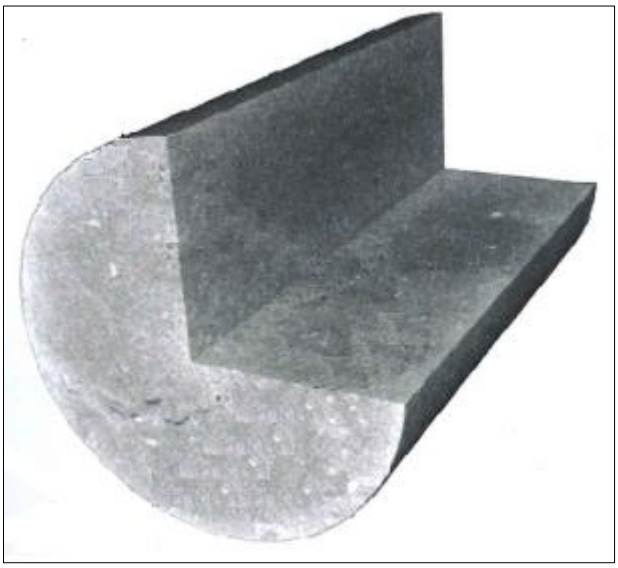

Figure 11: Three dimensional CT image of a water saturated Portland chalk core (Eide, 2011). Dark shade represents high-density areas where x-rays experienced significant attenuation whereas a lighter color indicates less dense material.

5.2 Positron Emission Tomography

Positron Emission Tomography (PET) generates 3D images of radioactive tracers flowing through a system by measuring emitted gamma radiation (Maucec et al., 2013). PET technology has played an important role in medicine for decades, and has also proven applicable in petroleum research. By adding a radioactive tracer to a fluid of interest in a multiphase flow system, this imaging technique allows a unique in-situ visualization of fluid distribution and propagation.

^{18}F-fluorodeoxyglucose (FDG) was chosen as the radioactive isotope for the PET experiments in this thesis. Because ^{18}F is easy to produce in particle accelerators (e.g. cyclotrons) and got a relatively short half-life (109 minutes) minimizing the radiation dose, it is frequently used on patients in hospitals (Bailey et al., 2004). **Figure 12** illustrates the underlying physics using ^{18}F in PET imaging. The ^{18}F isotope consists of an unstable nucleus with 9 protons and 9 neutrons surrounded by a total of 9 electrons circulating in fixed orbits (Bailey et al., 2004). Spontaneous decay of the nucleus result in emission of a positively charged positron, considered an anti-particle of electrons because it got identical mass and opposite charge. A collision between a positron and an orbiting electron result in annihilation and emission of two gamma rays. These are oriented anti-parallel in space, making it possible to determine their line of response (LOR) if two detectors are placed on opposite sides. Tomography analysis on multiple LORs captured from various angles, illustrated in b) in **Figure 12**, makes it possible to create a high-resolution 3D image of a tracer moving through a system over time (Maucec et al., 2013).

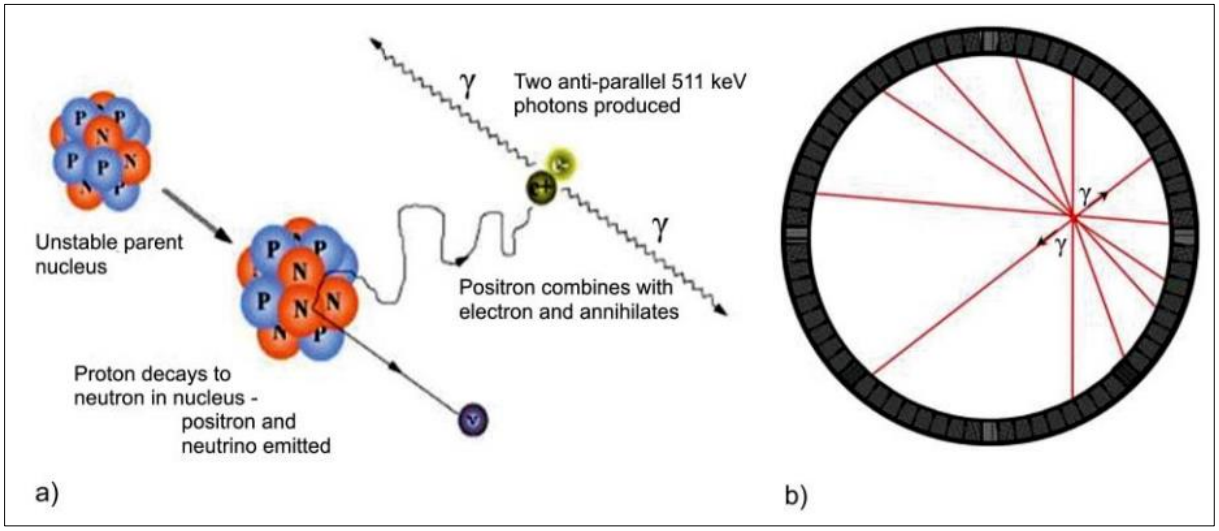

Figure 12: The physical principles in PET scans (Maucec et al., 2013). A) A positron emits from decay in the nucleus. A following positron/electron collision result in emission of two gamma rays moving in opposite directions with an angle of 180° between them. B) A PET scanner got detectors covering 360° around the system, making it possible to create 3D images of the tracer.

Chapter 2: Experimental Procedures

Experimental Objective

The objective of this thesis was investigate foam flow in fractured systems of increasing size. Two fractured cores of different length were developed to replicate one small and one intermediate system. In addition, a fractured marble tile was used to represent a large system. The design of the fractured marble network made it possible to visually observe foam flow during the coinjection and inspect foam texture at various gas fractional flows. Because the cores were placed in Hassler core holders during the experiments, it was not as straight forward to visualize fluid flow in these experiments. Hence, imaging techniques (PET/CT) were used to characterize foam distribution inside fractures. By comparing the results from the different fractured systems, the goal was to determine how system size influenced foam flow.

6 Fluids and Materials

6.1 Fluids

Table 1 lists the fluids used in the experiments in this thesis. To generate foam and investigate foam properties at different foam qualities, a coinjection strategy with surfactant solution and gas was applied. Aqueous surfactant solutions were made by mixing concentrated surfactant with brine (1 wt% NaCl) using a magnetic stirrer. To ensure equal brine composition in all experiments, a synthetic brine consisting of 10 g NaCl and 990 g distilled water (1 wt% NaCl brine) was used. Two different surfactants (Petrostep C-1 and Huntsman SURFONIC® L24-22) were added to increase foam stability. These had significant differences in texture. Petrostep C-1 appeared as a high-viscous liquid and was quickly dissolved in brine using a magnetic stirrer. The surfactant from Huntsman had texture similar to wax, and was separated into small pieces before it was added to brine. The magnetic stirrer dissolved all the solid material into brine solution.

Both air and nitrogen (N_2) were used as gas during the coinjection experiments. Dry air contains a mole fraction of 0.78 N_2 and was assumed to have the same properties as pure N_2 at experimental conditions.

Table 1: Fluids used in experiments. All experiments were performed at normal temperature and pressure (20 °C and 1 atm).

Fluid	Composition
Brine	1 wt% NaCl
Surfactant solution I	1 wt% Huntsman SURFONIC® L24-22 in 1 wt% NaCl brine
Surfactant solution II	1 wt% Petrostep C-1 in 1 wt% NaCl brine
Gas I	Nitrogen, N_2
Gas II	Air

Marble was chosen as rock material for the foam experiments conducted in this thesis. This is a metamorphic rock composed of calcite and is considered to be impermeable (Attanasio et al., 2006). Low-permeable matrix was believed to result in fluid flow primarily within fractures.

6.2 Marble Cores

Preparation of fractured core samples was done together with fellow master student Snorre Sande Vasshus. The job was accomplished in several steps and is described in detail below.

6.2.1 Drilling of Cores

Marble blocks were available at the Department of Physics and Technology, University of Bergen. These were initially cleaned with soap and a high-pressure water hose to remove attached moss from previous exposure to weather. To drill core samples of high quality, the marble blocks were transported to the core lab facility at Statoil Sandsli. Diamond coated bits with outer diameters of two and four inches were used to penetrate the solid marble. Prior to drilling, the blocks were mounted to the foundation of the drilling assembly, as shown in (1) in **Figure 13.** This increased stability and reduced the risk of uneven diameters over the lengths of the cores. During drilling, water was continuously supplied to the drilling bit to prevent overheating and flush calcite particles out of the drilling hole. A relatively high and constant drilling rate was found to be optimal. At low revolution per minute (RPM) settings, the bit stopped halfway through the block due to friction. A total of approximately 40 core samples were drilled.

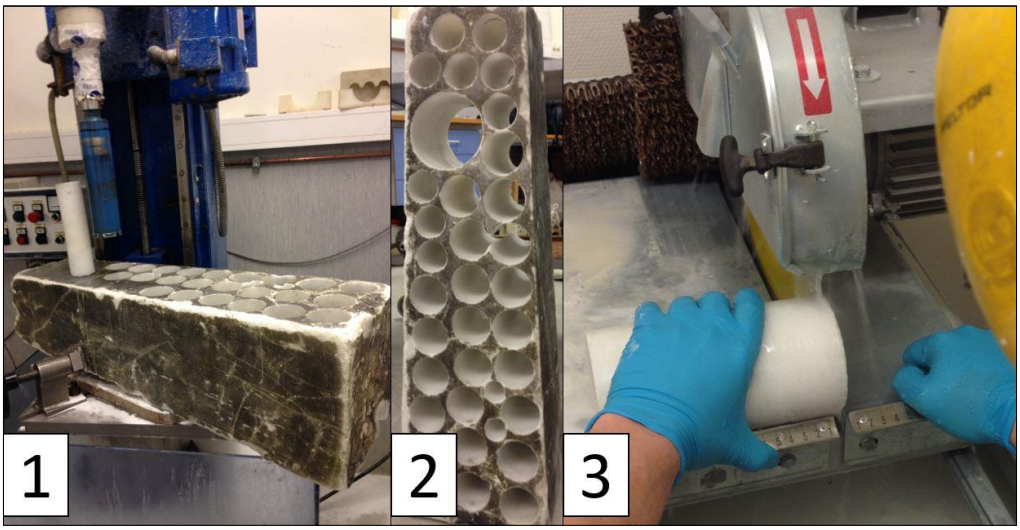

Figure 13: Drilling procedure on a marble block. 1) Water-cooled drilling machine used at Statoil Sandsli. The panel in the back controlled drilling rate and water supply to the bit. 2) One of the marble blocks after drilling. The majority of the cores shown here have a diameter of 2". A 4" hole can be seen on the top left. 3) Asymmetric geometry on the marble blocks resulted in a slight difference in dip on the short sides of the cores. A saw was used to get an equal angle on both faces of the cores.

Fractures found in reservoirs originates from geological events involving enormous amounts of stress. To create similar fractures in a lab, two practical aspects had to be considered:

- To ensure a safe working environment and reproducibility of the fracturing method, a standardized procedure had to be established.
- It had to be possible to reassemble the rock pieces into one solid core after the fracturing.

6.2.2 Fracturing Procedure

A specialized fracturing device was designed in collaboration with the mechanical workshop at the Department of Physics and Technology. With inspiration from Brazilian test procedures described by Cote and Thimus (1999), the idea was to place a given core horizontally between two metal plates and generate fractures by applying pressure from above. The metal plates holding the core were included core-shaped tracks with a thin edge in the center. The edge reduced the area of stress between the device and the core, accelerating the generation of fractures and facilitating vertical stress vectors, indicated with red arrows in (1) in **Figure 14**. To fit cores of various diameters, the top plate was adjustable in vertical direction. Pressure was applied on the top plate by an extension arm driven by a hydraulic press from Enerpac. The press could deliver a maximum overburden pressure of 700 bars and was regulated manually by a handle. An installed pressure gauge allowed readings of pressure during the procedure. An example of a generated fracture is shown in (2).

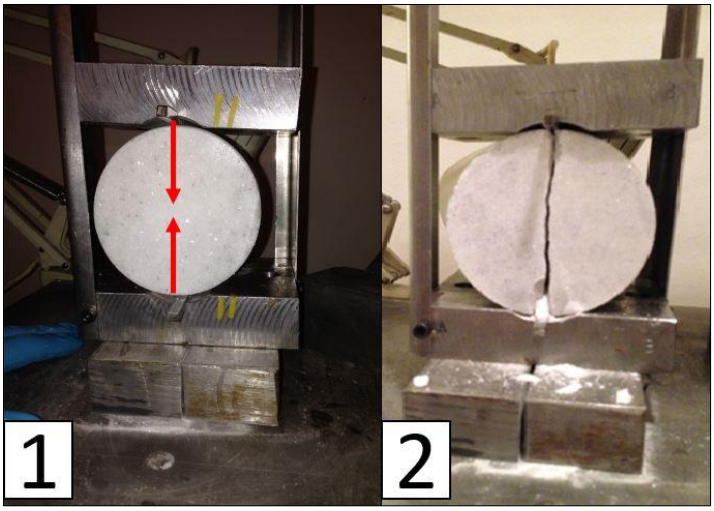

Figure 14: Fracturing device. 1) Front-view of an unfractured marble core placed in the device. The red arrows represent the direction of stress through the core when overburden pressure is applied. 2) Fractured core sample. The resulting fracture developed in vertical direction. Notice the amounts of debris below the core, indicating use of significant amounts of force.

Because large amounts of force were released over a short time period, it was decided that at least two participants had to be present at all times. A proposed step-by-step fracturing procedure is given below:

Step 1: Carefully place the core in the center (both horizontally and vertically) of the fracturing device. Make sure the core is contacted by the top and bottom plate over its entire length.

Step 2: A protection screen is placed in front of the device before pressure is applied. This will block potential debris leaving the core at the time of failure.

Step 3: One of the participants handles the hydraulic press while another act as an observer. The observer wears a face mask to safely inspect the core during the procedure. The extension arm from the hydraulic press is slowly lowered to the fracturing device before initiating the fracturing procedure.

Step 4: The pressure should be increased in small steps, i.e. 10 bars up in each step. This gives the observer time to look for developing fractures and makes it easier to quantify the exact pressure applied on the core at the time of failure. The majority of the cores (both 2” and 4”) fractured at an

overburden pressure of approximately 120 bar. Core failure tend to occur just after an increase in applied pressure and is characterized by a loud cracking noise.

Step 5: After the maximum pressure is recorded, the fractured core is carefully removed from the device. To avoid confusion between the different cores, each sample is puzzled together and wrapped in a paper towel marked with a specific name.

Figure 15: Fractured core sample. Remaining dust and debris were carefully brushed away before the pieces were puzzled together.

A majority of the marble core samples obtained controlled fracture patterns, as shown in **Figure 15**. Commencing flow experiments on cores with open fractures was not an option. Detachment and re-positioning of pieces between and during experiments would most likely compromise fluid flow through the core (e.g. as extreme gravity segregation) and thus prevent comparability of experiments.

6.2.3 Reassembling Procedure

To hold the pieces together and maintain a fixed fracture geometry, the cores were wrapped with several layers of aluminum foil. Duct tape was used to keep the end-fold of the foil in place. Low resistance to shear-movement in aluminum foil was, however, a concern as rotational movement may occur when a core is placed in a core holder. For that reason, it was decided that shrink tubing from Zeus, shown in (1) in **Figure 16**, should be used as an additional coating material. This is a robust plastic material designed to shrink at high temperatures. Aluminum coated cores were placed inside shrink tubing with diameters of 2" and 4" before a heat gun was used to raise the temperature. The shrink tubing responded instantly to heat and the initial space between tubing and core was sealed almost immediately. This procedure is shown in (2)**.** Due to the length of the 4" cores, two heat guns were used simultaneously to ensure equal heat distribution over the core, preventing development of plastic folds. When the shrink tubing was tightly sealed over a given area of core, the sample was rotated and the same procedure was done over 360 degrees. The result was a thick, smooth plastic coat, as shown in (3). A scissor was used to trim remaining foil stretching over the length of the core.

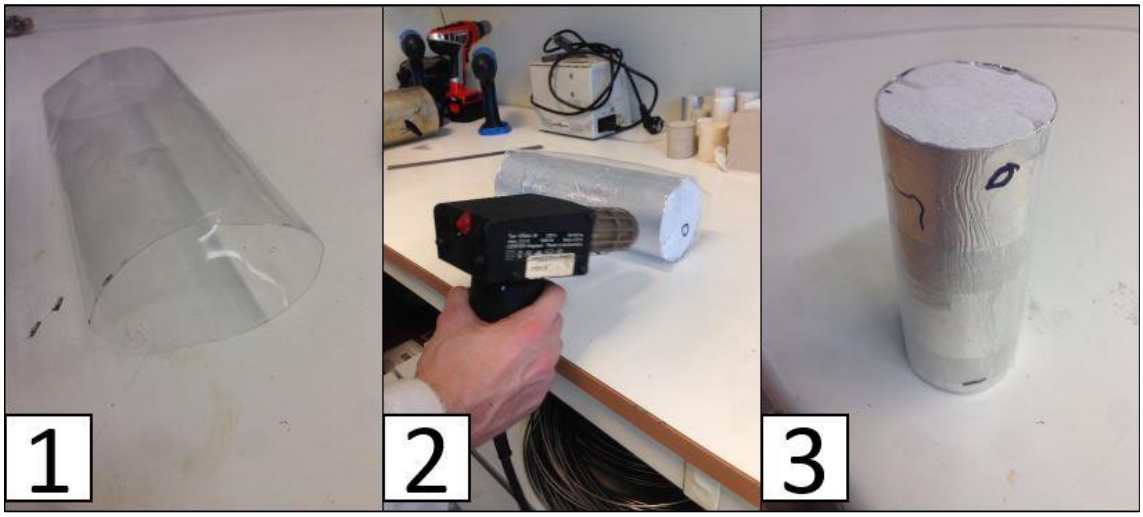

Figure 16: Application of shrink tubing in core assembling. 1) Unused shrink tubing from Zeus. 2) Heat guns were used to shrink the plastic around the core. 3) Fractured core covered with aluminum foil and shrink tube.

6.3 Fractured Marble Network

A fractured marble network has previously been developed by the reservoir physics group at the Department of Physics and Technology. This model consists of a fractured marble tile (31.2 cm x 31.2 cm) kept together between two Plexiglas plates. The transparent Plexiglas makes visual observation of advancing foam possible. The fractured marble network got a porosity of 7 % and an absolute permeability of 3.64 Darcy. Further details regarding the of the network design are given by Fernø et al. (2016).

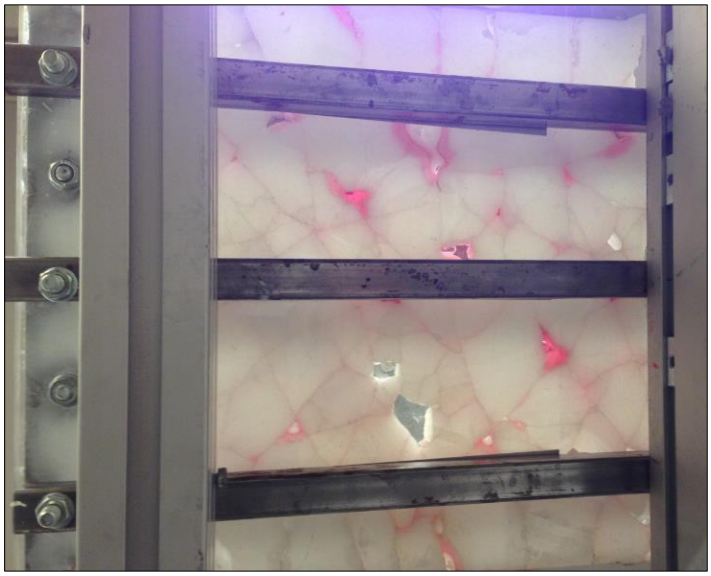

Figure 17: Photo of the fractured marble network after injection of a red contrast fluid. Although the majority of the fractures were narrow, some wide ones (seen with red contrast fluid) were included to make it possible to observe foam propagation and variation in foam quality during the experiments (Fernø et al., 2016).

7 Experimental Setups

7.1 System A: Fractured Marble Core (Two-Inch Diameter)

Foam generated by coinjection of surfactant solution and gas was studied in a fractured marble core with a diameter of two inches at low pressure and temperature. A majority of the experiments were carried out in the petroleum lab at the Department of Physics and Technology together with fellow master student Snorre Sande Vasshus. Routine core analysis was carried out in advance of the experiments to determine essential properties of the fractured core.

7.1.1 Routine Core Analysis

Porosity, φ, is a key parameter describing the available pore space within a rock and is defined as the ratio between pore volume, V_p [cm^3], and bulk volume, V_b [cm^3], of a core sample:

$$\varphi = \frac{V_p}{V_b} \tag{6}$$

The bulk volume of System A was determined geometrically by measuring the length and diameter of the core with a caliper and multiply surface area with length. The pore volume (i.e. fracture volume) was determined using the saturation method, shown in **Figure 18**. Firstly, a fractured core was placed inside a Hassler core holder mounted in an upright position where air was removed by a vacuum apparatus connected to the top of the assembly. Valve 1 was then closed and valve 2 at the bottom was connected to a beaker filled with sandstone brine. Secondly, valve 2 was opened, resulting in instant suction of brine into the vacuumed system. The amount of brine inside the core was determined by subtracting the weight of the beaker before and after valve 2 was opened.

Figure 18: Photo of a vertically placed two-inch core holder during pore volume estimation using the saturation method. An upright position was used to fill the core with brine from the bottom and displace pockets of air.

Sandstone brine with known density was used and the pore volume was calculated:

$$V_p = \frac{\Delta m_b}{\rho_b} \tag{7}$$

where Δm_b [g] is the weight difference of the brine filled beaker before and after brine was sucked into the fractured core and ρ_b $[\frac{\text{g}}{\text{cm}^3}]$ is the density of the brine. The absolute permeability, K, for System A was determined using Darcy's law. Differential pressure was measured at various injection rates, assuming 100 percent water saturation. In this thesis, K was used to calculate the apparent viscosity, μ_f^{app} during coinjection for in-situ foam generation. **Table 1** summarize measured and calculated parameters of System A. Uncertainties are based on uncertainty in the apparatus designated by the manufacturer (e.g. caliper, digital weighing scale, and pressure transducers).

Table 2: Key parameters of System A determined from routine core analysis. Low porosity coincides with limited matrix space in marble and high permeability indicates good communication between the fractures in System A.

Length [cm] ± 0.002 [cm]	Diameter [cm] $\pm$ 0.002 [cm]	Bulk volume [cm^3]	Pore volume [cm^3]	Porosity [%]	Abs.perm [D]
14.935	5.080	302.0 ± 1.0 [1)]	17.9 ± 0.2 [1)]	5.95 ± 0.06 [1)]	3.94 ± 0.07 [1)]

[1)]Uncertainties calculated from equation (A1) in appendix A.

7.1.2 Experimental Setup and Equipment

Figure 19 gives an overview of the experimental setup used for System A. Black lines represents plastic tubing and green lines represent cables connecting different devices to a computer.

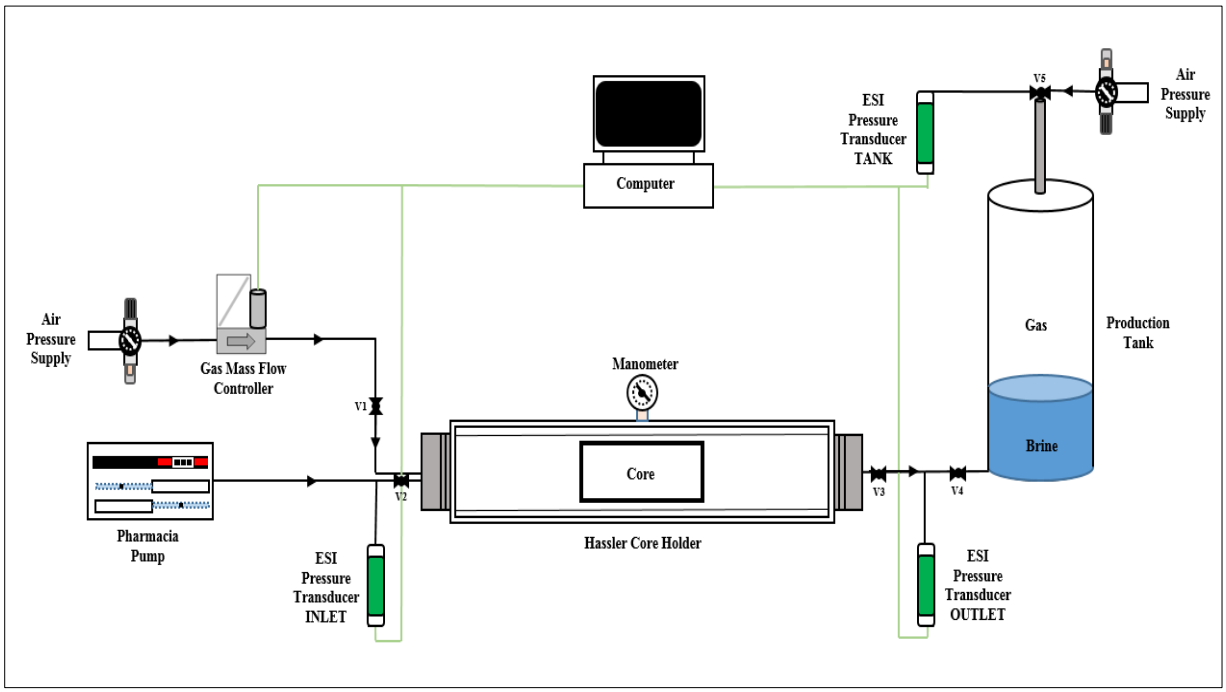

Figure 19: Schematic of the experimental setup used during coinjection of surfactant solution and gas into fractured marble cores. Black lines with arrows indicate the direction of fluid flow inside plastic tubing whereas the green lines indicate connection cables between devices and a computer. The computer was used to monitor pressure and regulate gas injection rate via a gas mass flow controller.

List of Equipment Used

- 2 x Air pressure supply (Maximum pressure delivery of 10 bar)
- Bronkhorst EL-FLOW® Select Series Mass Flow Meter / Mass Flow Controller
- 1/16 plastic tubing with Swagelok fittings and valves
- Pharmacia LKB P-500 pump
- 3 x ESI Digital USB Pressure Transducer, range 0-6 barg ($\pm$ 0.1 % FS)
- Computer used to regulate gas mass flow controller and record pressure
- Two-inch Hassler type core holders with confinement pressure
- Production tank (20-liter volume) used to maintain a constant back pressure

7.1.3 Description of Experimental Procedure

The fractured core was placed inside a Hassler core holder, as shown in **Figure 19**. A confinement pressure of approximately 10 bar was applied to hold the core in place and avoid fluid flow outside the fractures during coinjection. Surfactant solution from the Pharmacia pump and gas from the Bronkhorst Mass Flow Controller was injected in two separate tubes connected to Swagelok distribution ports on the inlet side. Two ports located in close proximity of each other was used to ensure rapid mixing between the two phases and facilitate in-situ generation of foam inside the fractures. Two ESI pressure transducers was connected on the inlet and outlet tubing to measure the differential pressure across the system.

Produced surfactant solution and gas was collected in a tank at the outlet, with valve 3 and 4 open. By opening valve 5 to an air pressure supply, the production tank generated a backpressure in System A. Compressed air worked as a piston by applying force on accumulated liquid at the bottom of the tank. Elevated flow pressure reduce gas compressibility effects and could thus enhance foam quality (Buchgraber et al., 2012). The pressurization was performed in advance of the experiments, using multiple steps in pressure increase (e.g. 0.5 bar in each step). Elevated backpressure resulted in temporary backflow inside the system, and pressure was not increased further until steady state flow was confirmed (i.e. stabilized differential pressure). A dedicated ESI pressure transducer was connected to the tank to monitor potential increase in backpressure during the coinjections.

The coinjections in System A used a constant volumetric rate and pre-defined changes in gas fraction. $F_g\ 0-1$ indicates a coinjection from pure surfactant injection ($F_g = 0$) to pure gas injection ($F_g = 1.0$). $F_g\ 1-0$ represent the opposite coinjection, changing from pure gas injection ($F_g = 1.0$) to pure surfactant injection ($F_g = 0$). **Table 3** show changes in gas fraction during a 3 ml/min coinjection.

Table 3: Variations in gas fractional flow during coinjection with a constant volumetric rate of 3 ml/min. Air was used as injected gas and 1 wt% Huntsman SURFONIC® in 1 wt% NaCl brine was used as injected surfactant solution.

Fg 0 – 1 coinjection											
Gas fraction [frac. of total flow]	0	0.1	0.2	0.3	0.4	0.5	0.6	0.7	0.8	0.9	1.0
Gas rate [ml/min]	0	0.3	0.6	0.9	1.2	1.5	1.8	2.1	2.4	2.7	3.0
Surf. Solution rate [ml/min]	3.0	2.7	2.4	2.1	1.8	1.5	1.2	0.9	0.6	0.3	0
Fg 1 – 0 coinjection											
Gas fraction [frac. of total flow]	1	0.9	0.8	0.7	0.6	0.5	0.4	0.3	0.2	0.1	0
Gas [ml/min]	3.0	2.7	2.4	2.1	1.8	1.5	1.2	0.9	0.6	0.3	0
Surf. Solution [ml/min]	0	0.3	0.6	0.9	1.2	1.5	1.8	2.1	2.4	2.7	3.0

7.2 System B: Fractured Marble Cores (Four-Inch Diameter)

A fractured core with a diameter of four inches was developed to evaluate how foam behavior change with increased fracture length. Similar coinjections (as in System A) were performed, using a constant volumetric rate and pre-defined alteration of gas fractional flow. In addition, it was desired to visualize foam flow inside the fractures using a combined PET/CT scanner at the Haukeland University Hospital. Hence, an almost identical experimental setup as the one for System A was rigged in the PET lab. Because the PET machine is used on cancer patients during the weekdays, the experiment was conducted over a weekend.

7.2.1 Experimental Setup and Equipment

Figure 20 show the PET/CT scanner with some of the equipment used during the coinjections. Equipment from System B are listed below.

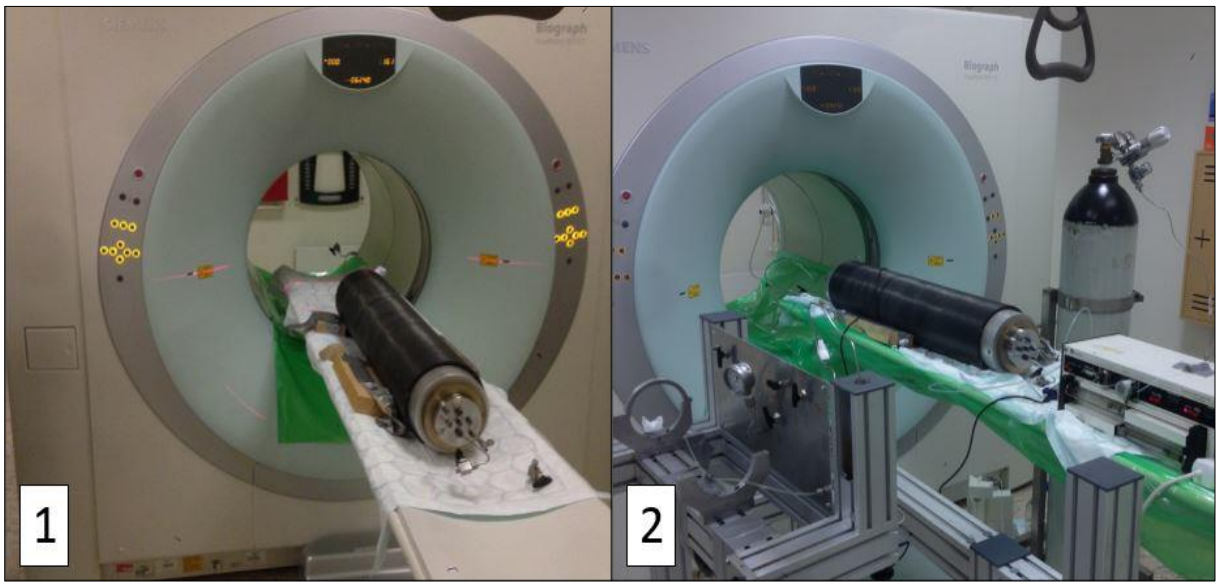

Figure 20: Pictures from the PET/CT experiment at Haukeland University Hospital. 1) The core holder alone was scanned with a high resolution CT scan to map major fractures inside the core. Lasers were used to adjust the core into optimal position. 2) An overview of the experimental setup during PET/CT scan. A nitrogen tank supplying the mass flow controller is visible in the background and a hand-regulated confinement pump is seen to the left. The patient bed holding the core was adjustable in horizontal direction and was situated inside the detector ring during the scan.

List of Equipment Used

- Siemens Biograph™ TruePoint™ medical PET/CT scanner
- Four-inch Hassler type core holder compatible with X-ray and gamma scanning from Core Laboratories
- ^{18}F-FDG radioactive isotope produced in a cyclotron was used to trace surfactant solution
- Autoclave/Swagelok fittings and valves
- Production tank connected to a backpressure regulator to maintain a constant backpressure
- Nitrogen tank
- Bronkhorst EL-FLOW® Select Series Mass Flow Meter / Mass Flow Controller
- Pharmacia LKB P-500 pump
- 2 x ESI Digital USB Pressure Transducer, range 0-6 barg ($\pm$ 0.1 % FS)
- Computer used to regulate gas mass flow controller and record pressure

7.2.2 Description of Experimental Setup

First, the four-inch core holder was placed inside the PET/CT scanner for a dry CT scan. Lasers were used to position the core in the center of the bore with detectors. X-rays with an energy of 120 keV was used, and registered attenuation was converted to 490 vertically sliced images. The image stack covered the entire length of the core and had a high resolution with voxel sizes 0.6 mm x 0.6 mm x 0.6 mm. High resolution is favorable as it makes it easier to characterize fractures.

Prior to the PET scan, an experimental setup as the one for System A was established, with the core holder resting on the patient bed as shown in **Figure 20**. After the equipment was assembled, the bed was moved horizontally until the core holder was located in the center of the detector ring. Crucial equipment such as the Bronkhorst mass flow controller and the Pharmacia pump was mounted to the patient bed to avoid unnecessary pull on the plastic tubing during bed positioning. The mass flow controller received nitrogen gas from a tank whereas the Pharmacia pump was supplied by surfactant solution from a container on the floor. Long plastic tubing was used to give the system flexibility to movement. The production tank was placed behind the PET/CT machine and was connected to the outlet of the core with a long plastic tubing. Backpressure was regulated with an available air pressure supply in the lab. In addition, a backpressure regulator was installed on the production tank to evacuate potential overpressure inside the tank.

Radioactive ^{18}F-FDG with an activity of 350 MBq was produced in a cyclotron by a radiologist the same morning and was delivered in a syringe stored in a lead box. Immediately after the $F_g\ 0-1$ coinjection was initiated, ^{18}F-FDG was added to the surfactant solution. Detected PET signal was monitored over a time period of 8 hours and included all changes in gas fractional flow from $F_g = 0$ to $F_g = 1.0$. A PET scan detects only gamma radiation and does not show isotope distribution inside the rock. Hence, a CT scan was performed in advance with identical resolution as the PET (voxel size 2.0 mm x 2.0 mm x 0.6 mm) to map the fractured core. Merging PET/CT images will then result in a 3D image of surfactant distribution within the core.

^{18}F-FDG did still emit a relatively high radiation at the end of the experiment, and the dismantling of the experimental setup was done the next day.

7.3 System C: Fractured Marble Network

The fractured marble network described in **Section 6.3** was used to up-scale foam flow in fractures spanning over a large area. Although PET/CT imaging of a core gives a unique visualization of foam distribution inside a fractured system, the low resolution prevents evaluation of foam texture. The transparent Plexiglas surrounding the marble network, however, facilitates visual inspection of foam texture and bubble variation at different gas fractions. The experiments on the fractured marble network were conducted in the petroleum lab at the Department of Physics and Technology together with fellow master student Snorre Sande Vasshus.

7.3.1 Setup and Equipment

An overview of the experimental setup is shown in **Figure 21**. Details from the experimental procedure are given in **Section 7.3.2**.

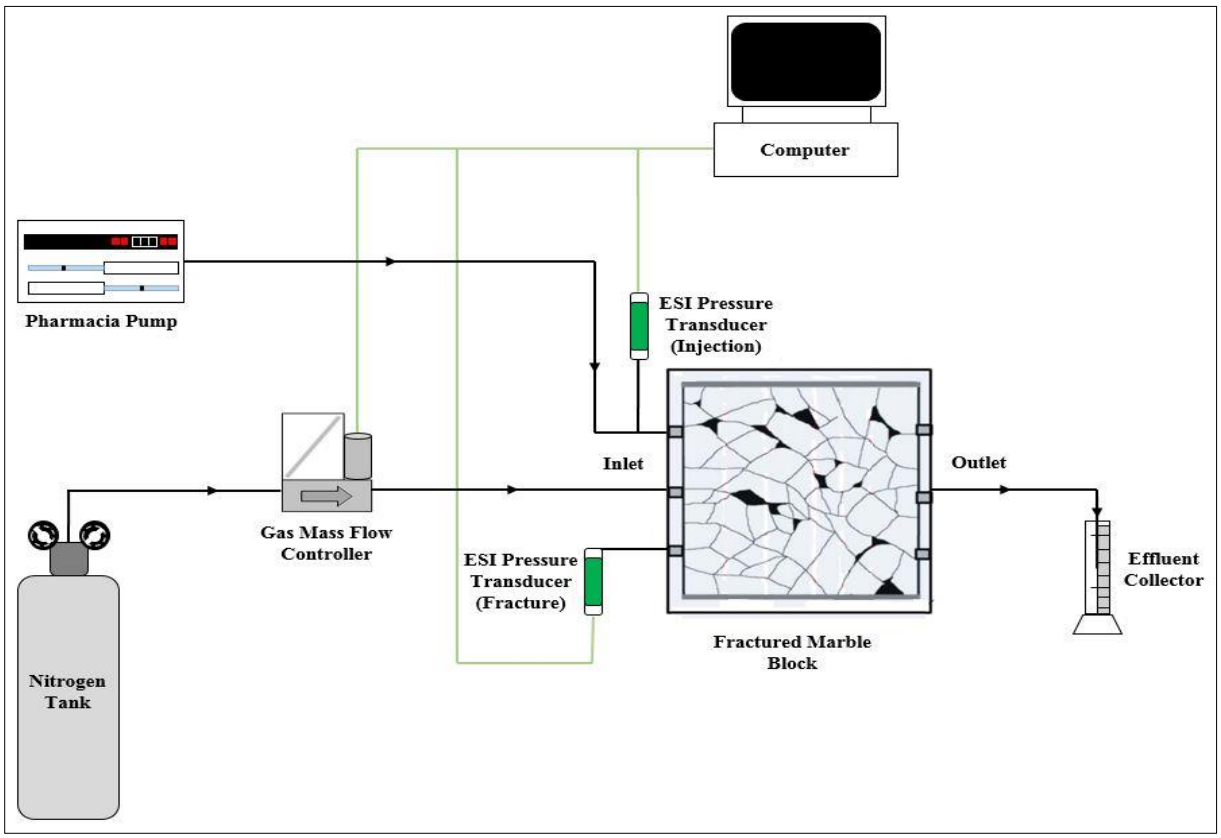

Figure 21: Schematic of the experimental setup used when surfactant solution and gas was coinjected into a fractured marble block. Black lines with arrows indicate the direction of fluid flow inside plastic tubing while the green lines indicate connection cables between devices and a computer. The computer was used to monitor pressure and regulate gas injection rate through a gas mass flow controller.

List of Equipment Used

- Nitrogen tank
- Bronkhorst EL-FLOW® Select Series Mass Flow Meter / Mass Flow Controller
- Pharmacia LKB P-500 pump
- 2 x ESI Digital USB Pressure Transducer, range 0-6 barg ($\pm$ 0.1 % FS)
- Computer used to regulate Mass Flow Controller and record pressure
- 1/16 plastic tubing with Swagelok fittings

7.3.2 Description of Experimental Procedure

The fractured marble network was placed on an elevated platform in advance of each experiment to optimize the field of view through transparent Plexiglas plates covering the model. Coinjections was performed both horizontally and vertically. During horizontal coinjections, the model rested on the platform whereas the vertical coinjections were performed using an upright position (perpendicular to the platform plane), as shown in **Figure 22**. Vertical position facilitates gravitational drag on the injected fluids and makes it possible to observe the effect of gravity on foam distribution inside the fractured network.

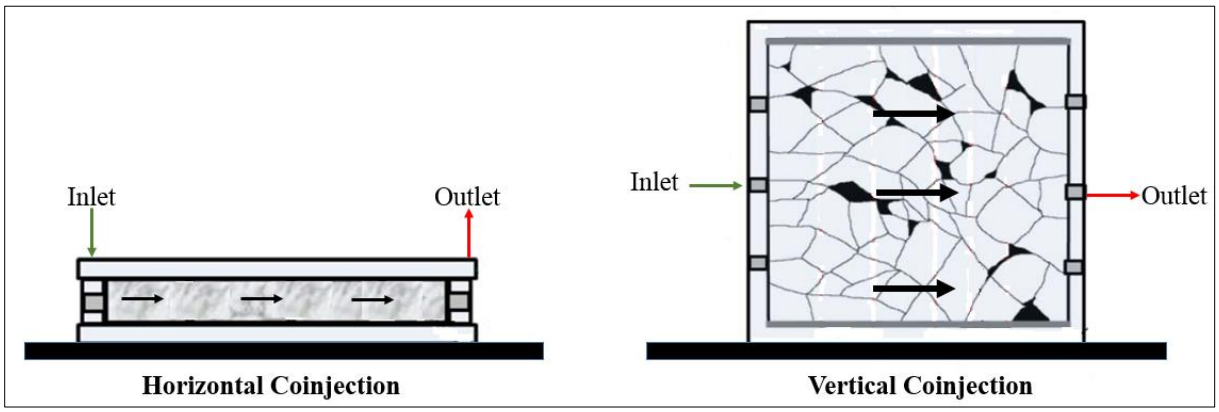

Figure 22: Schematic of horizontal and vertical coinjection configurations. Inlet represents two separate distribution ports located in close proximity to each other and the outlet represent one production port. Black arrows indicate expected direction of flow inside the fractures.

A series of Swagelok distribution ports were available on the inlet side of the model. To ensure rapid mixing between gas and surfactant solution and generate foam, two ports located next to each other were used during coinjection. Unused ports were shut in throughout the experiments to maintain a sealed system. The inlet port for gas received continuous gas from a digitally controlled mass flow controller (Bronkhorst) supplied by a nitrogen tank and the neighboring port received surfactant solution from a pump (Pharmacia). The total rate between gas and surfactant solution was kept constant whereas the amounts of gas/surfactant were regulated in predefined fractions.

Differential pressure was measured to calculate the pressure gradient at each gas fraction. A pressure gradient is given as differential pressure divided by system and was considered more appropriate than differential pressure because it allowed comparison of flow data from different sized systems. Differential pressure was calculated by subtracting the absolute pressure measured with an ESI transducer in the inlet tubing for surfactant with the absolute pressure at the outlet. Because injected fluids were produced directly into an open effluent collector, the outlet pressure was assumed to remain constant at one atmosphere (14.7 psi). An additional ESI transducer was connected directly into the fractured network. Measurements from several locations inside a fractured network may be used to evaluate the hydraulic communication between fractures (Fernø et al., 2016). Almost identical pressure measurements in all experiments suggested good communication between the fractures.

1 wt% brine was injected into the fractured marble network in advance of all experiments to remove remaining surfactant solution and gas from previous coinjections. Immobile gas bubbles were effectively removed when the system was placed in an upright position, injecting from the bottom and producing at the top. The ESI transducers was opened to the room and zero censored before coinjection was initiated. The gas fractional flow was not changed until steady state flow was achieved, i.e. stable flow pressure over a period of time.

Chapter 3: Experimental Results and Discussion

8 Foam Characteristics in Fractured Systems

A total of 13 coinjections were conducted in three different fractured systems to evaluate foam dependency on fracture size and fracture geometry. Raw pressure data from each individual experiment is included in appendix C, and the duration of each gas fractional flow is indicated with black, vertical lines. Uncertainties were calculated in all experiments by equations presented in appendix A. Results from the experiments listed in **Table 4** will be discussed next.

Table 4: Overview of the experiments included in this thesis. System A corresponds to a fractured marble core with a diameter of two inches, System B corresponds to a fractured marble core with a diameter of four inches, and System C corresponds to a fractured marble network (FMN). All experiments were conducted at normal conditions (20 °C and 1 atm).

Fractured system	Coinjection	Rate [ml/min]	Gas	Surfactant	Comment
A (2” core)	0-1	1	Air	Brine	Baseline
A (2” core)	0-1	1	Air	Huntsman	Baseline
A (2” core)	0-1	1	Air	Huntsman	
A (2” core)	0-1	2	Air	Huntsman	
A (2” core)	0-1	3	Air	Huntsman	
A (2” core)	0-1	2.5	Air	Huntsman	
A (2” core)	1-0	2.5	Air	Huntsman	
B (4” core)	0-1	8	Nitrogen	Huntsman	
B (4” core)	0-1	5	Nitrogen	Huntsman	PET/CT exp.
C (FMN)	0-1	3	Nitrogen	Petrostep	Horizontal
C (FMN)	1-0	3	Nitrogen	Petrostep	Horizontal
C (FMN)	0-1	3	Nitrogen	Petrostep	Vertical
C (FMN)	1-0	3	Nitrogen	Petrostep	Vertical

8.1 Foam Characteristics in System A

Coinjections were performed on a fractured marble core with a dimeter of two inches in collaboration with fellow master student Snorre Sande Vasshus. Each experiment used a constant total volumetric rate between gas and surfactant solution (air and 1 wt% Huntsman SURFONIC® in 1 wt% NaCl brine) where gas fractional flow was varied in predefined fractions.

8.1.1 Pressure Fluctuations and Gas Compressibility Effects

Figure 23 show differential pressure as a function of time during an 1 ml/min coinjection of surfactant solution and gas. Vertical black lines are added to indicate the duration of each gas fraction. Fine-textured foam was visually confirmed through a plastic tubing at the outlet, but scattering in pressure made it difficult to analyze flow characteristics. The experimental setup was hence examined to find the cause of the fluctuations. A peculiar trend was identified when movement of foam bubbles inside the outlet tubing was compared with differential pressure. In time intervals of 10-20 seconds, the pressure increased almost exponentially. During pressure buildup, bubbles remained stationary inside the outlet tubing. Suddenly, the pressure dropped and foam bubbles accelerated into the effluent collector at the production outlet. Pressure fluctuations occurred repeatedly during the first two hours of coinjection and increased in magnitude between $F_g = 0.3 - 0.5$. Abrupt changes in foam flow corroborate with findings from Rossen (1988), attributing gas compressibility effects to fluctuations in pressure. If lamellae stop simultaneously in constriction sites of the flow path (e.g. transition zone between wide and narrow fractures), the flow resistance increase significantly. Eventually, gas starts to compress due to elevation in flow pressure. Compression of individual lamella result in an unequal pressure distribution between flowing bubbles, leading to lamella separation and discontinuous flow. Pressure fluctuations could also originate from the viscosity contrast between water and gas. Because injected surfactant solution got a significantly higher viscosity than air, it is possible that a viscous drag between water/gas could separate lamellae at low gas fractions. **Figure 23** display a significant reduction in pressure fluctuation when gas fractional flow was increased from $F_g = 0.5$ to 0.6, suggesting that viscous drag got less impact on foam stability when the amount of gas exceeds surfactant solution. A possible explanation to reduced fluctuation in pressure at high gas fractions is based on the assumption that surfactant solution (water) is more wetting to the fracture walls (calcite) compared to the gas phase (air). At high gas fractional flow, foam flows relatively freely in the center of the fractures with water residing on rock surfaces due to the wetting preference of calcite, leading to stable flow conditions within fractures.

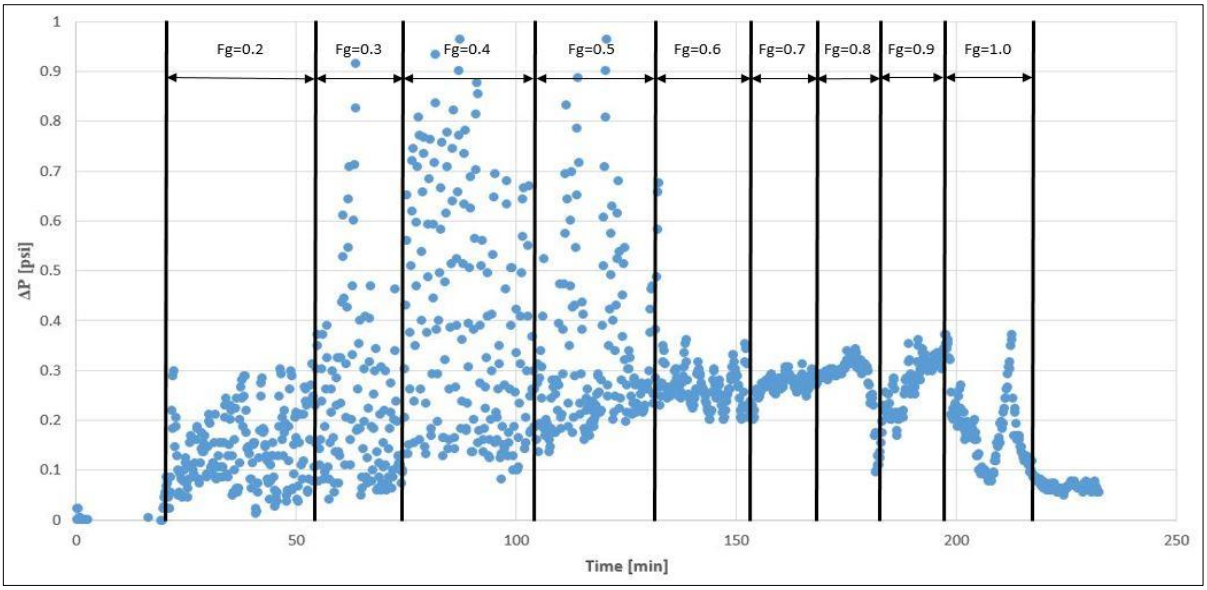

Figure 23: Differential pressure [psi] plotted as function of time [minutes] during F_g 0 − 1 coinjection with a total volumetric rate of 1 ml/min. Black lines represent the duration of each gas fraction. The first two hours was dominated by pressure fluctuation, most likely due to gas compressibility effects. Differential pressure appeared to stabilize at high gas fractions.

Figure 24 shows differential pressure as a function of time during an 1 ml/min coinjection after a backpressure regulator was installed downstream of the fractured core. Constant backpressure appeared to have a positive impact on foam stability, showing reduced fluctuation in pressure compared to the 1 ml/min coinjection without backpressure presented in **Figure 23**. Observations of foam flow inside a plastic tubing at the outlet verified stabilized flow conditions; instead of discontinuous fluid movement, foam maintained a constant velocity. Elevated flow pressure appears to stabilize individual lamella and limit unequal pressure distributions leading to gas compressional effects. A constant backpressure was hence used in a majority of the coinjections presented in this thesis.

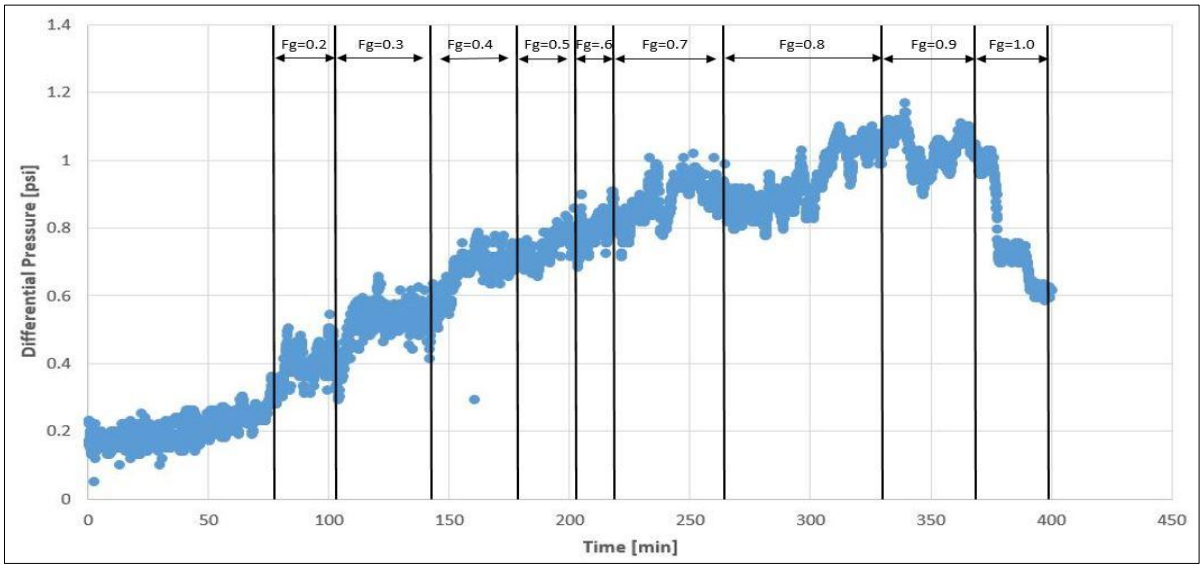

Figure 24: Differential pressure [psi] plotted as a function of time [seconds] during 1 ml/min coinjection after a backpressure regulator was installed. Black arrows indicate duration of each gas fraction, and pressure fluctuations appeared to be significantly reduced.

8.1.2 Baseline Study

A baseline study was carried out to evaluate differences in fluid flow during coinjection with and without surfactant solution present. The baseline used 1 wt% NaCl brine and is represented by black dots in **Figure 25**, displaying averaged pressure gradients for pre-defined gas fractions during $F_g\ 0-1$ coinjection. The baseline show limited increase in pressure between $F_g = 0.2-0.4$. Density difference between gas and water might have caused segregated gas flow in the top of the fractures where increased gas content had little impact on total fluid flow inside the fractures. Elevated pressure at $F_g = 0.5$ (same amount gas/brine injected) corroborates with discontinuity between injected phases where reduced relative permeability increase the flow resistance. Although flow conditions changed towards one-phase flow (i.e. gas) between $F_g = 0.5-0.9$, the pressure appeared to increase almost linearly. This contradicts expected flow behavior in a water-wet system where flowing gas would receive limited flow resistance from water residing on rock surfaces. The significant flow resistance (1.35 psi/ft) at $F_g = 1.0$ (pure gas injection) may be attributed to capillary end effects where water accumulates near the outlet of the core and reduce the relative permeability of gas. However, two factors challenge the validity of the baseline. Firstly, the baseline test in System A was carried out after a series of surfactant/gas coinjections. Mobilization of adsorbed surfactants on rock surfaces could have resulted in generation of foam, and a peak in pressure at $F_g = 0.9$ (1.65 psi/ft) correlates with foam behavior reported elsewhere (Pancharoen et al. (2012) determined $F_g = 0.91$ to result in maximum flow resistance during foam flow in fractures). Removal of surfactants is critical to obtain a representative baseline. For instance, Nguyen et al. (2005) handled surfactant retention by saturating cores with cleaning solvent for 24 hours between foam floods. Secondly, great uncertainties are associated with the averaged pressure gradients in the baseline. Based on observations from **Figure A 3** in Appendix C, differential pressure did not seem to stabilize before gas fractional flow was altered. Limited flow stability was especially apparent at low gas fractions ($F_g = 0.2-0.4$), increasing the uncertainty of the averaged pressure gradients in this flow domain.

The blue dots in **Figure 25** represents an 1 ml/min coinjection with surfactant solution and gas. Elevated pressure at $F_g = 0.2$ (1 psi/ft) compared to the baseline (0.5 psi/ft) is attributed to foam generation immediately after gas entered the system. Although gas constitutes a small fraction of total flow at $F_g = 0.2$, the high transmissivity of the fractures results in effective distribution of gas inside the core. Observation of lamellae inside the outlet tubing after 1.4 pore volumes injected confirms a high gas mobility. Gradual increase in pressure towards a peak at $F_g = 0.8$ (2.2 psi/ft) corroborate with foam behavior described by Kam (2007); with increased gas quality, foam texture change from a wet state where bubbles are well-separated by liquid to dry, gas rich bubbles of uniform size distribution. A high number of bubble films characterizing high-quality foams result in increased flow resistance. Further increase in gas fraction ($F_g > 0.8$) resulted in reduced pressure gradients. Because foam get limited supply of surfactant solution at high gas fractions, lamella starts to thin. Film thinning destabilize foam and results in bubble coalescence and hence reduced flow resistance. Elevated pressure in the baseline compared to the surfactant/gas coinjection at $F_g = 1.0$ is believed to be a result of insufficient flow stability. Comparison of **Figure A 3** and **Figure A 4** show that pure gas injection ($F_g = 1.0$) was maintained for an extended time period in the surfactant/gas coinjection compared to the baseline. Assuming foam was generated during the baseline test, a shorter exposure to pure gas flow could have caused a smaller degree of foam coalescence, leading to increased average pressure gradient compared to the surfactant/gas coinjection.

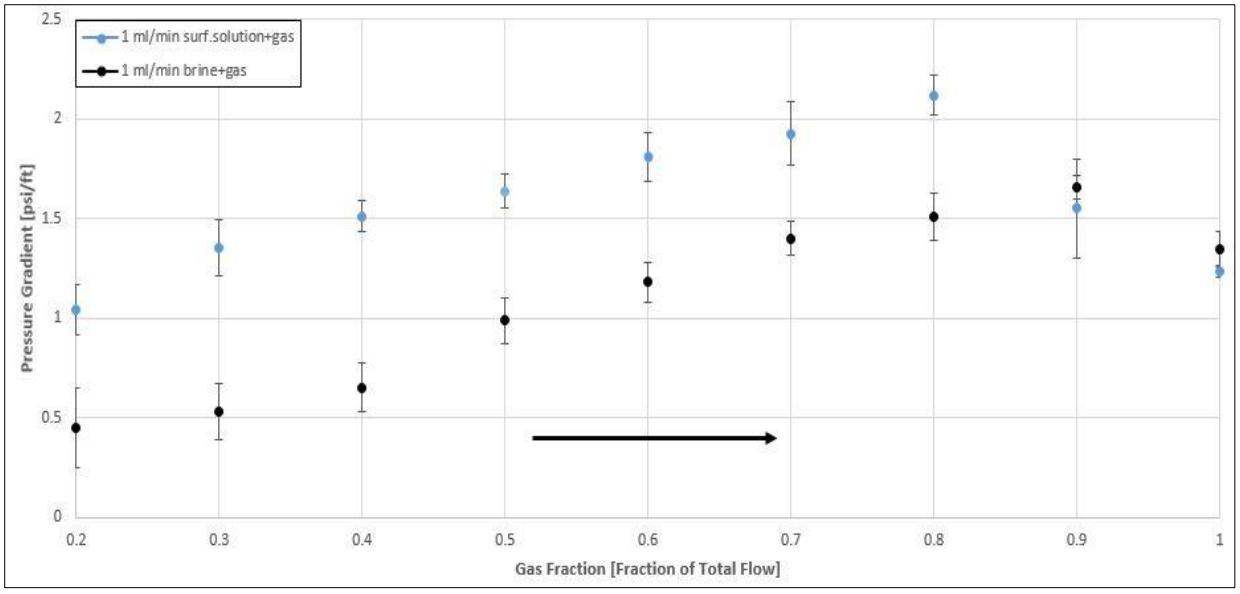

Figure 25: Comparison of pressure gradient [psi/ft] variations with gas fraction between coinjection of brine and gas (black) and surfactant solution and gas (blue). A black arrow indicates the direction of change in gas fractional flow from pure liquid injection ($F_g = 0$) to pure gas injection ($F_g = 1.0$). Included error bars represents standard deviation between averaged pressure gradients at each gas fraction. The baseline had larger uncertainties at low gas fractions due to unstable flow conditions whereas surfactant/gas had varied distribution in uncertainty at different gas fractions.

8.1.3 Foam Dependency on Injection Rate

Foam rheology was investigated by comparing coinjections of different flow rates. Measured differential pressures relate flow resistance to foam quality, and were used to calculate the apparent viscosity of foam. Observation of change in apparent viscosity at different flow rates gives valuable information on shear-stress relations between flowing foam and rock surfaces. In addition, mobility reduction factors for all coinjections presented in this thesis (including System B and System C) were examined.

Figure 26 show three F_g $0-1$ coinjections with different total injection rates ($V_t = 1, 2, 3$ ml/min). Lines between pressure points does not represent measured data but are included to distinguish different coinjections from each other. All pressure gradients increased with gas fractional flow to a peak at either $F_g = 0.8$ or 0.9 before pressure subsequently dropped due to foam coalescence. The maximum pressure gradient seems to depend on total injection rate as $V_t = 1, 2, 3$ ml/min achieved 2.1, 2.2 and 2.5 psi/ft, respectively. Both the 1 and 3 ml/min coinjection peaked at $F_g = 0.8$. This gas fractional flow differs from previous findings on foam flow in fractures. Pancharoen et al. (2012) simulated foam transport in 1D, 2D and radial fractured models and found maximum flow resistance to occur at $F_g = 0.91$. At this gas fraction, foam texture change from spherical bubbles to polyhedral bubbles. Because simulations were based on several assumptions (e.g. constant fracture aperture, atmospheric outlet pressure and a gas/water end-point relative permeability of 1), it is difficult to relate observed foam behavior directly to data from System A. The coinjections in **Figure 26** occurred in rough-walled fractures of varied aperture, yielding a significant drag on flowing fluids. A possible explanation to increased foam strength at $F_g = 0.8$ compared to $F_g = 0.9$ (for $V_t = 1, 3$ ml/min) is based on an interesting observation made by Kovscek et al. (1995) studying foam flow through a transparent, rough-walled fracture. At low gas fractions (i.e. wet texture), foam maintained a relatively high flow velocity within the fracture. The high mobility was thought to be a result of liquid exchange

between lamella and the rock, effectively lubricating the rough fracture walls. A higher liquid content at $F_g = 0.8$ compared to $F_g = 0.9$ could have resulted in lubrication of rough fractures walls, reducing the shear-stress between flowing lamellae and rock surfaces. The 2 ml/min coinjection (orange) had a lower pressure gradient at $F_g = 0.1$ (0.35 psi/ft) compared to the 1 and 3 ml/min coinjections, most likely due to delayed zeroing of the ESI pressure transducers in the 2 ml/min coinjection. However, a similar trend with increased pressure gradient with increased gas fractional flow suggests that similar flow conditions were obtained and that the coinjections are comparable.

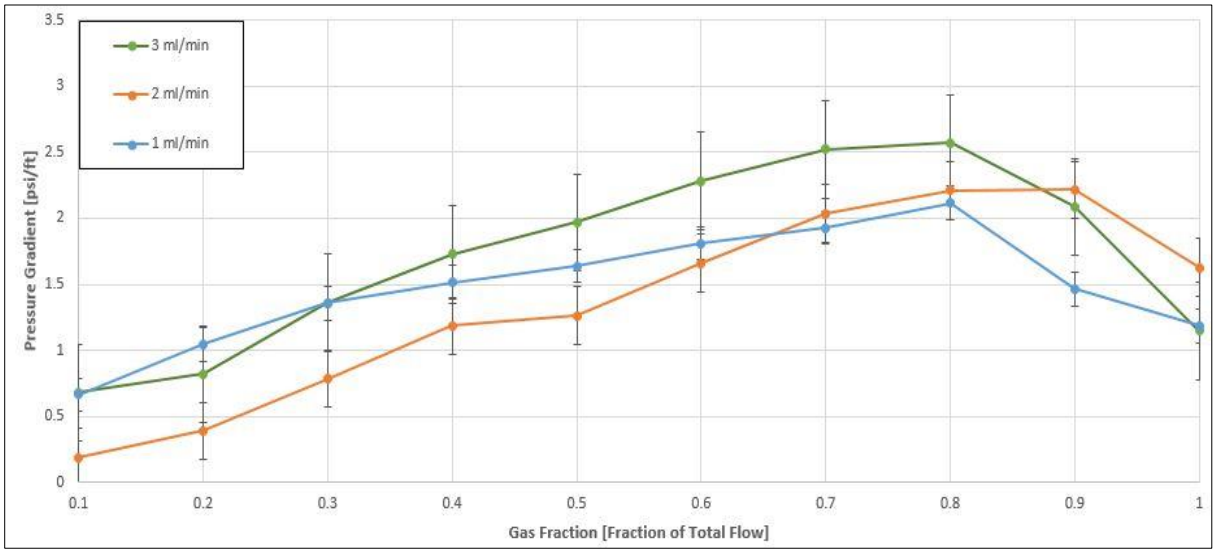

Figure 26: Pressure gradients [psi/ft] as a function of gas fractional flow during F_g 0 − 1 coinjections of various total injection rates ($V_t = 1, 2, 3$ ml/min). Lines between the pressure points does not represent measured data but are added to distinguish different experiments from each other. Included uncertainties are calculated as the standard deviation of the averaged pressure data representing each gas fraction, and increased with increased total injection rate.

Apparent viscosity, μ_f^{app}, was calculated using equation (2) where the product between absolute permeability of System A (3.9 Darcy) and pressure gradient was divided by superficial flow velocity (1,2, and 3 ml/min). **Figure 27** display apparent viscosity as a function of gas fractional flow. The apparent viscosity reached a maximum at high gas fractional flow in all three coinjections. This corroborates with generation of fine-textured foam of significant viscosity, inducing elevated flow resistance within the fractures. However, foam had a significantly higher apparent viscosity during 1 ml/min flow compared to the 2 and 3 ml/min coinjections. Decreasing apparent viscosity with increased total flow rate suggest a reduction in foam strength due to shear thinning (Allen, 1995). Increased flow rate result in a larger shear-stress between lamella and rock (i.e. rough fracture surfaces), leading to separation of bubbles. Although a flowing lamella constitutes a dynamic system that could stretch and regulate its surface area to maintain flow (e.g. through fractures with variations in fracture aperture), the rough fracture walls in System A seem to have a devastating effect on foam at high injection rates.

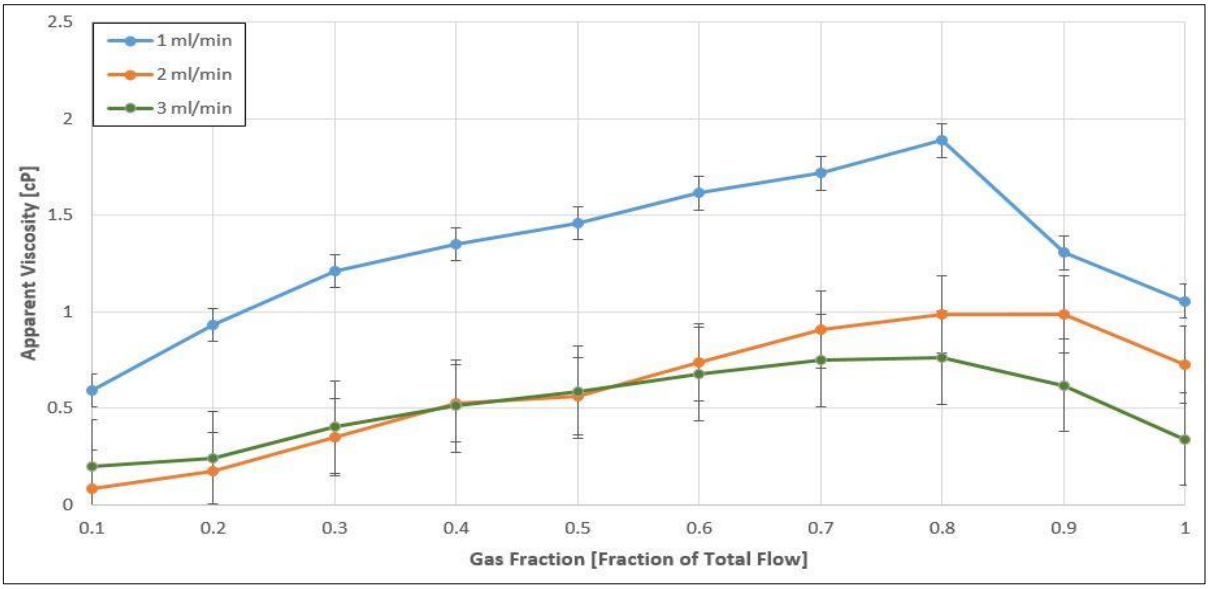

Figure 27: Apparent viscosity [cP] as a function of gas fractional flow. The lowest injection rate (1 ml/min in blue) had the highest apparent viscosity of the different coinjections. Reduced apparent viscosity with increased flow rate suggests shear thinning of the foam. Error bars are included to indicate uncertainties in apparent viscosity at different flow rates, and are based on standard deviations in the averaged pressure gradients.

The mobility reduction factor (MRF) quantify the ability of foam to reduce gas relative permeability within fractures and was calculated for the $V_t = 1, 2, 3$ ml/min coinjections as the ratio between the apparent viscosity of foam and the viscosity of the injected gas (air), i.e. reconfiguration of equation (4). In addition, MRF was calculated for coinjections in System B and System C. **Figure 28** show variations in MRF with total flow rate at high foam qualities ($F_g \geq 0.6$). MRF values from the low foam quality domain ($F_g \leq 0.5$) are not included because variations of volumetric rate at high liquid content seems to have little impact on MRF (Buchgraber et al., 2012). Note that x and y axis are logarithmic, making it easier to observe change in MRF at various injection rates. A negative slope in the included trendline indicate a decreased mobility reduction with increased injection rate for all fractured systems evaluated in this thesis. This suggests shear thinning of foam in fractured marble systems and correlate with findings from Fernø et al. (2016). However, significant variations in MRF at 3 ml/min coinjection show that there are differences in foam rheology between different-scaled systems. Thus, apparent viscosity measurements will be discussed for both System B and System C.

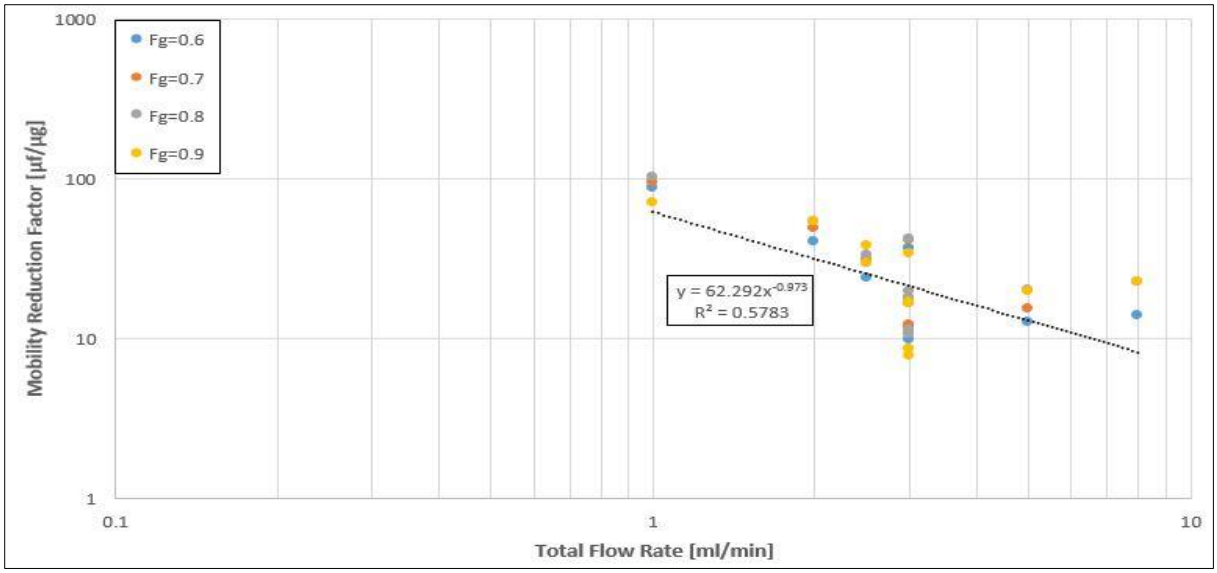

Figure 28: Mobility reduction factor (MRF) plotted as a function of total flow rate [ml/min] in a logarithmic axis configuration. MRF decreased with increased flow rate, indicating shear thinning of foam behavior in fractured marble systems. A power-trendline was included to indicate the decline in MRF. Trendline equation and R^2 value are shown in the box below the plotted data.

8.1.4 Alternation in Gas Fractional Flow

Coinjection order was varied to evaluate foam dependency on saturation history. **Figure 29** shows pressure gradients of two coinjections using a total rate of 2.5 ml/min with opposite variations in gas fractional flow. $F_g\ 0-1$ (blue curve) represents a coinjection from pure surfactant injection ($F_g = 0$) to pure gas injection ($F_g = 1.0$), and display a characteristic increase in pressure gradient with increased gas fractional flow to a peak at $F_g = 0.9$ (2 psi/ft). Dry foam and lamella coalescence at $F_g = 1.0$ resulted in a final pressure gradient of 1.5 psi/ft. A $F_g\ 1-0$ coinjection (red curve) was conducted immediately after the $F_g\ 0-1$ coinjection, indicated by a similar pressure gradient at $F_g = 1.0$. In contrast to the $F_g\ 0-1$ coinjection where pressure showed a strong dependence on foam quality, the $F_g\ 1-0$ coinjection show limited variations in pressure as gas fractional flow is reduced towards $F_g = 0$. Deviation in pressure development between the curves suggests hysteresis related to saturation history within the fractured core. A possible explanation to hysteresis in the $F_g\ 1-0$ coinjection is accumulation of immobile, trapped gas within fractures during the $F_g\ 0-1$ coinjection performed in advance. Trapped bubbles of gas situated in the center of fractures reduce the relative permeability of flowing liquid/gas and result in significant flow resistance. Because pressure remained relatively constant with increased liquid flow (i.e. decreased gas fractional flow), trapped foam bubbles appears to have a significant resistance against viscous drag from flowing water inside the fractures.

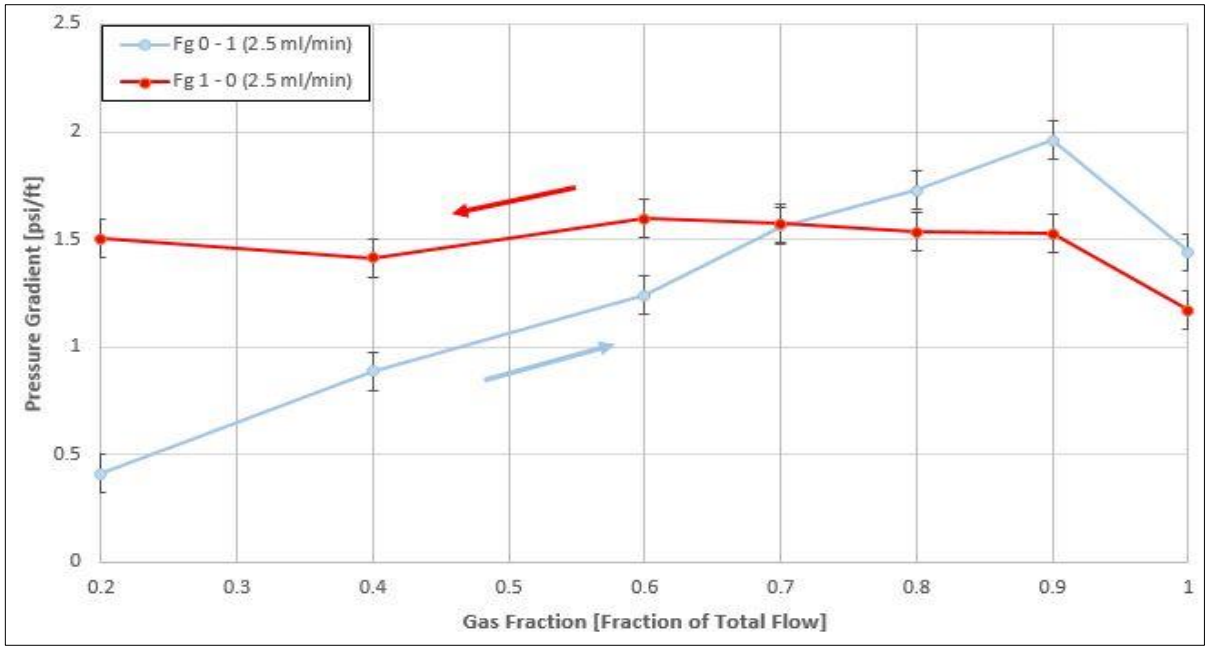

Figure 29: Pressure gradient [psi/ft] as a function of gas fraction during F_g 0 − 1 and F_g 1 − 0 coinjection using a total volumetric flow rate of 2.5 ml/min. The blue curve represents the Fg 0 – 1 coinjection, changing from no fractional gas flow initially to 100 percent gas flow in the end. The opposite coinjection, Fg 1 – 0 is shown as a red curve. Representative arrows are included to indicate the direction of changes in gas fractional flow. Hysteresis between the curves is believed to be result of saturation history and presence of trapped gas. The error bars in each pressure point are calculated from the uncertainty given by the manufacturer of the ESI transducers.

8.2 Foam Flow in System B

Similar coinjection experiments were conducted in an up-scaled system using a fractured marble core with a diameter of four inches. The objective was to evaluate whether a greater system size changed foam rheology and flow characteristics or if foam flow occurred similar to coinjections in System A. To make the systems comparable, the same liquid (1 wt% Huntsman SURFONIC® in 1 wt% NaCl brine) were used, together with a constant total rate and F_g $0-1$ alteration in gas fractional flow. In addition, an imaging study of foam distribution within fractures was carried out using PET/CT technology.

Figure 30 shows pressure gradient as a function of gas fractional flow during a F_g $0-1$ coinjection in System B. Use of a relatively high total volumetric rate (8 ml/min) resulted in a pressure gradient of 1.3 psi/ft at $F_g = 0$. Increased gas fractional flow between $F_g = 0-0.6$ caused a steady increase in pressure. After $F_g = 0.6$, however, the mass flow controller (MFC) was unable to provide sufficient gas flow due to elevated flow pressure, and predefined gas fractions were reduced to maintain flow. Adjusted gas rates are presented in **Table 5** and resulted in an averaged total flow rate of 6.8 ml/min. Differential pressure data in **Figure A 8** clearly indicate a decrease in pressure when total flow rate was changed from 8 ml/min to 6.8 ml/min 130 minutes into the coinjection. Pressure gradients at $F_g = 0.8, 0.9,$ and 1.0 were scaled with pressure data from the same gas fractions in a 5 ml/min coinjection. Although a scaling procedure involves a high degree of uncertainty, it gives an estimate of pressure variations at high gas fractional flow during 8 ml/min coinjection. Estimated pressure gradients are indicated with gray arrows and appeared to be almost identical at $F_g = 0.8$ and 0.9, suggesting a somewhat uniform foam stability at two different gas fractions. This was likely due to insufficient stabilization in flow before gas fractional flow was altered as foam texture and strength is known to be highly dependent upon gas fractional flow. Pressure gradient was reduced when gas fractional flow was increased at $F_g = 1.0$, corroborate with dry foam and bubble coalescence.

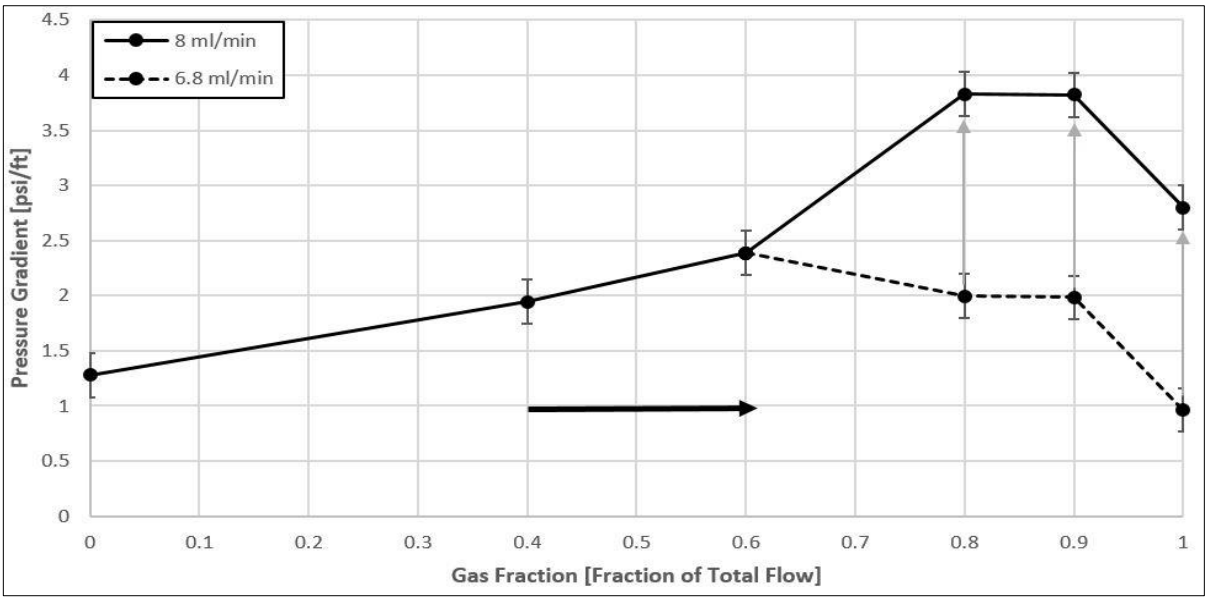

Figure 30: Pressure gradient [psi/ft] as a function of gas fractional flow during F_g $0-1$ coinjections with a total volumetric rate of 8 ml/min in System B. A black arrow is included to clarify the direction in change of gas fractional flow. The solid section of the curve represent 8 ml/min flow with scaled pressure gradients at $F_g = 0.8, 0.9,$ and 1.0, whereas the dotted line represents measured pressure after total volumetric flow was reduced to 6.8 ml/min total due to technical difficulties with the gas mass flow controller. Included error bars are based on standard deviation in the averaged pressure gradients.

Table 5: Variations in total volumetric flow [ml/min] during 8 ml/min coinjection in System B. Italicized numbers represents adjustments in gas fractional flow resulting in reduced total flow.

8 ml/min F_g 0 − 1 coinjection					
Gas fraction [fraction of total flow]	0.4	0.6	0.8	0.9	1
Surfactant solution rate [ml/min]	4.8	3.2	1.6	0.8	0
Gas rate [ml/min]	3.2	4.8	*5.7*	*6.0*	*6.2*
Total flow rate [ml/min]	8	8	7.3	6.8	6.2

A F_g 0 − 1 coinjection with a total flow rate of 5 ml/min is presented in **Figure 31**. Reduction in flow rate (i.e. from 8 ml/min) was believed to result in flow pressures below the boundary of the mass flow controller. The coinjection showed steady increase in pressure with increased gas fractional flow and correlates well with the first section of the 8 ml/min coinjection. Increased gas content between $F_g = 0.7$ and $F_g = 0.8$ resulted in a significant elevation in flow pressure, suggesting generation of fine-textured lamella.

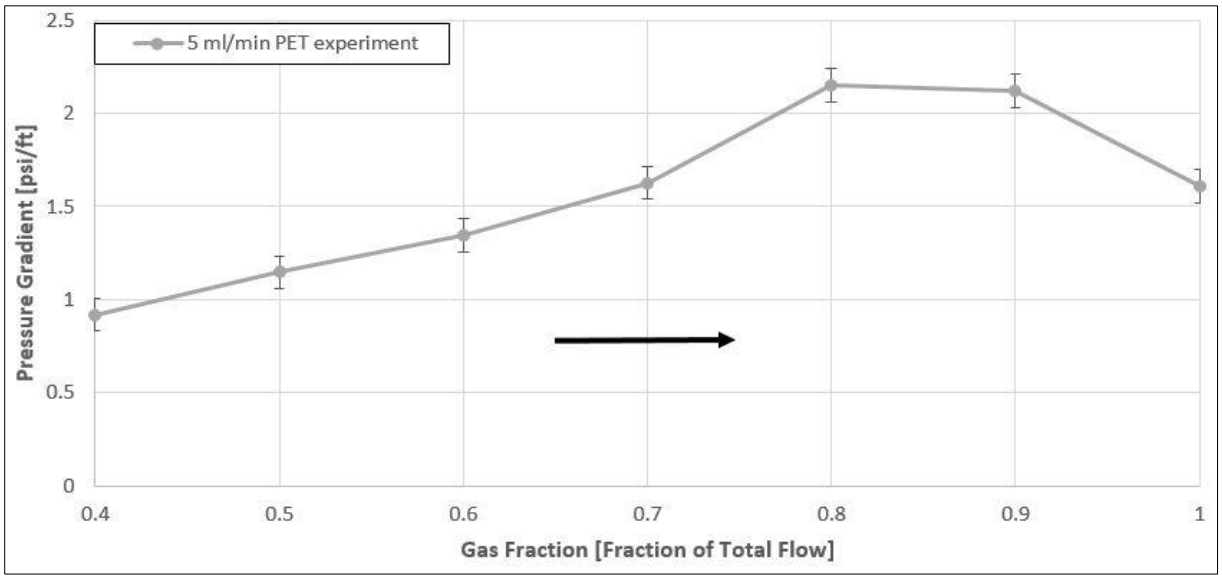

Figure 31: Pressure gradient [psi/ft] as a function of gas fraction during a F_g 0 − 1 coinjection with 5 ml/min total volumetric rate. The black arrow indicates the direction of change in gas fractional flow. Included uncertainties are based on standard deviation in the averaged pressure gradients.

The 5 ml/min coinjection discussed above was conducted in the imaging lab at the Haukeland University Hospital. Application of a combined PET/CT scan during coinjection made it possible to visualize foam flow and fluid distribution inside the fractured core. The following section summarize the experimental findings from PET/CT imaging in System B.

8.2.1 Fracture Characterization of System B Using X-ray Computed Tomography

A CT scan of high resolution (0.6 mm x 0.6 mm x 0.6 mm) was performed on System B before the coinjection to identify fractures where fluid flow was likely to occur. Thin 2D slices of the entire fractured core (35 cm) was converted to a 3D image using Amira 3D software. **Figure 32** show a cropped 3D picture of System B and indicates substantial fractures in the center of the core.

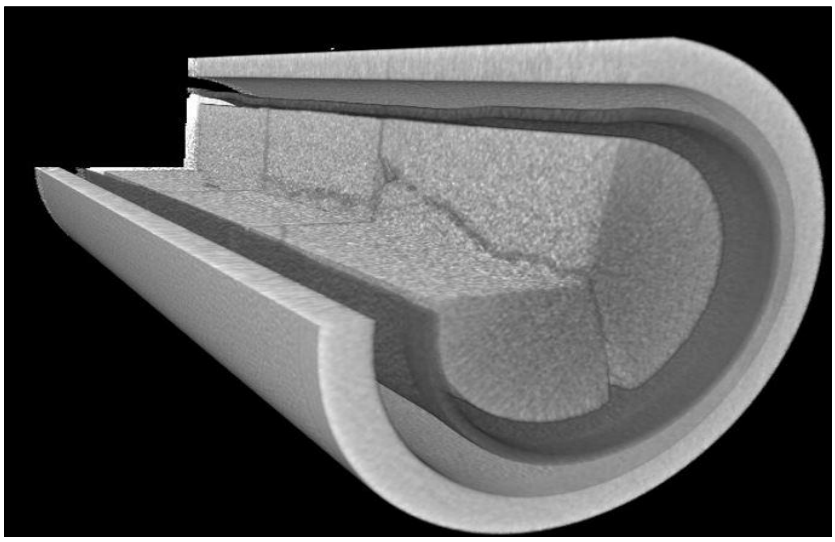

Figure 32: High resolution dryscan (0.6 mm) of the entire fractured core in System B. The white layer surrounding the core represents the Hassler core holder. Major fracture patterns are clearly visible through the core.

PET images have a lower resolution (2.0 mm x 2.0 mm x 0.6 mm) with a limited field of view (FOW) of 16.6 cm consisting of 83 slices. **Figure 33** shows a side-view of the total fractured core with inlet on the right and outlet to the left. PET field of view is shown in red and two major fractures, F1 and F2, are indicated in green.

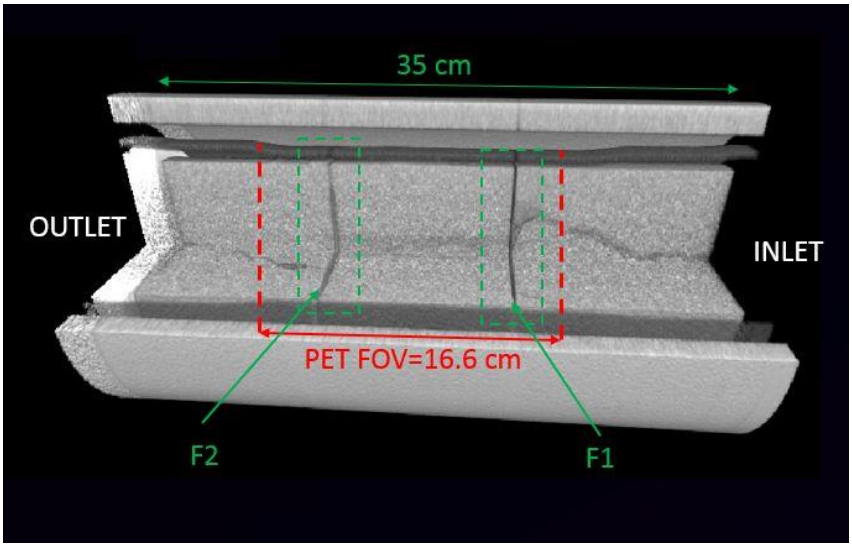

Figure 33: High resolution CT image of System B. PET field of view is given in red and include two major fractures referred to as F1 and F2. The coinjected fluids enters System B from the right and flow towards the outlet on the left.

8.2.2 Visualization of Foam Flow Using Positron Emission Tomography

Positron emission tomography was used to visualize fluid flow inside the fractures at specific gas fractions during the 5 ml/min coinjection in System B. Surfactant solution was labelled with a radioactive isotope (^{18}F), and emitted gamma rays were measured by a PET scanner over an 8-hour period. The number detected gamma rays, referred to as counts, are hence proportional to liquid content. **Figure 34** shows variation in counts as a function of normalized system length (i.e. over the PET field of view) where position $X_L = 0$ indicates the outlet and $X_L = 1$ represent the inlet. Gamma activity was particularly high at $X_L = 0$, $X_L = 0.3$, and $X_L = 0.8$, indicating areas with increased fracture volume storing radioactive surfactant solution. Visual comparison with **Figure 33** suggests that $X_L = 0$ corresponds to the parallel fracture near the center of the core, $X_L = 0.3$ to the perpendicular fracture F2 and $X_L = 0.8$ to the perpendicular fracture F1.

Measured gamma activity for $F_g = 0.4$ is represented in pink, and indicates a significant PET signal from the perpendicular fractures F1 and F2 compared to inlet ($X_L = 1$) and outlet ($X_L = 0$). In fact, the highest measured gamma count in fracture F1 was obtained at $F_g = 0.4$, suggesting significant accumulation of radioactive ^{18}F within fractures oriented perpendicular to the flow path. When gas fractional flow was increased at $F_g = 0.6$ (orange curve), PET signal was reduced in F1 and F2. Reduced liquid content within large, vertical fractures at increased gas flow (i.e. enhanced foam quality), suggests that liquid was displaced by foam distributing into new pathways. At $F_g = 0.9$ (blue curve), surfactant saturation increased in F1 and F2. In addition, PET signal increased significantly between $X_L = 0 - 0.3$, $X_L = 0.3 - 0.8$, and $X_L = 0.8 - 0.9$. A possible explanation to elevated gamma activity at high gas fractional flow is discussed below.

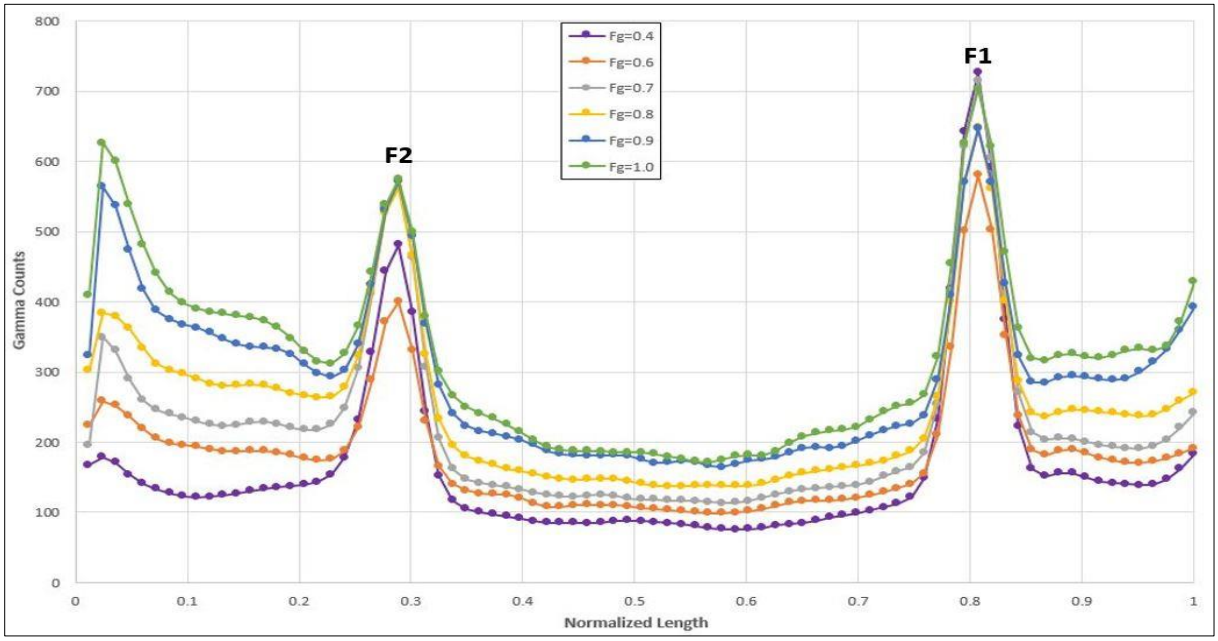

Figure 34: PET counts as a function of normalized length over the PET field of view in System B. Measured PET signal as a function of length gives valuable information regarding distribution of radioactive FDG at different gas fractions during coinjection. Peaks labelled as F1 and F2 was identified as large, vertical fractures oriented perpendicular to the flow path through CT images of System B. Increased gamma activity in F1 and F2 are believed to come from extensive storage space facilitating trapping of immobile, radioactive tracers.

The apparent increase in PET signal over the length $X_L = 0 - 1$ between $F_g = 0.6$ to $F_g = 0.9$ indicate an higher saturation of radioactive ^{18}F at high gas fractional flow. This may seem strange as ^{18}F was injected through the aqueous phase (i.e. surfactant solution), constituting 10 percent of the total volumetric fluid flow injected at $F_g = 0.9$. However, pressure data in **Figure 35** plotted together with the sum of PET counts in **Figure 34** indicate that the highest flow resistance was obtained at high gas fractional flow. Kovscek et al. (1995) observed lamella to remain stationary and bridge fracture aperture at high gas fractional flow in rough-walled fractures. Because ^{18}F is present on lamella, increased levels of stationary foam at high gas fractional flow could have increased the PET signal. Stationary foam may also entrap concentrated surfactant in vugs by sealing off communicating fractures. To validate this possibility, a PET image montage was created to visualize fluid distribution in 3D space. All images in **Figure 36** were captured at time intervals where pressure seemed to stabilize, indicating stabilized flow conditions representative of each gas fractional flow.

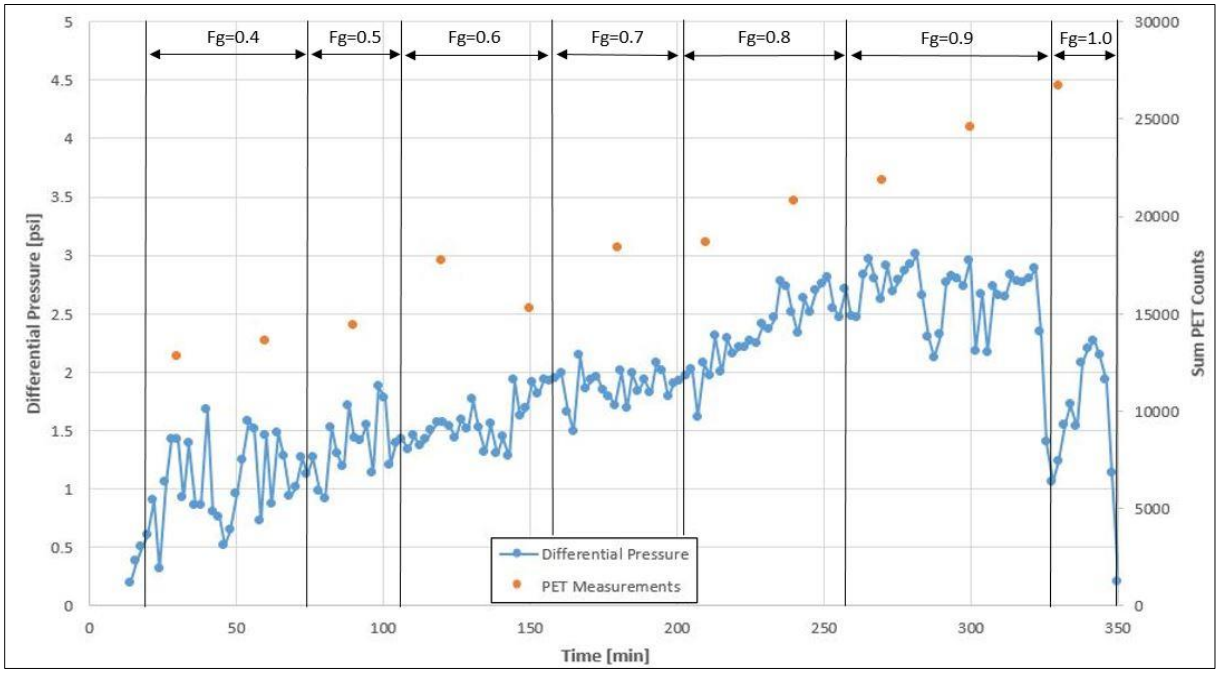

Figure 35: Differential pressure [psi] and total PET count over ten minutes intervals are plotted as a function of time [min]. Measured gamma activity appeared to increase with gas fractional flow (and pressure). A possible explanation to this development are based on a higher degree of stationary, trapped fluids at high gas fractional flow compared to flow at lower gas fractions.

Figure 36 display variations in PET signal in 3D space at different gas fractions. Red color indicates high ^{18}F concentration and blue color represents low ^{18}F concentration. At $F_g = 0.4$, concentrated signal is observed F1 and F2, and coincide with accumulation of surfactant solution in perpendicular fractures at low gas fractional flow as discussed earlier. ^{18}F appeared to be well-distributed in vertical direction in F1, and may suggests that presence of foam outside the fracture prevents liquid to accumulate in the bottom of the fracture from gravity pull. At $F_g = 0.9$, ^{18}F concentration was lowered in F1 (indicated with a green color) whereas F2 seemed to contain a similar concentration as for $F_g = 0.4$. However, PET signal was detected in several locations new locations compared to $F_g = 0.4$, for instance at $X_L = 0$ and between $X_L = 0.8$ and 1.0. Elevated distribution in PET signals indicate increased propagation of foam inside fractures and diversion of flow into previously untouched zones. Increased amounts of foam within major flow fractures may also trap surfactant in vugs, resulting in elevated PET count. Reproduction of PET experiments is however necessary to draw conclusions.

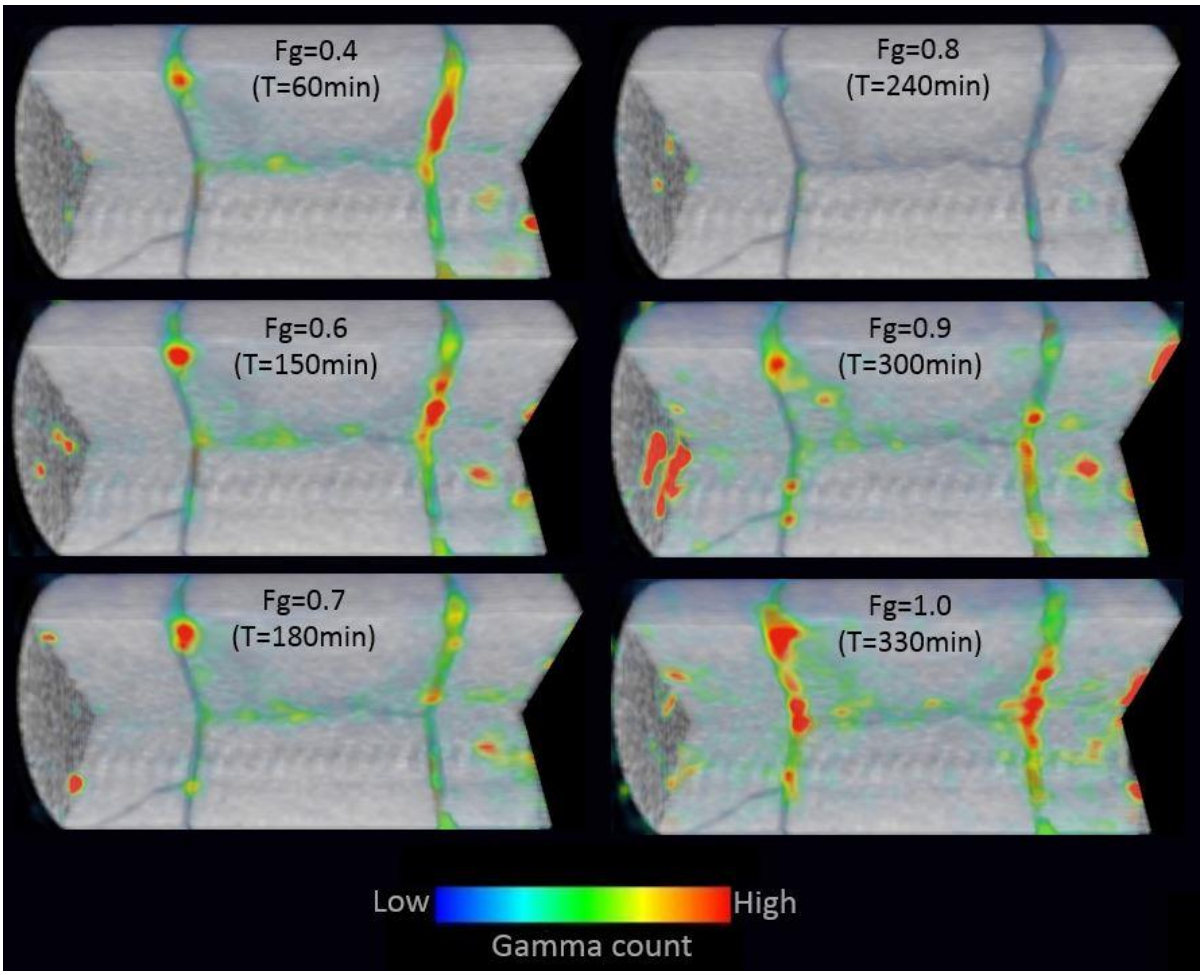

Figure 36: 3D representation of ^{18}F distribution inside System B during foam flow. Red color indicates a high count and presence of ^{18}F whereas blue color indicates low gamma activity. Increased distribution of immobile, trapped foam at high gas fractional flow was believed to result in increased ^{18}F concentration.

8.2.3 Impact of Up-Scaling on Fractured Marble Cores

Figure 37 show measured pressure gradients at different gas fractions in System A and System B. Green colored curves represent coinjections in System A whereas blue curves corresponds to coinjections in System B. All coinjections appear to follow a similar trend: the pressure gradient increases with enhanced foam quality (i.e. gas content) and peaks at either $F_g = 0.8$ or $F_g = 0.9$, before the pressure declines during pure gas injection at $F_g = 1$. The pressure gradient for the 8 ml/min coinjection in System B (dotted blue curve) appeared to result in greater pressure gradients compared to coinjections at lower flow rates. However, there is a significant uncertainty related to the pressure gradients for 8 ml/min pressure data at $F_g < 0.6$ as these were estimated by scaling equivalent pressures obtained during 5 ml/min coinjection. Good overall correlation between the different sized systems (2" and 4" cores) imply that the generated foam is relatively independent on fracture size (in terms of fracture length) and that Huntsman surfactant could be used as a foam stabilizer in fractured systems having both intermediate and large fractures.

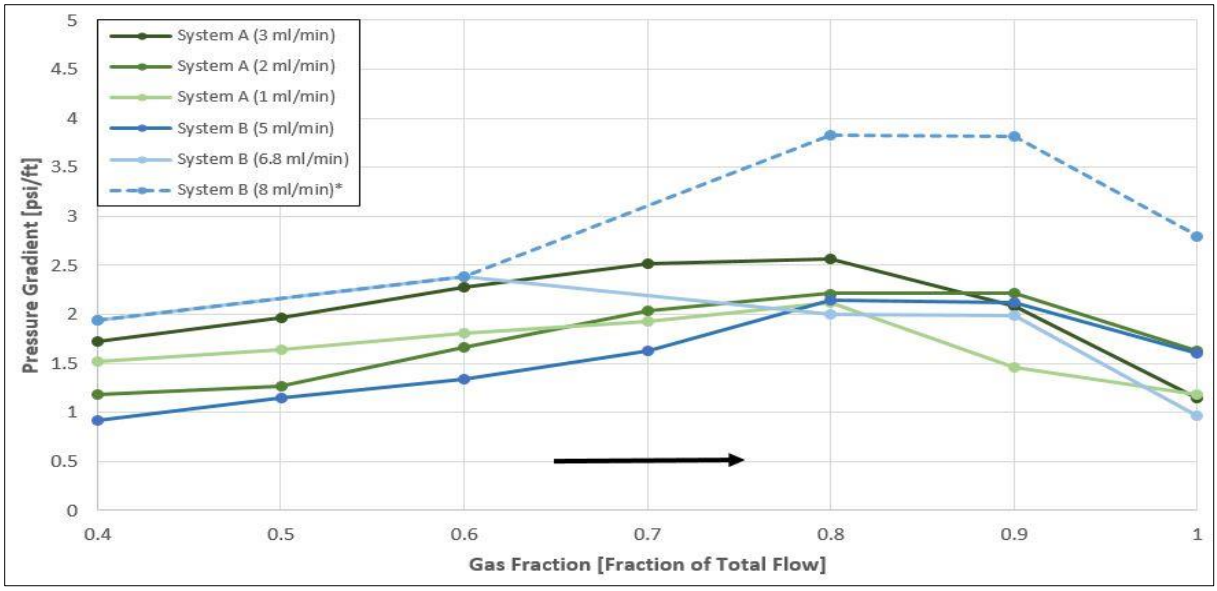

Figure 37: Comparison of various F_g 0 − 1 coinjections from System A and System B. Green curves represent System A and blue curves represent System B. The black arrow indicates that the coinjections was changed from pure surfactant solution injection $F_g = 0$ to pure gas injection $F_g = 1.0$. The pressure gradient caused by foam seem independent on fracture size.

Because injection rate was varied between coinjections in System A and B, foam rheology could be evaluated. Apparent viscosity calculations for System B are based on an averaged absolute permeability between System A and C because routine core analysis has not yet been established. Apparent viscosity as a function of gas fraction is presented in **Figure 38**, and indicates reduced viscosity of foam at increased flow rates. This corroborates with shear-thinning and suggests that drag between foam and rough fracture walls reduce foam stability and hence the ability to control gas mobility in different sized fractured cores at elevated flow rates.

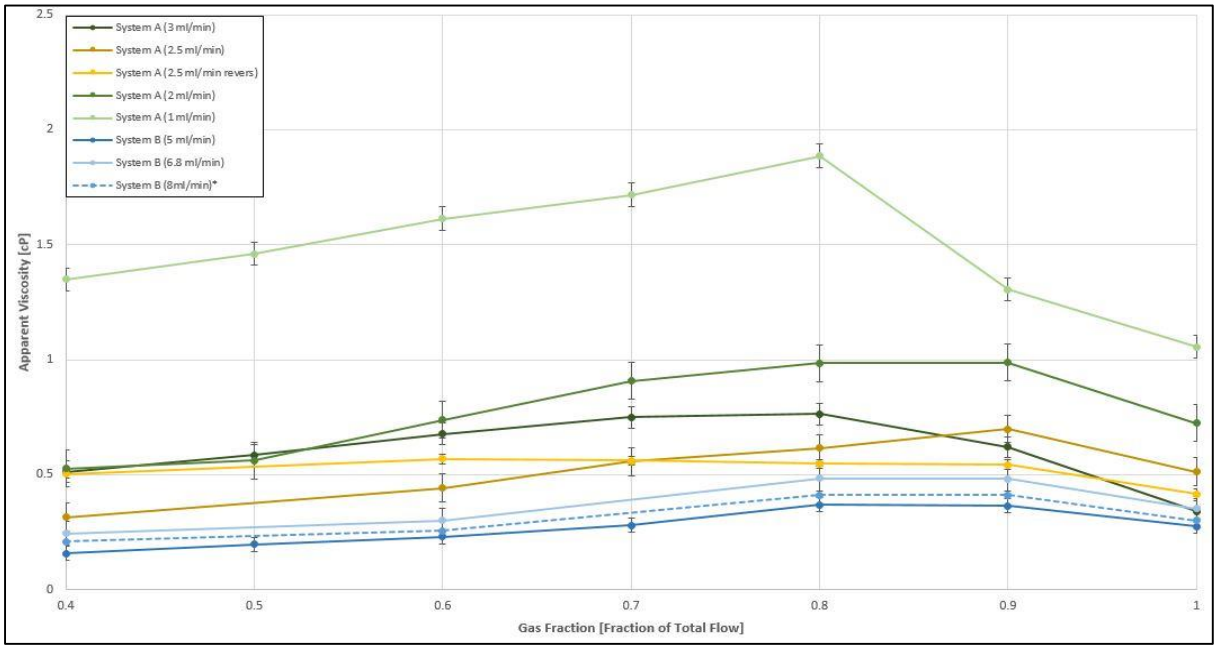

Figure 38: Comparison of apparent viscosity as a function of gas fractional between System A and B. Viscosity decreased with increased flow rates and indicates shear-thinning of foam. Uncertainties included as error bars are based standard deviation in pressure gradients calculated from equation (A3) in appendix A and the uncertainties in absolute permeability, calculated with equation (A1) in appendix A.

8.3 Foam Characteristics in System C

A fractured marble network was used to evaluate foam flow in a complex fracture pattern spanning a surface area of 31.2 cm x 31.2 cm. A total of four successful experiments were conducted in collaboration with fellow master student Snorre Sande Vasshus on the fractured marble network, all with a constant volumetric rate of 3 ml/min and pre-defined regulations in gas fractional flow. The network was positioned both horizontally and vertically during coinjection to evaluate influence of gravity.

8.3.1 Horizontal Coinjection

Pressure gradient is plotted as a function of gas fraction in **Figure 39**. The dark blue curve represents a F_g 0 – 1 coinjection, and an initially low pressure gradient (0.2 psi/ft) was expected because the system was liquid filled before gas subsequently entered the system to generate foam. Steady increase in pressure with increased gas fraction was consistent with generation of foam, and lamellae were observed in large vugs at $F_g = 0.1$. The highest pressure gradient (1.13 psi/ft) was measured at $F_g = 0.8$, implying that foam induced the greatest flow resistance at a quality of 80 percent. Further increase in gas fraction resulted in a decrease in pressure. F_g 1 – 0 (light blue) represents the same experiment performed in opposite injection order, moving from right to left in **Figure 39**. Both curves share a similar trend in pressure gradient variation with gas fractional flow, indicating limited hysteresis compared to **Figure 29** in System A. A likely explanation to limited hysteresis effects in System C is that the model was pre-flushed with brine between coinjections to remove remaining trapped gas, reducing the relative permeability of gas by blocking flow pathways (Kovscek and Radke, 1993). By injecting brine from the bottom-up with the system oriented in vertical direction, gas bubbles were observed to flow to flow towards the outlet port. In System A, the F_g 1 – 0 coinjection were carried out directly after an F_g 0 – 1 coinjection, leaving trapped gas saturation within the fractures.

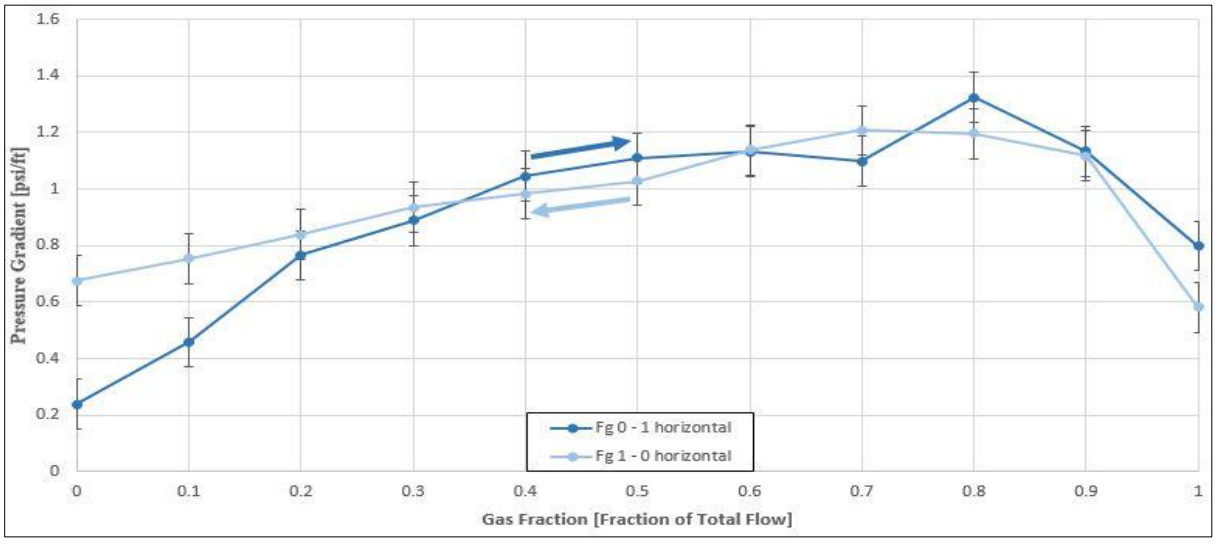

Figure 39: Pressure gradient [psi/ft] as a function of gas fraction during coinjection of surfactant solution and nitrogen gas into a horizontally positioned fractured marble network. The dark blue curve represents a (Fg 0 – 1 horizontal) coinjection, changing from no fractional gas flow initially to 100 percent gas flow in the end. The opposite coinjection, (Fg 1 – 0 horizontal) is shown as a light blue curve. Representative arrows are included to indicate the direction of changes in gas fractional flow. The error bars in each pressure point are calculated by standard deviation in averaged pressure gradients using equation (A3) in appendix A.

Foam texture depends on gas fractional flow and was visually inspected during the horizontal coinjections. **Figure 40** shows variations in foam texture at different gas fractions for Fg 0 – 1 horizontal. The foam observed at $F_g = 0.7$ and $F_g = 0.8$ consisted of fine, polyhedral bubbles with a relatively homogeneous size distribution. Grundmann and Lord (1983) characterize fine textured foam as particularly resistant and strong due to a high number of film faces. Polyhedral foam was observed throughout the fractured marble network, predominantly in the largest vugs. Because foam occupied major flow paths, flowing gas experienced increased resistance and had to overcome a higher capillary entry pressure to advance further. This is apparent in F_g $0 - 1$ coinjection in **Figure 39**, with a peak in pressure gradient at $F_g = 0.8$. A decrease in pressure at $F_g = 1.0$ occurred when the foam texture coarsened and is likely a result of dry foam conditions. Reduced exchange of surfactant solution between a Plateau border and lamella at high gas fractions may results in film thinning and eventually film rupturing at a limiting capillary pressure (Farajzadeh et al., 2015). $F_g = 1.0$ in **Figure 40** is an example of coarse foam where small bubbles has coalesced into large bubbles that span over the entire length of the vug.

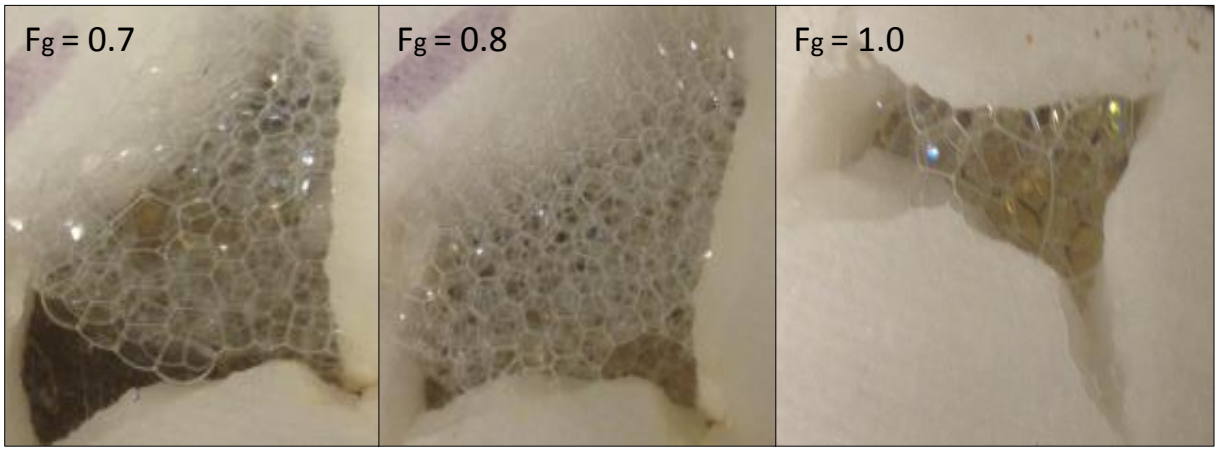

Figure 40: Foam texture at different gas fractions during Fg 0 – 1 coinjection. Foam texture changed from a uniform, polyhedral geometry at $F_g = 0.7$ and $F_g = 0.8$ to a unstable coarse texture at $F_g = 1.0$, and is consistent with the pressure gradients in Figure 39.

8.3.2 Vertical Coinjection and Gravity Segregation

Pressure gradients are plotted as a function of gas fraction in **Figure 41**. Coinjections into a vertically positioned fractured network are given in orange and show similar trends compared to the horizontal coinjections represented in blue, and all coinjections peaked at high gas fractional flow. A key difference, however, is an obvious deviation in the magnitude on the recorded pressure during horizontal and vertical coinjection. Foam was visually confirmed near the inlet and outlet ports, but was not observed elsewhere inside the network. Limited foam distribution was likely an effect of gravitational segregation between injected surfactant solution and gas. Mixing occurred near the inlet because the two phases was contacted instantly, but over the system length (31.2 cm), gas gradually settled near the top whereas surfactant solution flowed further down due to density differences between the phases. Foam was generated near the outlet port where narrow fractures opened into the production tubing, most likely by a snap-off mechanism as described by (Gauteplass et al., 2015). Discontinuous foam within the flow paths reduced the flow resistance and the pressure gradients was thus lower for the vertical coinjections compared to the horizontal coinjections.

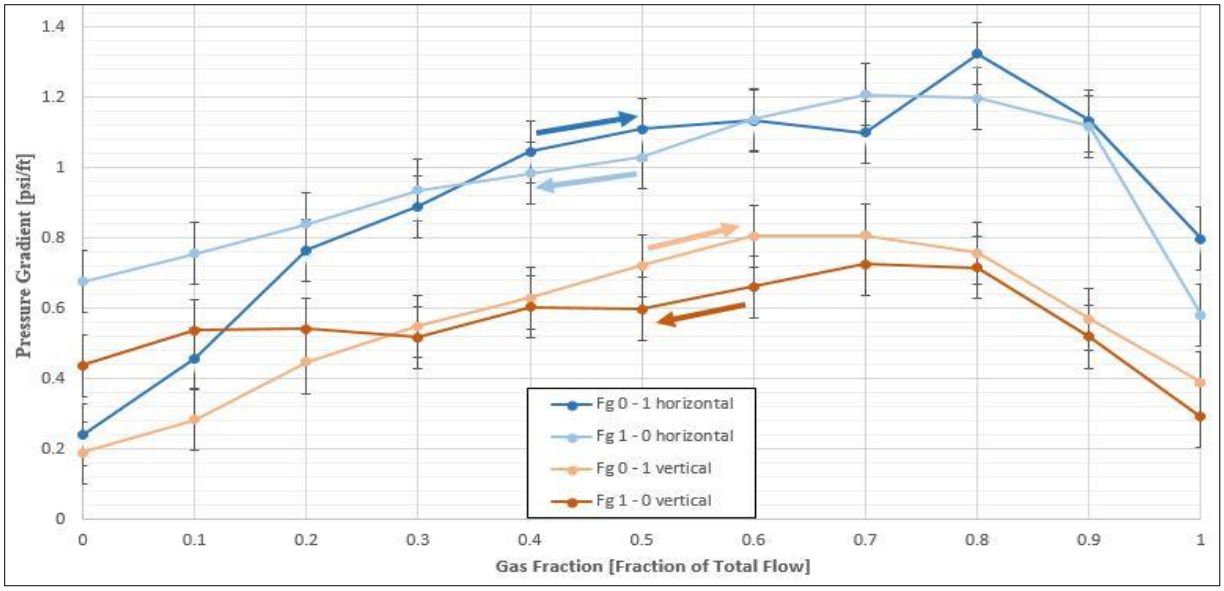

Figure 41: Pressure gradient [psi/ft] as a function of gas fraction during coinjection of surfactant solution and nitrogen gas into a fractured marble network. Blue curves represent experimental data when the system was horizontal and the orange ones represent experiments where the model was mounted in an upright, vertical position. Representative arrows for each experiments are included to indicate the direction of changes in gas fractional flow (i.e. if the experiments were initiated with 100 percent gas and finished with 100 percent surfactant solution or vice versa). The error bars included in each pressure point are calculated from standard deviation in the averaged pressure gradient for a given gas fractional flow.

8.3.3 The Influence of Fracture Geometry and System Design on Foam Distribution

The fractured marble network constitutes a relatively complex flow system of both wide and narrow fractures distributed over an area of 31.2 cm x 31.2 cm. Foam was immediately generated at the inlet port during horizontal coinjection. Use of a ball-peen hammer during the fracturing procedure ensured rough-surfaced fractures similar those found in nature. Flow of surfactant solution and gas through rough fractures with varying aperture resulted in a wide distribution of foam throughout the entire network. This indicate that the rough fractures provide a sufficient amount of snap-off sites. Rough surfaces also increase the drag between the rock surface and flowing bubbles and result in stick and slip movement of bubbles (Buchgraber et al., 2012). Foam generation was particularly apparent near the outlet port and foam was observed to propagate towards the center of the network at high gas fractional flow. This indicates high communication between the fractures.

The size of the system made it possible to thoroughly investigate and observe foam propagation with time. Discontinuous foam distribution during vertical experiments (likely an effect of gravity segregation), address a possible downside with the design. A minor slug of liquid was observed between the Plexiglas and the marble rock when the marble network was mounted in an up-right position. Aluminum rods used to apply force on the Plexiglas and keep the network together was tightened further but with limited success. Additional flow space outside the fractures makes it easier for gas to flow towards the top and increase the risk of gravity segregation. The observed leakage brings uncertainty to whether the reduced pressure gradients measured during vertical coinjection are a result of gravity segregation or an effect gravitational effects on the foam itself.

8.3.4 Up-Scaling from Core to Fractured Marble Network

Foam experiments in System C showed great correspondence between coinjections performed in opposite injection order, both horizontally and vertically. Coinjection of gas with Petrostep-C1 surfactant resulted in generation of fine-textured foam with uniform bubble. The highest pressure increase was found at high gas fractional flow, similar to the pressure gradients observed in both fractured cores. Gas compressibility effects and abrupt changes in foam flow was not visually observed in System C. Pressure data from horizontal coinjection in **Figure A 10** and **Figure A 11** indicates limited scatter in differential during the coinjections, but are based on the assumption of constant atmospheric outlet pressure. Hence, the impact of foam gas compressibility is uncertain in System C and visual observations of lamella only give a qualitative description of foam flow.

Figure 42 compare pressure gradients as a function of gas fractional flow between System A, B, and C. Pressure gradients were lower in System C compared to the core coinjections, and this was attributed to use of a total volumetric rate of 3 ml/min in a fractured system of increased length. **Figure 43** display calculated apparent viscosities for System A, B, and C and implies decreasing gas mobility control by foam at elevated flow rates from shear-thinning of lamella.

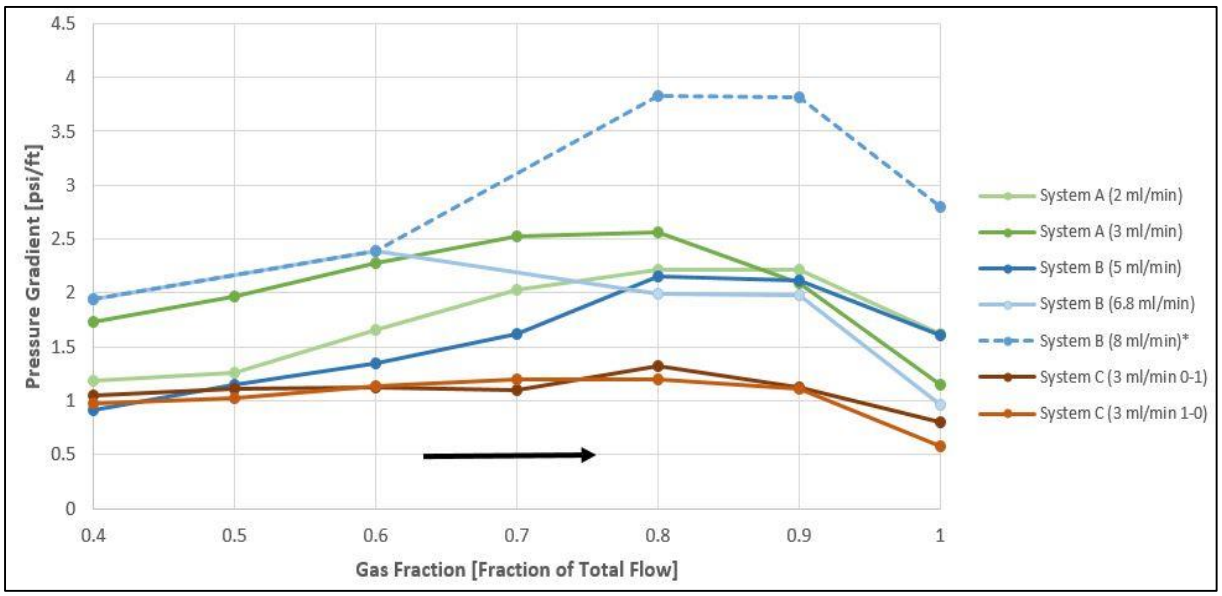

Figure 42: Comparison various F_g 0 − 1 coinjections in System A, B, and C where pressure gradient [psi/ft] is plotted as a function of gas fractional flow. Coinjections from System A, B, and C are represented in green, blue and brown, respectively.

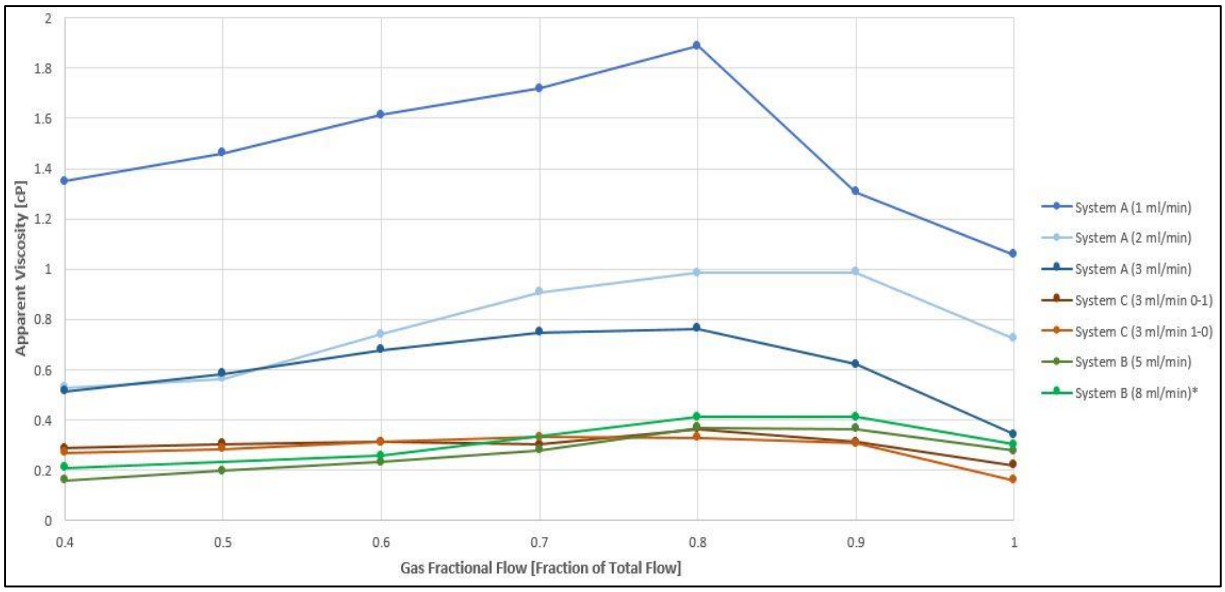

Figure 43: Apparent viscosity as a function of gas fractional flow in System A, B, and C. Decreasing viscosity with increased flow rates indicate shear-thinning of foam in fractured marble systems.

Chapter 4: Conclusions and Future Work

9 Conclusions

Based on coinjections in System A, B, and C, the following conclusions were made.

- Marble cores were successfully drilled, fractured, and reassembled to replicate rough-walled fractures found in reservoirs. Low-permeable marble was used as core material to ensure foam flow primarily in fractures.

- Differential pressure was measured as a function of gas fractional flow to evaluate the relationship between foam quality and flow resistance. Coinjections in all the fractures systems obtained maximum flow resistance at high gas fractional flow ($F_g = 0.7 - 0.9$).

- Change in total volumetric flow rate between the fractured systems made it possible to investigate foam rheology. Apparent viscosity appeared to decrease with in increased flow rates, suggesting shear-thinning of foam within the fractures. Shear-stress at elevated flow rates caused the mobility reduction factor to drop from approximately 100 at 1 ml/min total rate to 10 at 3 ml/min total rate.

- Foam flow did not seem dependent on system size. Pressure gradient curves was highly comparable between System A, B, and C.

- Hysteresis was observed in System A when coinjection order was altered from $F_g = 0 - 1$ to $F_g = 1 - 0$. Hysteresis effects was attributed to presence of trapped gas saturation within the fractured core after coinjection of surfactant solution and gas. By flushing System C with brine from bottom-up with the network oriented in vertical direction, trapped gas was bubbles were observed to be removed. Hence, little hysteresis was apparent during coinjections in System C.

- Positron emission tomography (PET) was successfully used to investigate changes in saturation as a function of gas fractional flow and pressure. PET signals provided access to variation in local surfactant solution concentrations within the fractured network.

- Visual investigation of foam texture during coinjection in System C showed that texture changed from uniform, polyhedral bubbles to coarse, dry bubbles at high gas fractional flow.

10 Future Work

The following work is suggested based on presented results in this thesis.

- Reproduce coinjections presented in this thesis at different flow conditions, e.g. at high pressure and temperature to investigate foam stability at reservoir conditions.

- Routine core analysis should be conducted on System B. Porosity and absolute permeability are essential parameters characterizing reservoir rocks, and absolute permeability needs to be determined to calculate apparent viscosity.

- Baseline studies should be carried out in System A, B, and C. Retention of surfactants was believed to occur in System A, and an effective cleaning procedure should be established to remove remaining surfactant solution between coinjection experiments.

- Acquired PET/CT data can be used in further investigations. Fractures should be characterized in greater detail using obtained CT data. Local variations in detected PET signal may be used to study foam distribution at different gas fractional flows. One possible study would be to link specific trends in pressure to fluids saturations. Reproduction of PET experiments are necessary to draw certain conclusions on the relationship between surfactant distribution and foam flow.

- Coinjections of surfactant solution and gas into oil-saturated, fractured reservoir rocks (e.g. carbonates) should be investigated to evaluate foam application in reservoirs. The fracturing device developed in this thesis may be applied to generate fractured cores with rough fracture surfaces. An interesting study would be to perform baseline studies on oil recovery with pure gas injection, and compare obtained results to oil recovery by coinjecting surfactant solution and gas. Results from these tests could be used to evaluate the ability of foam to reduce viscous fingering and limited sweep efficiency in fractured carbonate reservoirs.

Chapter 5: References and Appendixes

References

AARNES, J. E., KIPPE, V., LIE, K. A. & RUSTAD, A. B. 2007. Modelling of Multiscale Structures in Flow Simulations for Petroleum Reservoirs. *In:* HASLE, G., LIE, K. A. & QUAK, E. (eds.) *Geometric Modelling, Numerical Simulation, and Optimization.* New York: Springer Berlin Heidelberg New York.

AHMED, T. & MEEHAN, N. 2011. *Advanced Reservoir Management and Engineering*, Gulf Professional Publishing, 2011.

AHR, W. M. 2011. *Geology of Carbonate Reservoirs: The identification, Description and Characterization of Hydrocarbon Reservoirs in Carbonate Rocks*, John Wiley & Sons.

AL-ANAZI, B. D. 2007. Enhanced Oil Recovery Techniques and Nitrogen Injection. *Canadian Society of Exploration Geophysics,* 32**,** 28-33.

ALLAN, J. & SUN, S. Q. 2003. Controls on Recovery Factor in Fractured Reservoirs: Lessons from 100 Fractured Fields. *SPE Annual Technical Conference and Exhibition.* Denver, Colorado: Society of Petroleum Engineers.

ALLEN, E. 1995. An Improved Viscosity Equation to Characterize Shear-Thinning Fluids. *SPE International Symposium on Oilfield Chemistry, San Antonio, Texas.* San Antonio, Texas, USA: Society of Petroleum Engineers.

ANDERSON, W. 1986. Wettability Literature Survey- Part 1: Rock/Oil/Brine Interactions and the Effects of Core Handling on Wettability. *Journal of Petroleum Technology,* 38**,** 1246-1262.

ATTANASIO, D., BRILLI, M. & OGLE, N. 2006. *Studia Archaeologica*, L'ERMA di BRETSCHNEIDER.

BAILEY, D. L., TOWNSEND, D. W., VALK, P. E. & MAISEY, M. N. 2004. *Positron Emission Tomography: Basic Science*, Springer Science & Business Media.

BROWN, H. W. 1951. Capillary Pressure Investigations. *Journal of Petroleum Technology,* 3**,** 67-74.

BUCHGRABER, M., CASTANIER, L. M. & KOVSCEK, A. R. 2012. Microvisual Investigation of Foam Flow in Ideal Fractures: Role of Fracture Aperture and Surface Roughness. *SPE Annual Technical Conference and Exhibition.* San Antonio, Texas: Society of Petroleum Engineers.

BUST, V. K., OLETU, J. U. & WORTHINGTON, P. F. 2011. The Challanges for Carbonate Petrophysics in Petroleum Resource Estimation. *SPE Reservoir Evaluation & Engineering,* 14**,** 25-34.

CHEN, M., YORTSOS, Y. C. & ROSSEN, W. R. 2004. A Pore-Network Study of the Mechanisms of Foam Generation. *SPE Annual Technical Conference and Exhibition.* Houston, Texas: Society of Petroleum Engineers.

CORAPCIOGLU, M. Y. 1996. *Advances In Porous Media, Volume 3*, Elsevier, 1996.

COTE, H. & THIMUS, J. F. 1999. Ultrasonic Velocity And Attenuation During Brazilian Test. *9th ISRM Congress.* Paris, France: International Society for Rock Mechanics.

DENNEY, D. 2003. Fractured-Reservoir Recovery Factors: Lessons From 100 Fields. *Journal of Petroleum Technology,* 55**,** 51-52.

DONALDSON, E. C., CHILINGARIAN, G. V. & YEN, T. F. 1989. *Enhanced Oil Recovery, II - Processes and Operations,* New York, USA, Elsevier Science Publishers Company Inc.

EIDE, Ø. 2011. *Integrated EOR and Waterflood Stability Criteria in Carbonate Rock.* Masters Degree, University of Bergen.

ENICK, E. M. & OLSEN, D. K. 2012. Mobility and Conformance Control for Carbon Dioxide Enhanced Oil Recovery (CO2-EOR) via Thickeners, Foams and Gels - A Detailed Literature Review of 40 Years of Research. National Energy Technology Laboratory.

ERDAL, A. 2011. *Elementær innføring i sannsynlighetsregning og problemløsning ved analyse av måleresultater,* Department of Physics and Technology, University of Bergen.

EXEROWA, D. & KRUGLYAKOV, P. M. 1998. *Foam and foam films : theory, experiment, application,* New York, Elsevier.

FARAJZADEH, R., LOTFOLLAHI, M., EFTEKHARI, A. A., ROSSEN, W. R. & HIRASAKI, G. J. H. 2015. Effect of Permeability on Implicit-Texture Foam Model Parameters and the Limiting Capillary Pressure. *Energy & Fuels,* 29**,** 3011-3018.

FERNØ, M. A. 2012. Enhanced Oil Recovery in Fractured Reservoirs. *In:* ROMERO-ZERÒN, L. (ed.) *Introduction to Enhanced Oil Recovery (EOR) Processes and Bioremediation of Oil-Contaminated Sites.* Intech.

FERNØ, M. A. 2015. Laboratory Evaluation of CO2 Flow and EOR - Insight Through Visualization. *NorTex Petroleum Cluster Collaborative Symposium on CO2 for EOR as CCUS.* Rice University, Houston, Texas, Oct. 4-6, 2015: NorTex Petroleum Cluster.

FERNØ, M. A., GAUTEPLASS, J., PANCHAROEN, M., HAUGEN, Å., GRAUE, A., KOVSCEK, A. R. & HIRASAKI, G. 2016. Experimental Study of Foam Generation, Sweep Efficiency, and Flow in a Fracture Network. *SPE Journal,* Preprint.

FIROOZABADI, A. 2000. Recovery Mechanisms in Fractured Reservoirs and Field Performance *Journal of Canadian Petroleum Technology,* 39.

FRIEDMANN, F. & JENSEN, J. A. 1986. Some Parameters Influencing the Formation and Propagation of Foams in Porous Media. *SPE California Regional Meeting.* Oakland, California: Society of Petroleum Engineers.

GAUTEPLASS, J., CHAUDARY, K., KOVSCEK, A. R. & FERNØ, M. A. 2015. Pore-level foam generation and flow for mobility control in fractured systems. *Colloids and Surfaces A: Physicochemical and Engineering Aspects,* 486**,** 184-192.

GRUNDMANN, S. R. & LORD, D. L. 1983. Foam Stimulation. *Journal of Petroleum Technology,* 35**,** 597-602.

GUO, H., FABER, M. J., BUIJSE, M. A. & ZITHA, P. L. J. 2011. A Novel Alkaline-Surfactant-Foam EOR Process. *SPE Enhanced Oil Recovery Conference* Kuala Lumpur, Malaysia: Society of Petroleum Engineers.

HICKS, P. J., JR. 1996. X-Ray Computer-Assisted Tomography for Laboratory Core Studies. *Journal of Petroleum Technology,* 48**,** 1120-1122.

HIRASAKI, G., MILLER, C. A. & PUERTO, M. 2011. Recent Advances in Surfactant EOR. *SPE Journal,* 16**,** 889 - 907.

HIRASAKI, G. J. & LAWSON, J. B. 1985. Mechanisms of Foam Flow in Porous Media: Apparent Viscosity in Smooth Capillaries. *Society of Petroleum Engineers Journal,* 25**,** 176-190.

HOLM, L. W. 1968. The Mechanism of Gas and Liquid Flow Through Porous Media in the Presence of Foam. *Society of Petroleum Engineers Journal,* 8**,** 359-369.

JANSSEN, J., MANCA, O. & MANCA, R. 2013. *Applied Diffusion Processes from Engineering to Finance,* Hoboken, Wiley.

KAM, S. I. 2007. Improved Mechanistic Foam Simulation with Foam Catastrophe Theory. *Colloids and Surfaces A: Physicochemical and Engineering Aspects,* 318**,** 62-77.

KHATIB, Z. I., HIRASAKI, G. J. & FALLS, A. H. 1988. Effects of Capillary Pressure on Coalescence and Phase Mobilities in Foams Flowing Through Porous Media. *SPE Reservoir Engineering,* 3 919-926.

KOVSCEK, A. R., CHEN, Q. & GERRITSEN, M. 2010. Modeling Foam Displacement With the Local-Equilibrium Approximation: Theory and Experimental Verification. *SPE Journal,* 15**,** 171-183.

KOVSCEK, A. R. & RADKE, C. J. 1993. Fundamentals of Foam Transport in Porous Media. U.S. Department of Energy.

KOVSCEK, A. R., TRETHEWAY, D. C., PERSOFF, P. & RADKE, C. J. 1995. Foam flow through a transparent rough-walled rock fracture. *Journal of Petroleum Science and Engineering,* 13**,** 75-86.

LAWSON, J. & REISBERG, J. 1980. Alternate Slugs of Gas and Dilute Surfactant for Mobility Control During Chemical Flooding. *SPE/DOE Enhanced Oil Recovery Symposium.* Tulsa, Oklahoma: Society of Petroleum Engineers.

LEE, S. T. & RAMESH, N. S. 2004. *Polymeric Foams: Mechanisms and Materials*, CRC Press, 2004.

LI, R. F., HIRASAKI, G. J., MILLER, C. A. & MASALMEH, S. K. 2011. Wettability Alteration and Foam Mobility Control in a Layered 2-D Heterogeneous System. Society of Petroleum Engineers.

LIEN, J. R., JAKOBSEN, M. & SKAUGE, A. 2011. *Introduksjon til petroleums- og prosessteknologi,* Universitetet i Bergen.

LYONS, W. C. & PLISGA, G. S. 2005. *Standard Handbook of Petroleum & Natural Gas Engineering,* Burlington, MA, USA. , Elsevier/Gulf Professional Pub.

MARSHAK, S. 2011. *Eart: Portrait of a Planet,* Canada, W. W. Norton & Company, Inc. .

MARTINS, A. L., LOURENCO, A. M. F., SA, C. H. M. & JR., V. S. 2001. Foam Rheology Characterization as a Tool for Predicting Pressure While Drilling Offshore Wells in UBD Conditions. *SPE/IADC Drilling Conference.* Amsterdam, Netherlands: Society of Petroleum Engineers.

MAUCEC, M., DUSTERHOFT, R., RICKMAN, R., GIBSON, R., BUFFLER, A., STANKIEWICZ, M. & HEERDEN, M. V. 2013. Dynamic Imaging of Fluid Mobility in Low-Permeability Matrices Using Positron Emission Tomography. *Unconventional Resources Technology Conference.* Denver, Colorado, USA: Society of Petroleum Engineers.

MUGGERIDGE, A., COCKIN, A., WEBB, K., FRAMPTON, H., COLLINS, I., MOULDS, T. & SALINO, P. 2013. Recovery rates, enhanced oil recovery and technological limits. *Philosophical Transactions of The Royal Society,* 372.

MUKERJEE, P. & MYSELS, K. J. 1971. Critical Micelle Concentrations of Aqueous Surfactant Systems. *Journal of Pharmaceutical Sciences,* 61.

NELSON, R. 2001. *Geologic Analysis of Naturally Fractured Reservoirs*, Gulf Professional Publishing.

NGUYEN, Q. P., CURRIE, P. K. & ZITHA, P. L. J. 2005. Effects of Crossflow on Foam-Induced Diversion in Layered Formations. *SPE Journal,* 10**,** 54-65.

OKON, A. N. & UDOH, F. D. 2013. Gas-oil gravity drainage in fractured porous media. *Indian Journal of Engineering,* 3**,** 70-75.

PANCHAROEN, M., FERNØ, M. & KOVSCEK, A. R. 2012. Modeling foam displacement in fractures. *Journal of Petroleum Science and Engineering,* 100**,** 50-58.

PATTON, J. T., HOLBROOK, S. T. & HSU, W. 1983. Rheology of Mobility-Control Foams. *Society of Petroleum Engineers Journal,* 23**,** 456-460.

RANSOHOFF, T. C. & RADKE, C. J. 1988. Mechanisms of Foam Generation in Glass-Bead Packs. *SPE Reservoir Engineering,* 3**,** 573-585.

ROSSEN, W. R. 1988. Theory of mobilization pressure gradient of flowing foams in porous media: I . Incompressible foam. *Journal of Colloid and Interface Science,* 136**,** 1-16.

SCHRAMM, L. L. 1994. *Foams : fundamentals and applications in the petroleum industry,* Washington, DC, American Chemical Society.

SHENG, J. 2013. *Enhanced Oil Recovery Field Case Studies*, Gulf Professional Publishing.

SKARESTAD, M. & SKAUGE, A. 2012. *Reservoarteknikk II, PTEK213,* University of Bergen.

SKAUGE, A., AARRA, M. G., SURGUCHEV, L., MARTINSEN, H. A. & RASMUSSEN, L. 2002. Foam-Assisted WAG: Experience from the Snorre Field. *SPE/DOE Improved Oil Recovery Symposium.* Tulsa, Oklahoma: Society of Petroleum Engineers.

SKJÆVELAND, S. M. & KLEPPE, J. 1992. *SPOR - Recent Advances in Improved Oil Recovery Methods for North Sea Sandstone Reservoirs,* Stavanger, Norway, Norwegian Petroleum Directorate.

SPEIGHT, J. G. 2013. *Enhanced Recovery Methods for Heavy Oil and Tar Sands*, Elsevier.

STEVENSON, P. 2011. *Foam Engineering: Fundamentals and Applications,* Hoboken, Wiley.

SUZUKI, F. 1990. X-Ray Computed Tomography For Carbonate Acidizing Studies. *Annual Technical Meeting.* Calgery, Alberta: Petroleum Society of Canada.

UREN, L. C. 1939. *Petroleum Production Engineering,* New York, USA, McGraw Hill.

VAN GOLF-RACHT, T. D. 1982. *Fundamentals of Fractured Reservoir Engineering*, Elsevier.

VRIJ, A. & OVERBEEK, J. T. G. 1968. Rupture of Thin Liquid Films Due to Spontaneous Fluctuations in Thickness. *J. Am. Chem. Soc.,* 90**,** 3074-3078.

WANG, L. & MOHANTY, K. 2014. Enhanced Oil Recovery in Gasflooded Carbonate Reservoirs by Wettability-Altering Surfactants. *SPE Journal,* 20**,** 60-69.

YAN, W., MILLER, C. A. & HIRASAKI, G. J. 2006. Foam sweep in fractures for enhanced oil recovery. *Colloids and Surfaces A: Physicochemical and Engineering Aspects,* 282**,** 348-359.

YUDOVICH, A., CHIN, L. Y. & MORGAN, D. R. 1989. Casing Deformation in Ekofisk. *Journal of Petroleum Technology,* 41**,** 729-734.

ZOLOTUKHIN, A. B. & URSIN, J. R. 2000. *Introduction to Petroleum Reservoir Engineering*.

Appendix A – Uncertainties and Calculations

Calculated uncertainties in this thesis are based on the following equations from Erdal (2011):

The uncertainty of an experimental value R involving several variables $x, y, z, \dots, i$, with individual uncertainties $\Delta x, \Delta y, \Delta z, \dots, \Delta i$ may be calculated as:

$$\Delta R = R\sqrt{\left(\frac{\Delta x}{x}\right)^2 + \left(\frac{\Delta y}{y}\right)^2 + \left(\frac{\Delta z}{z}\right)^2 + \cdots + \left(\frac{\Delta i}{i}\right)^2} \tag{A1}$$

Equation (A1) was used to calculate the uncertainty of bulk volume V_b, pore volume V_p and porosity φ during routine core analysis of System A. As discussed in **Section 7.1**, these parameters are based on length (caliper) and mass (weight). Uncertainty in absolute permeability (i.e. Darcy's law) was also calculated with equation (A1) and included uncertainties in measured pressure (ESI transducers) and core length/surface area (caliper). Instrumental uncertainties are listed in **Table 6**.

The mean value $\bar{x}$ of a series of data points $x_1, x_2, x_3, \dots, x_N$ may be calculated as:

$$\bar{x} = \frac{1}{N}\sum_{i=1}^{N} x_i = \frac{x_1 + x_2 + x_3 + \cdots + x_N}{N} \tag{A2}$$

Equation (A2) were used to calculate an averaged pressure gradient for each gas fractional flow. Pressure data included in Appendix C indicate significant variations in pressure between different gas fractional flows. Thus, the uncertainty in pressure varies with gas fraction. The uncertainty in each averaged pressure gradient was therefore determined using standard deviation, σ, given in equation (A3). The uncertainty of a mean value $\bar{x}$ may be calculated from standard deviation, σ, quantifying the amount of variation between individual variables of a data set. Considering an a random variable A in a data set, the standard deviation σ is given as:

$$\sigma = \sqrt{(A - \bar{x})^2} \tag{A3}$$

Table 6: Instrumental uncertainties provided by the manufacture of the instruments.

Instrument	Parameter	Uncertainty	Unit
Caliper	Length	$\pm$0.02	mm
Pressure transducers	Pressure	$\pm$0.09	psi
Weight	Mass	$\pm$0.01	gram
Mass flow controller	Volume	$\pm$0.02	ml/min

Although uncertainties related to instruments are an important factor influencing the validity of experimental data, the primary source of error is attributed to the procedure. Incidents with leakage of fluids and changed flow conditions between coinjections (e.g. different constant backpressure) are examples of errors that likely affected the comparability between experiments in this thesis. However, the statistic validity of experimental work increase with number of experiments, and findings from this thesis will hopefully contribute to improved understanding of foam behavior in fractured systems.

Appendix B – Fundamentals

The following section includes fundamental parameters relevant for foam and petroleum recovery in general.

Interfacial Tension

Interfacial tension σ (IFT) presents itself as a membrane-like equilibrium surface separating two immiscible fluids. Strong intermolecular cohesion and little molecular exchange at the interface reduces the contact area between the phases, and the magnitude of the resulting interfacial tension equals the energy required to keep the two phases apart in a pressure equilibrium state (Zolotukhin and Ursin, 2000). Depending on the relative magnitude of the intra- and interfluid cohesive forces, this energy gives insight to how different fluids interact:

- $\sigma > 0$: Molecules of each fluid are strongly attracted to molecules of their own kind, making the fluids immiscible.
- $\sigma \approx 0$: Molecules are equally attracted to its own and the other kind. Slow bilateral diffusion will lead to full mixing eventually.
- $\sigma < 0$: Molecules of one fluid are more attracted to the molecules of the other kind. This leads to dissolution, a chemical reaction forming a new fluid.

Capillary Pressure

The effects of capillary pressures, P_c, in petroleum reservoirs are of huge importance. Along with gravity, P_c controls the distribution of fluid saturation within the reservoir as well as the relative freedom of movement for the fluids, making it a key parameter in production processes (Brown, 1951). The pressure associated with interfacial tension is known as the capillary pressure P_c. Based on two fluids ability to spread on a solid's surface in the presence of one another (wettability), capillary pressure is given as the pressure difference between the non-wetting fluid and the wetting fluid. Based on two fluids ability to spread on a solid's surface in the presence of one another (wettability), capillary pressure is defined as the pressure difference between a non-wetting and wetting fluid (e.g. gas and surfactant solution). In a capillary tube shown in **Figure A 1**, P_c could also be written according to the Young-Laplace equation.

$$P_c = P_{nw} - P_w = \frac{2\sigma cos\theta}{r} \tag{A4}$$

where p_{nw} and p_w is the pressure in the non-wetting and the wetting phase, θ is the wetting angle and r is the radius capillary tube.

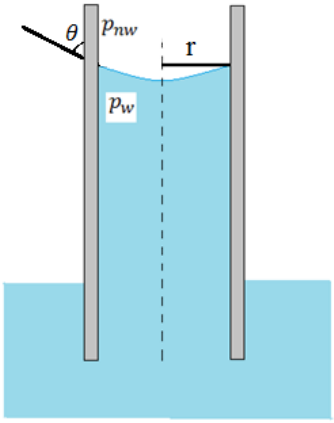

Figure A 1: Illustration of capillary pressure in a capillary tube filled with water. Due to the water-wet nature of the tube itself, water rises in the tube to a certain height where the weight of the liquid column equals the vertical component of the interfacial tension. The curved meniscus observed at the top is convex towards the wetting fluid. Redrawn from (Lien et al., 2011).

Surfactants

A surfactant molecule, or monomer, is often represented as a tadpole consisting of a nonpolar (lypophile) tail and a polar (hydrophile) head. The most energetically favorable orientation for these molecules is at interfaces between two fluids (e.g. water/gas), where each part of the molecule can reside in the fluid where it has the greatest affinity. Surfactant adsorption along an interface provides an expanding force causing a drastic reduction in the normal IFT (Schramm, 1994). When surfactants is dissolved in a solution, a critical micelle concentration (CMC) is reached when monomers aggregate into micelles where the hydrophile end is oriented outward and the lypophile inward (Skarestad and Skauge, 2012). The mentioned phenomena are illustrated in **Figure A 2**.

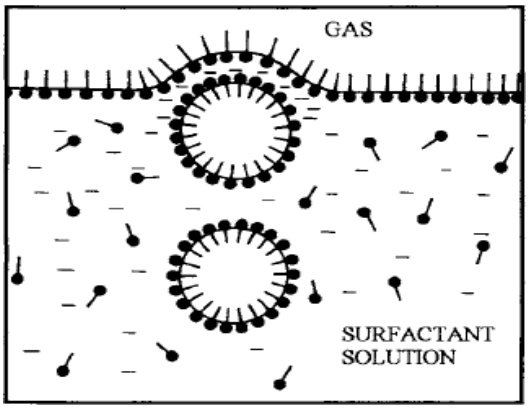

Figure A 2: Illustration of surfactant adsorption along an interface between gas and a surfactant solution. The lypophile tail of the monomer faces the gas while the hydrophile head faces the water. Micelles within the surfactant solution is also shown (Exerowa and Kruglyakov, 1998).

The aim of adding surfactants to the injected water is to recover the capillary trapped residual oil after water flooding. The residual oil saturation correlates well with the dimensionless capillary number N_c defined by (Skarestad and Skauge, 2012):

$$N_c = \frac{u_w \cdot \mu_w}{\sigma_{ow}} \tag{A5}$$

where u_w is the Darcy velocity, μ_w is the viscosity of the injected water and σ_{ow} is the interfacial tension between oil and the surfactant solution. Hirasaki et al. (2011) found that IFT has to be reduced from crude-oil/brine values of 20 to 30 mN/m to the range of 0,001 to 0,01 mN/m to get values of residual-oil saturation lower than 0,05 in a reservoir. Introduction of a surfactant into a liquid also changes the properties of gas dispersions (gas present in a continuous phase of a different fluid) and liquid films by acting as a stabilizer (Exerowa and Kruglyakov, 1998). Surfactant accumulation at a gas/surfactant-solution interface prevents immediate rupture of the liquid film and thus aids as a foaming agent.

Appendix C – Experimental Data

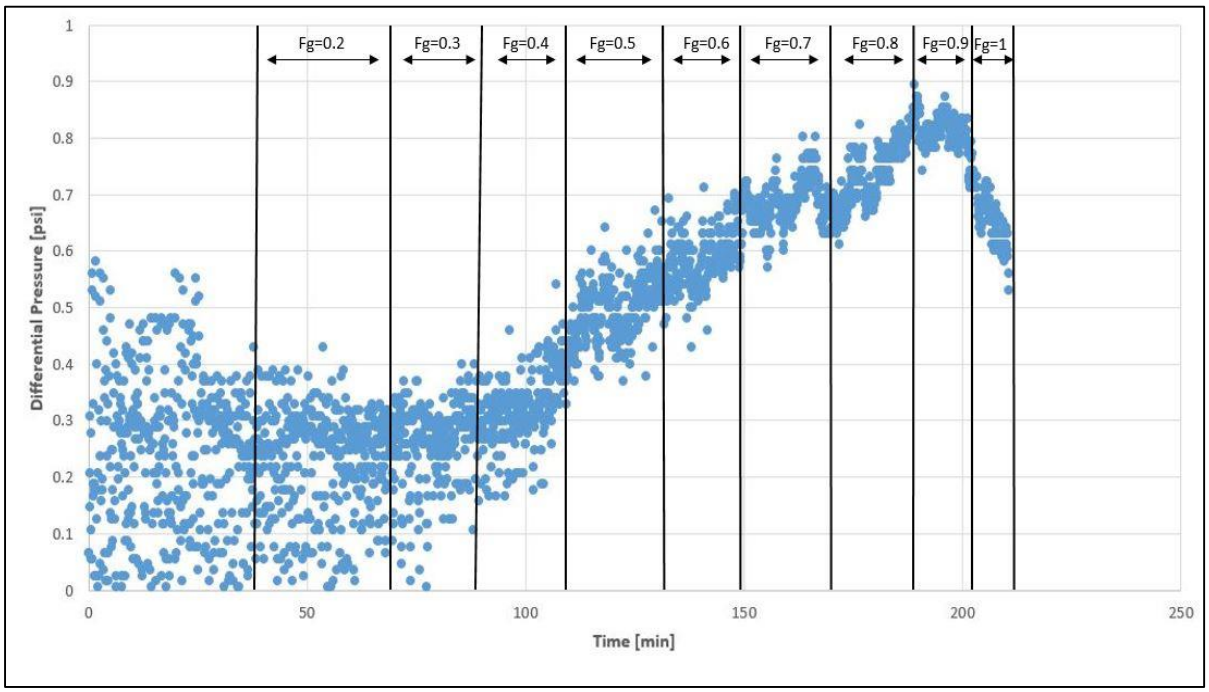

Figure A 3: Differential pressure [psi] as a function of time [min] during 1 ml/min coinjection of brine and air in System A.

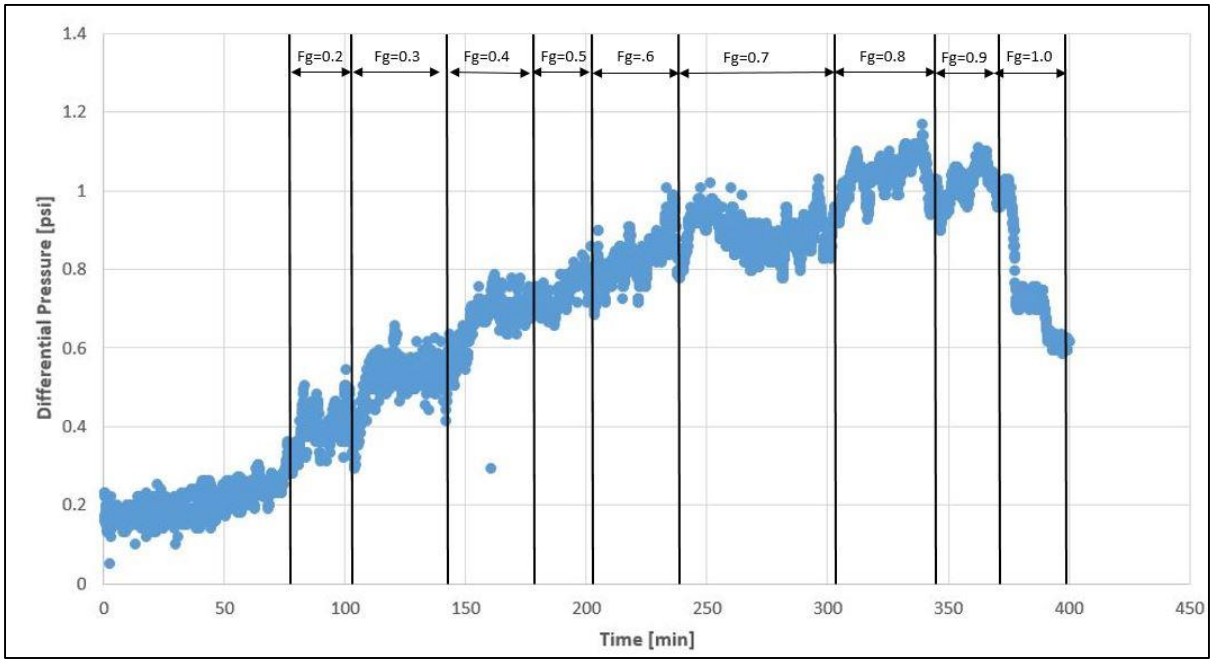

Figure A 4: Differential pressure [psi] as a function of time [min] during 1 ml/min coinjection of Huntsman surfactant solution and air in System A.

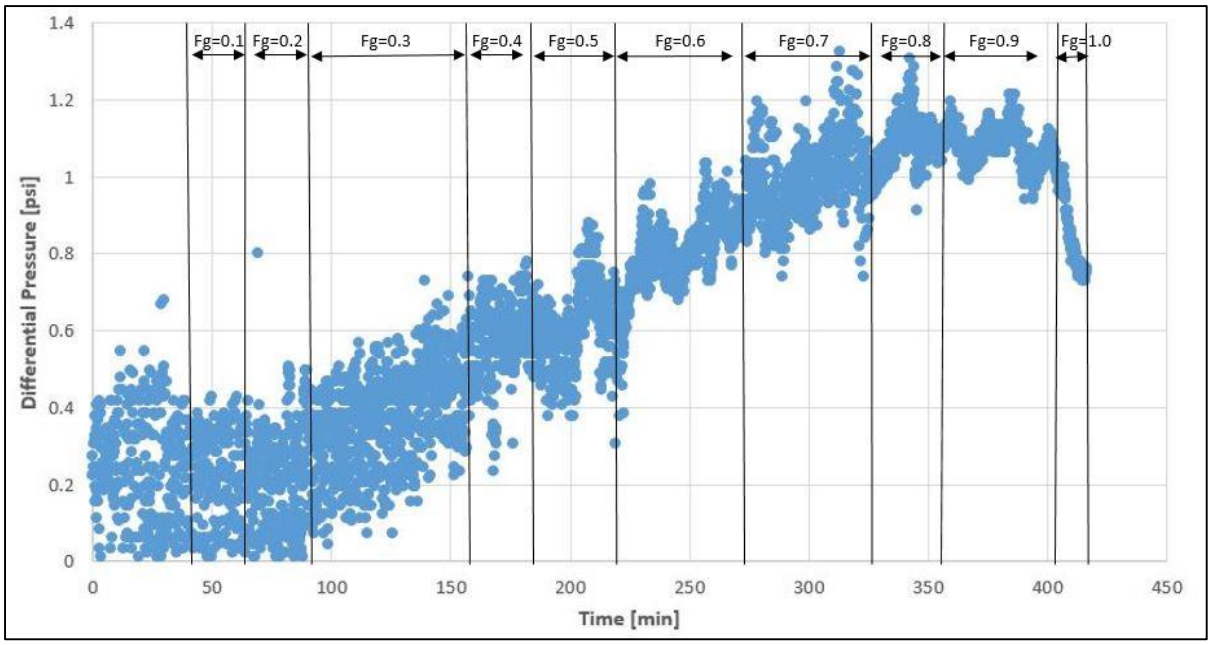

Figure A 5: Differential pressure [psi] as a function of time [min] during 2 ml/min coinjection of Huntsman surfactant solution and air in System A.

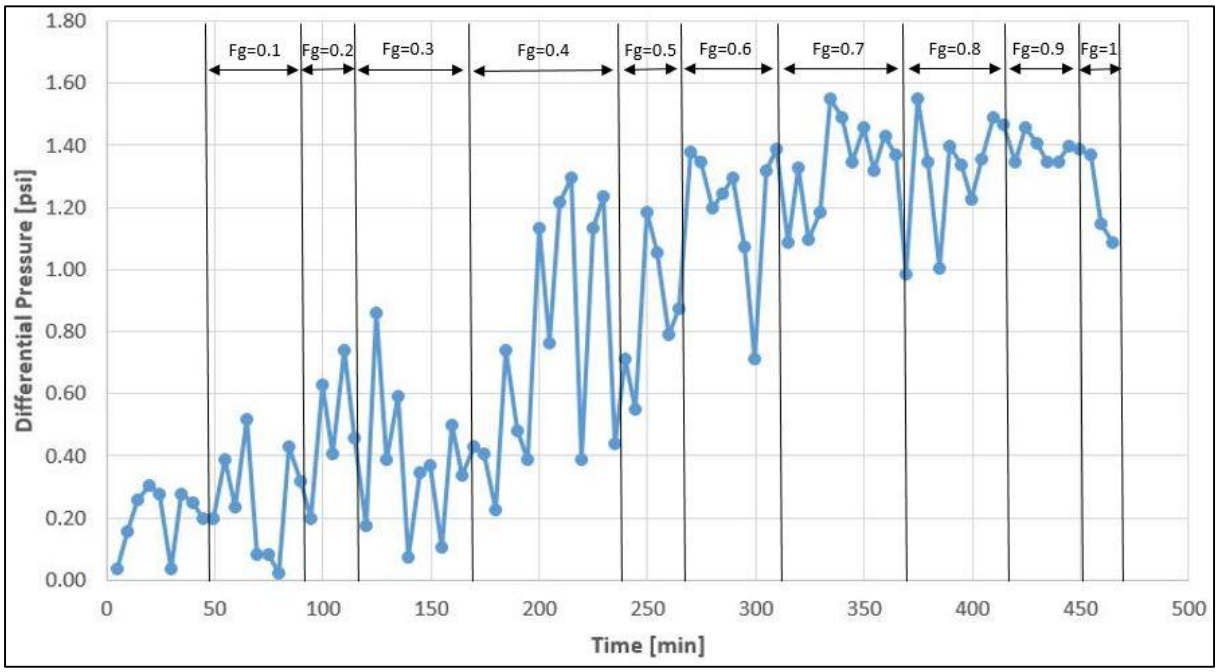

Figure A 6: Differential pressure [psi] as a function of time [min] during 3 ml/min coinjection of Huntsman surfactant solution and air in System A. Data presented here has been processed in an a data reduction Excel sheet to a clarify pressure trends.

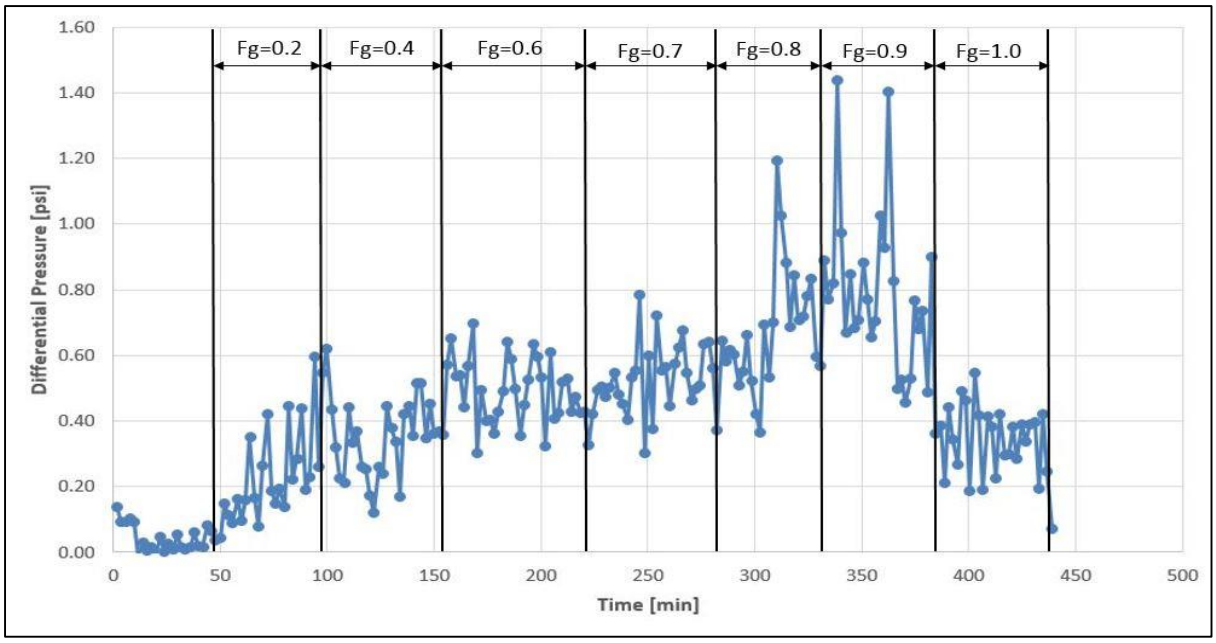

Figure A 7: Differential pressure [psi] as a function of time [min] during 2.5 ml/min coinjection of Huntsman surfactant solution and air in System A. Data presented here has been processed in an a data reduction Excel sheet to a clarify pressure trends.

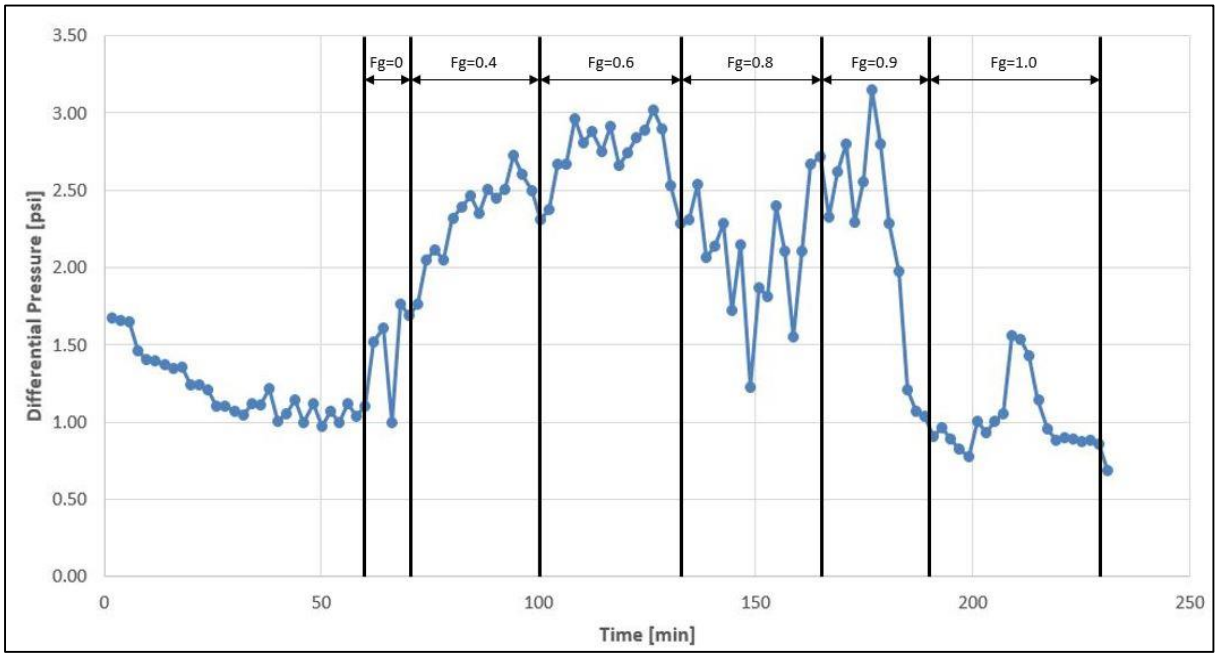

Figure A 8: Differential pressure [psi] as a function of time [min] during 8 ml/min coinjection of Huntsman surfactant solution and nitrogen in System B. Data presented here has been processed in an a data reduction Excel sheet to a clarify pressure trends.

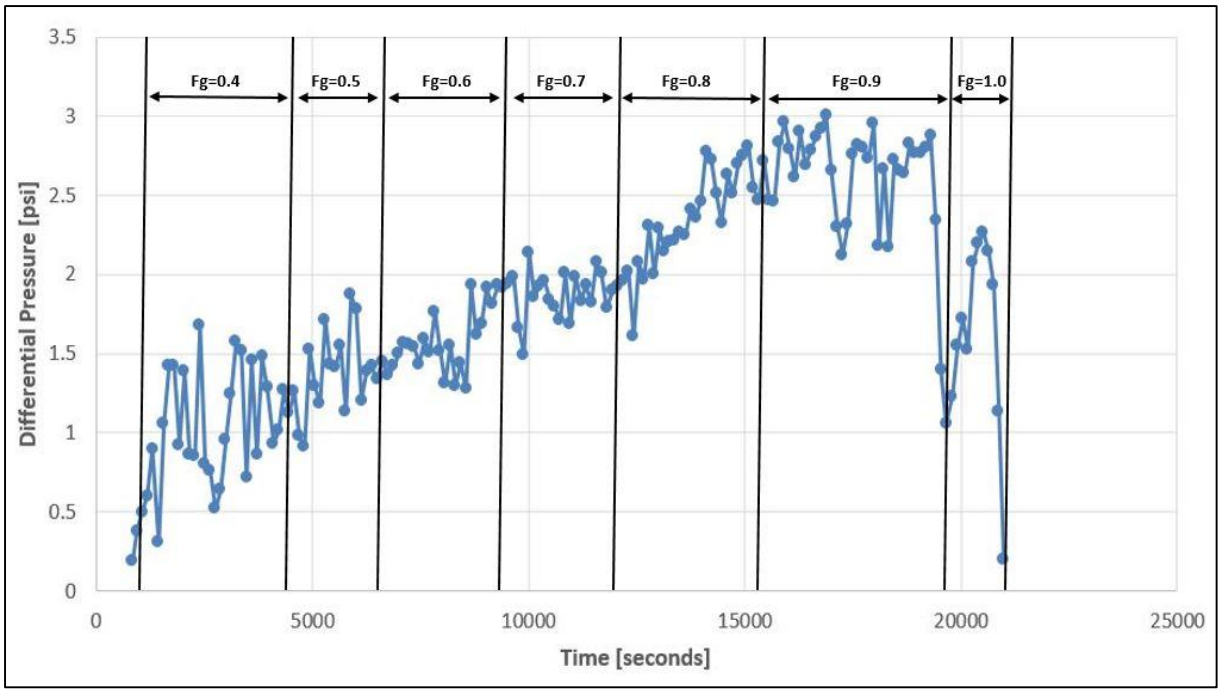

Figure A 9: Differential pressure [psi] as a function of time [min] during 3 ml/min coinjection of Huntsman surfactant solution and nitrogen in System B. Data presented here has been processed in an a data reduction Excel sheet to a clarify pressure trends.

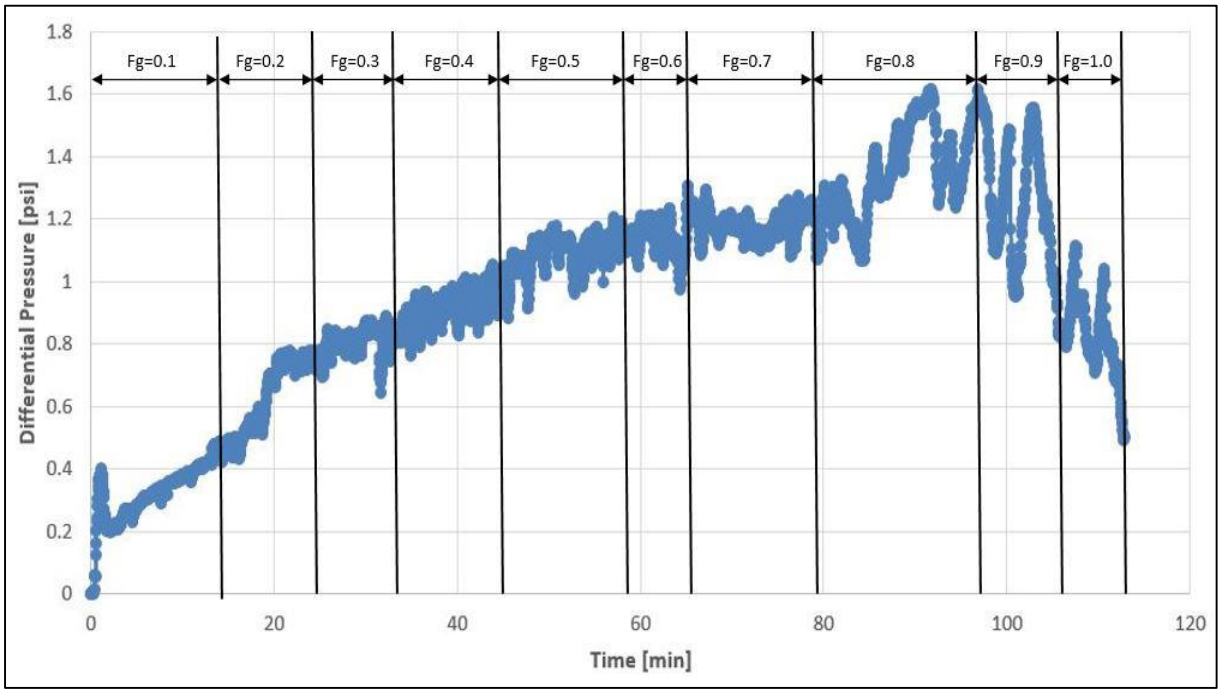

Figure A 10: Differential pressure [psi] as a function of time [min] during 3 ml/min coinjection of Petrostep surfactant solution and nitrogen in System C.

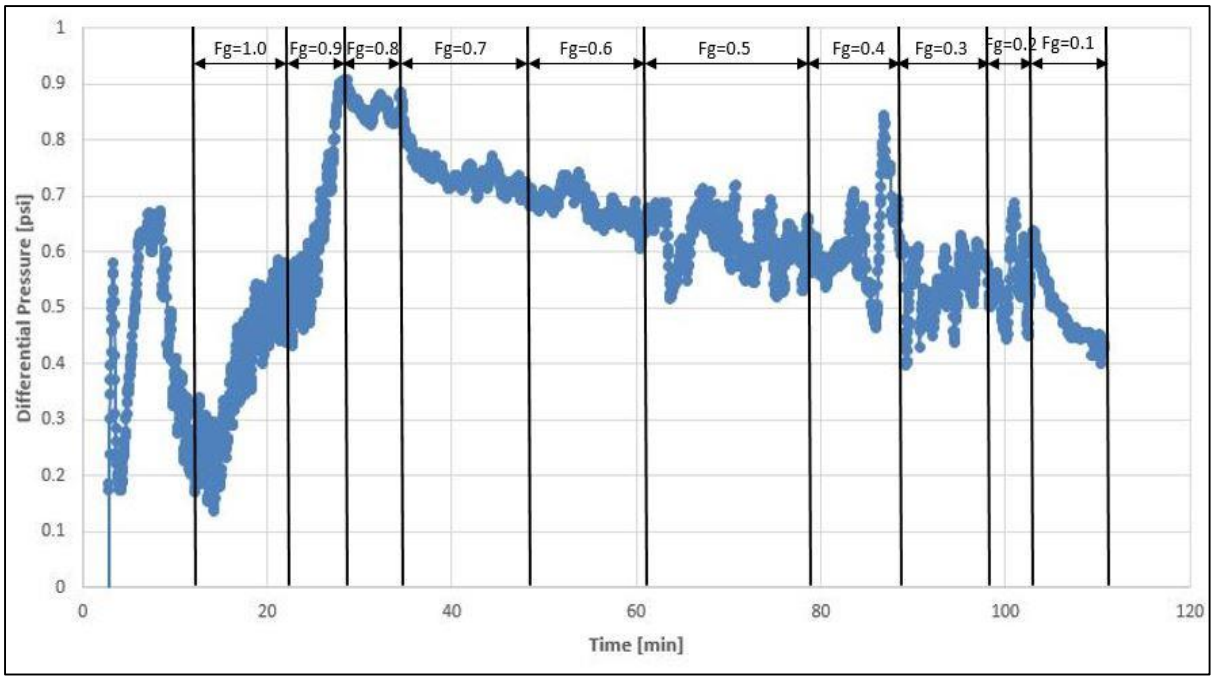

Figure A 11: Differential pressure [psi] as a function of time during 3 ml/min ($F_g = 1 - 0$) coinjection of Petrostep surfactant solution and nitrogen in System C.